

UC Berkeley

UC Berkeley Electronic Theses and Dissertations

Title

Emergent Ferroic Order at Oxide Heterointerfaces

Permalink

<https://escholarship.org/uc/item/1cj1x1q0>

Author

Lupi Sosa, Eduardo Andres

Publication Date

2021

Peer reviewed|Thesis/dissertation

Emergent Ferroic Order at Oxide Heterointerfaces

by

Eduardo Andres Lupi Sosa

A dissertation submitted in partial satisfaction of the

requirements for the degree of

Doctor of Philosophy

in

Engineering- Materials Science and Engineering

in the

Graduate Division

of the

University of California, Berkeley

Committee in charge:

Professor Lane W. Martin, Chair

Professor Ramamoorthy Ramesh

Professor Jeffrey Neaton

Spring 2021

Emergent Ferroic Order at Oxide Heterointerfaces

Copyright 2021

by

Eduardo Andres Lupi Sosa

Abstract

Emergent Ferroic Order at Oxide Heterointerfaces

By

Eduardo Andres Lupi Sosa

Doctor of Philosophy in Materials Science and Engineering

University of California, Berkeley

Professor Lane W. Martin, Chair

This work focuses on complex-oxide superlattices as a pathway to numerous forms of emergent phenomena due to strong interfacial interactions present in unit-cell precise structures. Superlattices based on ferroelectric and dielectric materials can elicit new forms of ferroelectricity, exotic dipolar textures, and distinctive domain structures. Here, I place two different ferroelectric phases in the $\text{PbZr}_{1-x}\text{Ti}_x\text{O}_3$ system and use superlattice design as a proxy for local composition – asking what happens when the overall chemistry is that of the morphotropic phase boundary, but the individual layers are far away from that boundary? The intimate interfacing of these dissimilar materials results in a unique combination of effects: simultaneous large polarization magnitude and large permittivity. The material effectively acts like a combination of the robust parent ferroelectrics and an interfacial region that akin to the phase-boundary. Next, I analyze relaxor-like behavior, which is typically associated with chemical inhomogeneity and complexity in solid solutions, in atomically precise $(\text{BaTiO}_3)_m/(\text{SrTiO}_3)_n$ symmetric superlattices. Dielectric studies reveal frequency dispersion of dielectric response which increases in magnitude as the periodicity decreases. Techniques such as Vogel-Fulcher analysis and bond valence molecular dynamics simulations reveal that relaxor-like behavior in short-period superlattices arises from temperature-driven size variations of antipolar stripe domains in contrast to the more thermally stable dipolar configurations in long-period superlattices. Moreover, the size and shape of antipolar domains are tuned by superlattice periodicity following Kittel's Law thus providing an artificial route to relaxor-like behavior which may expand the ability to control desired properties in these complex systems. Ultimately, I show that unit-cell-precise deposition provides a pathway to design novel heterostructures and thus access interfacial-driven phenomena, posing the question: can control at a single unit-cell be achieved with designer chemical ordering and structure? Such questions will motivate the community's further pursuit of these matters. The current work paves the way for future research in the realization of novel approaches to ferroelectricity stemming from interfacial interactions, which will continue to be more relevant as devices get smaller.

To my family for their complete and unwavering support

Acknowledgments

First, I would like to thank Professor Lane Martin for the incredibly consistent mentorship and support through my doctoral studies. Lane is a true academic, always acting with an extremely high standard in both technical and ethical aspects of the craft.

Prof. Ramamoorthy Ramesh also provided a well-rounded shape to my graduate studies, asking the big picture questions at the precise moment, which was every moment along the way.

I would also like to acknowledge the tremendous support from the Martin and Ramesh groups, whose force amassed that of an army that supported me as I progressed through the ranks during my doctoral studies. Within these groups, Ran Gao was the primary mentor who showed me the ropes with his expertise. Throughout the years, I built long-term and scientifically engaging interactions with so many postdoctoral mentors including Dr. Derek Meyers, Dr. Zuhuang Chen, Dr. Anirban Ghosh, Dr. Lei Zhang, Dr. David Pesquera, Dr. Arnoud Everhardt, Dr. Yen-Lin Huang, and Dr. Sujit Das.

Throughout my doctoral studies, I had the pleasure of working closely with a wealth of peers, acting as a mentee, and mentor, and every shade between. I appreciate all of my interactions with Dr. Ruijuan Xu, Dr. Shishir Pandya, Dr. Sahar Saremi, Jieun Kim, Arvind Dasgupta, Abel Fernandez, Megha Acharya, Yizhe Jiang, Zishen Tian, Anton Zahradnik, David Garcia, Margaret McCarter, Xiaoxi Huang, Eric Parsonnet, and Dr. Shang-Lin Hsu.

I would also like to thank Dr. Gabriel Velarde for the incredible support and bond built through long hours in the laboratory. Serving as each other's first sounding board was an incredibly fruitful relationship as peers throughout the entire doctoral program.

My collaborators Dr. Robert Wexler and Prof. Andrew Rappe were fantastic during the last year. Their close-knit collaboration led to incredibly insightful and scientifically appealing discussion.

I would like to thank my dissertation committee members, Prof. Ramamoorthy Ramesh and Prof. Jeffrey Neaton, and Prof. Lane Martin for their guidance through my qualifying exam that gave me the direction to hone my efforts on making meaningful and effective progress in my research.

This work has been supported, in part, by the Army Research Office under Grants W911NF-14-1-0104, W911NF-21-1-0118, and W911NF-21-1-0126, the National Science Foundation under grants DMR-1451219, DMR-1708615, and OISE-1545907, and the U.S. Department of Energy, Office of Science, Office of Basic Energy Sciences, Materials Sciences and Engineering Division under Contract No. DE-AC02-05-CH11231 (Materials Project program KC23MP for the development of functional oxide materials and under Award Number DE-SC-0012375 for the development of thin-film ferroelectrics.

Last, I would like to thank my friends and family that saw me through the doctoral studies from start to finish and beyond. I was unequivocally certain that I could finish this program from the start, and you are the biggest reason why. My parents, my brother, Liz, and Jenn. I thank you for your unconditional love and support. Five years of my life went into this work, and every year had its special challenges that helped me become a better scientist and more importantly, a better person.

Table of Contents

Table of Contents	iii
List of Figures	vi
List of Tables	ix
List of Symbols	x
List of Abbreviations	xi
Chapter 1: Introduction to ferroelectric order	1
1.1. Basic definitions and materials	1
1.2. Origins of ferroelectricity	2
1.2.1. Spontaneous polarization	2
1.3. Epitaxial ferroelectric thin films	3
1.3.1. Strain	3
1.4. Electric fields in thin-film ferroelectrics	4
1.4.1. Janovec-Kay-Dunn scaling	5
1.4.2. Limits of ferroelectricity	5
1.5. Relaxor ferroelectrics	5
1.5.1. Slush model	6
1.6. Dissertation Goal and Organization	7
Chapter 2: Ferroelectrics in superlattice structures	9
2.1. Why superlattices?	9
2.2. Superlattice structure and behavior	9
2.2.1. Dielectric relaxation in layered structures	10
2.3. Energy landscapes of superlattice structures	12
2.3.1. Elastic energy	12
2.3.2. Electrostatic interactions and gradient energy	13
2.4. Relevant literature in ferroelectric superlattices	14
2.4.1. Improper ferroelectricity	14
2.4.2. Polar vortex and skyrmion structures	15
Chapter 3: Synthesis and characterization of ferroelectric superlattice structures	17
3.1. RHEED-assisted pulsed-laser deposition	17
3.1.1. Pulsed-laser deposition	17
3.1.2. Growth mechanisms	19
3.1.3. Reflection high-energy electron diffraction	20
3.1.4. RHEED for film optimization: the SrTiO ₃ prototype	21

3.2.	Fabrication of device structures	23
3.3.	Structural characterization of ferroelectric superlattice structures	24
3.4.	Electrical characterization of ferroelectric superlattice structures	26
3.4.1.	Hysteretic response and beyond	26
3.4.2.	Dielectric response	27
3.4.3.	Rayleigh studies of ferroelectric materials	28
3.4.4.	Relaxor ferroelectrics: Vogel-Fulcher analysis	29
Chapter 4: Enhanced dielectric and ferroelectric properties in $\text{PbZr}_{1-x}\text{Ti}_x\text{O}_3$ superlattice structures		30
4.1.	Introduction	30
4.2.	Morphotropic-phase boundary	31
4.3.	Compositional tuning	31
4.4.	Superlattice structures	32
4.5.	Periodicity-dependent dielectric enhancement	34
4.6.	Periodicity-independent polarization saturation	38
4.7.	Pushing the limit of dielectric Rayleigh studies	39
4.8.	First-order reversal curve analysis	40
4.9.	Conclusions	43
Chapter 5: Artificial relaxor behavior in $(\text{BaTiO}_3)_n/(\text{SrTiO}_3)_n$ superlattices		44
5.1.	Introduction	44
5.2.	Prior art in the $\text{Ba}_{1-x}\text{Sr}_x\text{TiO}_3$ system	45
5.3.	Experimental superlattices – growth and structure	45
5.4.	Relaxor behavior in electrical response	49
5.5.	Molecular dynamics simulations	51
5.6.	Conclusions	55
Chapter 6: Beyond ferroelectric order: ferromagnetic order and interfacially-driven behavior ...		56
6.1.	Ferromagnetic order in ultra-thin LaCrO_3	56
6.1.1.	Initial LaCrO_3 deposition and orbital occupation	58
6.1.2.	Band alignment and beyond	58
6.2.	Optically tunable exotic ferroic phases	60
6.2.1.	Next challenges in emergent charge-ordered insulating phase	61
Chapter 7: Summary of findings and directions for future work		64
7.1.	Summary of findings	64
7.2.	Directions for future work	65
7.2.1.	Tri-component superlattices	65

7.2.2. Superlattice asymmetry	66
7.2.3. Strain control and measurement direction.....	67
References.....	70
Appendix A: RHEED-assisted PLD conditions	81

List of Figures

- 1.1. Schematic of a complex oxide perovskite unit cell with formula ABO_3 .
- 1.2. Dielectric anomaly of a ferroelectric material as it undergoes a structure phase transition at the Curie temperature T_C .
- 1.3. Polarization-electric field hysteresis behavior of a ferroelectric material.
- 1.4. Schematic of (a) cubic perovskite with (b) distortion creating an electric polarization and consequent depolarization field.
- 1.5. Frequency dispersion in the temperature-dependent permittivity maxima, as typically observed in relaxor ferroelectric materials.
- 1.6. Schematic of relaxor-ferroelectric in the polar nano region model (adapted from [Takenaka 2017]).
- 2.1. Schematic of a $(BaTiO_3)_{16}/(SrTiO_3)_{16}$ structure superlattice structure with HR-STEM overlay demonstrating the ability to control atomically-precise epitaxial layers.
- 2.2. Maxwell-Wagner polarization demonstrates a key signature through a large imaginary component of dielectric permittivity at low (<100 Hz) frequencies.
- 2.3. Strain phase diagram for a standard tetragonal ferroelectric material. Out-of-plane domains are stabilized with compressive strain (negative lattice mismatch) and in-plane domains are stabilized with tensile strain (positive lattice mismatch).
- 2.4. Improper ferroelectricity is observed in a short-period $(PbTiO_3)_n/(SrTiO_3)_n$ superlattice through the coupling of (a) ferrodistorptive and (b,c) antiferrodistorptive instabilities.
- 3.1. Schematic depicts pulsed-laser deposition in a vacuum chamber.
- 3.2. Schematic of (a) island (b) layer-by-layer and (c) layer-plus-island thin film growth modes.
- 3.3. Reflection high-energy electron diffraction monitors thin film deposition in situ.
- 3.4. (a,b) RHEED-assisted stoichiometry optimization of $SrTiO_3$ deposition in molecular beam epitaxy (adapted from [2017 Zhang]). (c) Stoichiometry optimization in pulsed-laser deposition using laser fluence.
- 3.5. Schematic depiction of parallel-plate capacitor structures used to measure (a) standard electrical measurements and (b) temperature-dependent measurements.
- 3.6. Voltage profile used to measure ferroelectric hysteresis.
- 3.6. A standard symmetric θ - 2θ scan of a superlattice demonstrating both superlattice and thickness fringes related to their respective thicknesses.
- 3.8. A series of minor hysteresis loops at increasing reversal fields (E_r), with coercive field (E_c) and bias field (E_B) highlighted.
- 3.9. Rayleigh behavior in ferroelectric materials is illustrated in three distinct regions (adapted from [1999 Stevenson]).
- 4.1. The phase diagram of the $PbZr_{1-x}Ti_xO_3$ system with vertical bars indicating selected parent compositions.
- 4.2. A series of $(PbZr_{0.8}Ti_{0.2}O_3)_n / (PbZr_{0.4}Ti_{0.6}O_3)_m$ superlattices with varying average composition. The ratio $n \times m$ was adjusted while $n + m = 12$ u.c. was held constant. (a) θ - 2θ X-ray scans and (b) dielectric permittivity reveals phase boundary-like behavior at an average mole fraction of $PbTiO_3$ of 47, as in $PbZr_{0.53}Ti_{0.47}O_3$.

- 4.3. (a) RHEED-assisted PLD of heterostructures demonstrates persistent layer-by-layer deposition and sharp interface control. (b) STEM image of the superlattice structure with overlaid EDS mapping of Ti and Zr. (c) A lower-resolution image across a wide area of the heterostructure, here for a $n = 8$ superlattice, reveals (d) smooth interfaces with no apparent defect structures.
- 4.4. (a) Full-range θ - 2θ X-ray diffraction patterns about the 002-diffraction condition for superlattices of various periodicities and accompanying reference films demonstrate excellent epitaxial crystalline quality. (b) θ - 2θ X-ray diffraction patterns about the 002-diffraction condition demonstrate precise superlattice control.
- 4.5. Reciprocal space maps about $(103)_{pc}$ indicate slightly larger c/a ratio for (a-c) parent phases compared to (d-h) superlattices and (i) bilayer on the same substrate, consistent with trends in ferroelectric polarization saturation.
- 4.6. Dielectric response: (a) permittivity and (b) loss show a variety of permittivities while maintaining low-loss. (c) Summarized dielectric response demonstrates an enhancement at a critical superlattice unit $n = 4$ unit cells. (d) Rayleigh dielectric measurements at sub-switching fields.
- 4.7. Low- and Rayleigh-regime measurements for reference samples: parent phases, bilayer heterostructures, and phase-boundary composition.
- 4.8. Transition temperatures as indicated by dielectric permittivity are persistent at 500 °C between (a),(b) parent phases and (c) 4 x 8 superlattice.
- 4.9. Ferroelectric current-voltage behavior for (a-b) single layer parent films, (c-g) superlattices with longer periodicity up to a (h) bilayer film taken at 10 kHz. Polarization and current are simultaneously shown to show constant polarization saturation and varying mixed-step intensities as superlattice periodicity increases.
- 4.10. Dielectric Rayleigh measurements employed at switching fields indicate split switching behavior in (a),(b) dielectric permittivity. (c) Reference parent phases require a large AC field strength (50-90 kV cm⁻¹) whereas the single-layer PbZr_{0.52}Ti_{0.48}O₃ exhibits switching at a smaller AC field strength (15-40 kV cm⁻¹). (d) Superlattice samples exhibit a varying proportion of small and large AC field switching events as a function of periodicity.
- 4.11. Minor loops from which FORC plots are extracted.
- 4.12. Polarization-electric field hysteresis measured between a negative saturation field and increasing positive reversal fields for (a) a reference single-layer film and (b-d) corresponding FORC contour plots. (e) Bilayer heterostructure shows two distinct switching events. (f) Superlattice minor loops are analyzed with (g-j) FORC to reveal a third switching event at high coercive fields for various periodicities.
- 4.13. (a) The evolution of peak intensities for various FORC distributions as a function of superlattice periodicity. (b) Schematic representation of the evolution of peak intensities for various FORC distributions wherein an increasing phase-boundary-like green peak (corresponding to volume fraction) with decreasing superlattice periodicity (n).
- 5.1. (a) RHEED-assisted PLD of (BaTiO₃)₁₆/(SrTiO₃)₁₆ demonstrates persistent layer-by-layer deposition control. (b) θ - 2θ X-ray diffraction patterns about the 002-diffraction condition for various superlattice periodicities (n). (c) HAADF-STEM image confirming sharp deposition control in (BaTiO₃)₁₆/(SrTiO₃)₁₆.

- 5.2. Off-axis reciprocal space maps about the 103_{pc} -diffraction condition demonstrate coherent strain for all $(\text{BaTiO}_3)_n/(\text{SrTiO}_3)_n$ superlattice structures to the GdScO_3 substrate. Superlattice fringes varying in spacing along $Q_x = 0$ according to the periodicity n of each structure.
- 5.3. On-axis reciprocal space maps about the 002_{pc} -diffraction condition show periodic out-of-plane features as seen in the line scan at the same diffraction condition (Figure 1b). With no detectable peaks at $Q_x \neq 0$, no in-plane periodic features are observed.
- 5.4. (a) Hysteresis loops demonstrate no significant remanent hysteresis across all superlattices and single-layer $\text{Ba}_{0.6}\text{Sr}_{0.4}\text{TiO}_3$. (b) Frequency-disperse temperature-dependent dielectric permittivity maxima are (c) fitted to the Vogel-Fulcher relation. (d) Vogel-Fulcher fitted parameters are tabulated for $(\text{BaTiO}_3)_n/(\text{SrTiO}_3)_n$ superlattices in addition to $\text{Ba}_{0.6}\text{Sr}_{0.4}\text{TiO}_3$ and literature values for $\text{Pb}(\text{Mg}_{0.33}\text{Nb}_{0.67})\text{O}_3$ (PMN), $0.7\text{Pb}(\text{Mg}_{0.33}\text{Nb}_{0.67})\text{O}_3$ - 0.3PbTiO_3 (PMN-PT), and $\text{CaCu}_3\text{Ti}_4\text{O}_{12}$.
- 5.5. Low-temperature hysteresis loops at 80 K, 10 kHz demonstrate a lack of significant remanent polarization for superlattice samples ($n = 4, 6, 8, 10, 12, 16, 20$) in contrast to a remanent polarization $P_r = 11 \mu\text{C cm}^{-2}$ for $\text{Ba}_{0.6}\text{Sr}_{0.4}\text{TiO}_3$. Stronger non-linearity is demonstrated in shorter-period superlattices, maintaining the same trend from room-temperature hysteretic response.
- 5.6. Temperature-dependent dielectric permittivity from 1 kHz to 1 MHz for $\text{Ba}_{0.6}\text{Sr}_{0.4}\text{TiO}_3$ demonstrates negligible frequency dispersion across a Curie temperature of 165 K.
- 5.7. Capacitance – voltage measurements up to applied dc field strengths of 125 kV cm⁻¹ demonstrate an increase in tunability at shorter superlattice periodicities. Long-period superlattices display a tunability of the dielectric permittivity near 0% and the short-period $n = 4$ superlattice shows a tunability of 24%. Low-loss tangents (<0.05) are consistent for all measurements.
- 5.8. Dipolar configuration-temperature stability diagram for (top) $n = 4$, (middle) $n = 6$, and (bottom) $n = 16$. $n = 4$ has two dipolar configuration transitions ≤ 90 K whereas the lowest phase transition temperature for $n = 6$ is 130 K. Qualitatively defining T_f as the temperature above which the relaxor-like phase is stable, the results show that $n = 4$ freezes at a lower temperature (90 K) than $n = 6$ (130 K) and $n = 16$ (>170 K), which agrees with the fitted Vogel-Fulcher parameters.
- 5.9. Same decrease in the average polarization of the BaTiO_3 layers upon heating for $n = 4$ and 6.
- 5.10. Wavelet-based estimator of the polar noise standard deviation (σ_{PN}). (a) 2D discrete wavelet transform of schematic, 2D dipolar configurations for a ferroelectric, paraelectric, relaxor at some time t , and the same relaxor some time later $t+\Delta t$. Time-averaged, layer-resolved σ_{PN} for the (b) $n = 4$, (c) $n = 6$, and (d) $n = 16$ superlattices at different temperatures. σ_{PN} and $\Delta\sigma_{PN}$ quantify spatial and temporal order, respectively.
- 6.1. Charge layers in an oxide perovskite ABO_3 structure along the [001]. Alternating positive negative and positive charges in the AO^+ and BO^- layers build up potential in proximity to nonpolar layers, leading to a polar discontinuity and polar catastrophe.
- 6.2. Reflection high-energy electron diffraction of LaCrO_3 grown epitaxially in the layer-by-layer growth mode on SrTiO_3 . Persistent oscillations and streaky pattern (inset) demonstrate excellent thin-film deposition *in situ*.

- 6.3. X-ray absorption spectra of Cr $L_{3,2}$ edges of a 30 nm LaCrO_3 film demonstrating a Cr^{3+} oxidation state in agreement with reference spectra.
- 6.4. (a) Band alignment of the $\text{LaAlO}_3/\text{SrTiO}_3$ heterostructure demonstrates electron accumulation in the SrTiO_3 . Prior work from the group demonstrates (b) an electron accumulation in LaMnO_3 and (c) ferromagnetism by observation of Mn XMCD of ultrathin $\text{LaMnO}_3/\text{SrTiO}_3$ heterostructures. (d) $\text{LaCrO}_3/\text{SrTiO}_3$ should have electron accumulation in LaCrO_3 .
- 6.5. The evolution of $\text{La}_{1-x}\text{Ca}_x\text{MnO}_3$ lattice parameter as a function of calcium content. Relevant substrates are shown for reference.
- 6.6. (a) Reflection high-energy electron diffraction intensity oscillations during deposition of $\text{La}_{0.67}\text{Mn}_{0.33}\text{O}_3$ on SrTiO_3 (001). (b) θ - 2θ X-ray scans about the 002-condition show excellent epitaxial quality.
- 6.7. Resistivity versus temperature measurements with and without applied magnetic fields of (a) 20 nm LCMO on SrTiO_3 and (b) 30 nm LCMO on NdGaO_3 [Adapted from Zhang 2016].
- 6.8. (a) Schematic of the $\text{SrRuO}_3 / \text{La}_{0.67}\text{Mn}_{0.33}\text{O}_3 / \text{PbTiO}_3 / \text{La}_{0.67}\text{Mn}_{0.33}\text{O}_3 / \text{SrRuO}_3$ heterostructure. (b) θ - 2θ X-ray scans demonstrate excellent heterostructure growth on SrTiO_3 .
- 6.9. Reciprocal space maps of multi-layer heterostructures demonstrate (a) no periodic in-plane features at the 002-diffraction condition and (b) excellent epitaxial quality at the 103-diffraction condition.
- 7.1. (a) X-ray diffraction about the 002-diffraction condition demonstrating high-quality epitaxial (00 l)-oriented $(\text{BaTiO}_3)_n/(\text{SrTiO}_3)_m$ superlattices on 20 nm $\text{SrRuO}_3/\text{GdScO}_3$ (110) with thickness and superlattices fringes. (b) Dielectric permittivity and loss for $n, m = 6, 4$ and $6, 6$, with larger permittivity in the shorter periodicity.
- 7.2. (a) X-ray diffraction about the 002-diffraction condition demonstrating high-quality epitaxial (00 l)-oriented $(\text{BaTiO}_3)_{10}/(\text{SrTiO}_3)_{10}$ superlattices on NdScO_3 , SmScO_3 , and GdScO_3 (110) substrates with thickness and superlattices fringes. (b) Dielectric permittivity trending upward with decreasing substrate size, with corresponding loss tangents. (c) Frequency- and temperature-dependent dielectric permittivity from 500 Hz to 1 MHz and (d) corresponding loss tangents.

List of Tables

- 4.1. Dielectric Rayleigh parameters of various single-layer films and heterostructures.

List of Symbols

a_f	Film lattice constant
a_s	Substrate lattice constant
C_0	Geometric factor (Maxwell-Wagner)
D	Displacement
D	Diffusivity
d	Film thickness
d	lattice spacing
d_{nn}	nearest neighbor lattice distance
E	Electric field
E_a	Activation energy
E_C	Coercive field
F	Free energy
f	Lattice mismatch
L	Kinetic coefficient
m	number of unit cells
n	order of reflection
n	number of unit cells
P	Polarization
P_r	Remnant polarization
P_S	Saturation polarization
r	Spatial coefficient
R	Resistance
T	Temperature
t	Temporal coefficient
T_b	Burns temperature
T_C	Curie temperature
T_f	Freezing temperature
T_{max}	Temperature of maximum dielectric constant
T^*	Intermediate temperature
V	Volume
Q_x	Reciprocal lattice vector (in-plane)
Q_y	Reciprocal lattice vector (out-of-plane)
ε	Dielectric permittivity
λ	X-ray wavelength
τ	Characteristic relaxation time
θ	Diffraction angle
ω	Frequency
ω	Diffraction angle
γ	Interfacial energy

List of Abbreviations

CVD	Chemical vapor deposition
DWT	Discrete wavelet transform
HR-STEM	High-resolution-scanning transmission electron microscopy
JKD	Janovec–Kay–Dunn law
LCMO	$\text{La}_{0.67}\text{Ca}_{0.33}\text{MnO}_3$
MBE	Molecular beam epitaxy
MPB	Morphotropic phase boundary
NPT-BVMD	Isobaric-isothermal ensemble-bond-valence molecular dynamics
PLD	Pulsed-laser deposition
PMN-PT	$(1-x)\text{PbMg}_{1/3}\text{Nb}_{2/3}\text{O}_3-(x)\text{PbTiO}_3$
PNR	Polar nano regions
PVD	Physical vapor deposition

Chapter 1

Introduction to Ferroelectric Order

This Chapter introduces the ferroelectric order parameter in complex oxide thin films. The origins of ferroelectricity are covered to provide a contextualization for the various methods used to measure, alter, and analyze ferroelectric materials throughout this work. First, I will cover the order parameter upon which ferroelectrics are defined, spontaneous polarization. Next, classical ferroelectric materials and their differences will be described. I will then highlight the effects on ferroelectric order when a material is limited to the dimensions of a thin film, which will lead to the limits of ferroelectricity in ultrathin films. Lastly, I will cover relaxor ferroelectrics, which demonstrate marked differences in structure and electronic response from standard ferroelectrics.

1.1. Basic definitions and materials

A ferroelectric material is defined as an insulating material with a spontaneous electric polarization in at least two directions. An applied external electric field can switch the direction of the electric polarization, and the material then maintains that polarization (or a good fraction thereof) upon removal of the external field. Ferroelectrics undergo a structural phase transition from a high temperature paraelectric nonpolar phase into a low temperature ferroelectric polar phase. This work focuses on ferroelectric materials with the widely used complex oxide perovskite structure with generic chemical formula ABO_3 (Figure 1.1).

Classical ferroelectric materials such as $BaTiO_3$, $PbTiO_3$, and $BiFeO_3$ have this structure. $BaTiO_3$ was the first perovskite ferroelectric material discovered¹, and it goes through several phase transitions. The high-temperature non-polar cubic phase transitions to tetragonal, orthorhombic, and then rhombohedral polar phases when cooled, with polarization directions along the $[001]$, $[110]$, and $[111]$, respectively. $BaTiO_3$ has a spontaneous polarization of $30 \mu C cm^{-2}$, which is smaller than the $75 \mu C cm^{-2}$ associated with another other classic system, $PbTiO_3$. $PbTiO_3$ has not found widespread utility in applications due to large concentrations of defects and their associated conduction, but doped versions and solid solutions including this material have been the focus of research and application.

One such notable material is $PbZr_{1-x}Ti_xO_3$, which is the solid solution between $PbTiO_3$ and $PbZrO_3$, an antiferroelectric material. Antiferroelectric materials have displacements between unit cells oppositely aligned in an antiparallel order. This system also exhibits a morphotropic phase boundary (MPB), which is a nearly-temperature-independent phase transition. The MPB occurs at the chemistry $PbZr_{0.52}Ti_{0.48}O_3$, and has been the focus of research efforts and applications due to the simultaneous

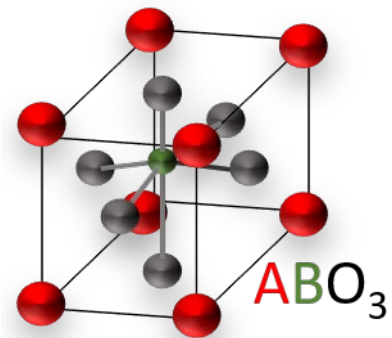


Figure 1.1. Schematic of a complex oxide perovskite unit cell with formula ABO_3 .

presence of enhanced dielectric and piezoelectric susceptibilities at this composition. This work focuses on BaTiO_3 and $\text{PbZr}_{1-x}\text{Ti}_x\text{O}_3$, wherein ultra-thin versions of these materials are sandwiched together to explore how advanced materials design can result in enhanced properties.

1.2. Origins of ferroelectricity

From a structural perspective, ferroelectricity stems from a shift in the B -site cation and oxygen anions away from the positions associated with a center of symmetry in the unit cell. Thus, structural symmetry is broken below a transition temperature and the net displacement results in a net polarization. This transition is denoted by the Curie temperature (T_C), at which the structure transitions from a high-temperature nonpolar phase into a low-temperature polar phase with associated large dielectric susceptibility and spontaneous polarization². Various susceptibilities,

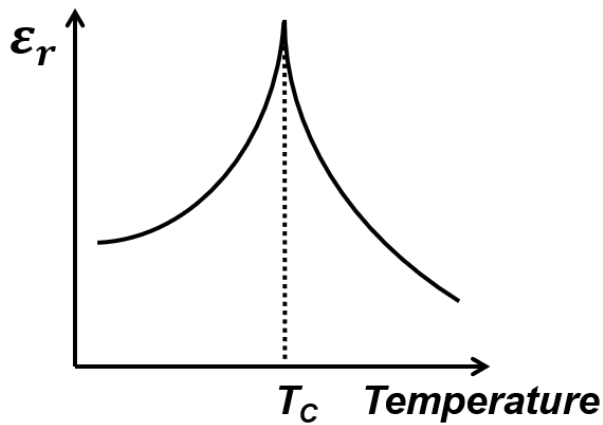


Figure 1.2. Dielectric anomaly of a ferroelectric material as it undergoes a structure phase transition at the Curie temperature T_C .

such as the dielectric permittivity, spike at this structural transition (Figure 1.2).

From a chemical perspective, ferroelectricity stems from the competition of forces that favor a centrosymmetric versus non-centrosymmetric structure. These forces are long-range Coulombic forces stemming from the ionic insulators that make up ferroelectrics, and local short-range repulsive forces between these ions³. The second-order Jahn-Teller effect describes the stabilization of a non-centrosymmetric structure by hybridization of orbitals in ferroelectric materials^{4,5}. In the case of BaTiO_3 , oxygen $2p$ and titanium $3d$ orbitals hybridize resulting in a displacement of the B -site cation away from the center of the unit cell⁶. In the case of PbTiO_3 , lone pair $6s$ electrons on the A -site cation further distort the structure by hybridizing with the oxygen $2p$ orbitals⁷.

From a physics perspective, ferroelectricity stems from the softening of phonons modes in a structure⁸. Instabilities of the order parameter, which in the case of a ferroelectric material is spontaneous polarization, follow the condensation of a vibrational mode of the lattice⁹. In a ferroelectric, transverse optical vibrations soften at the Brillouin zone center, wherein the wave vector is zero and the corresponding wavelength of this mode asymptotes to infinity. Thus, a region of homogeneous lattice distortions and polarization extends infinitely. This is opposite to an antiferroelectric, wherein transverse optical vibrations soften at the Brillouin zone edge, and therefore lattice distortions are opposite to adjacent distortions. This leads to antiparallel alignment of neighboring unit cells and a net zero polarization at a macroscopic average.

1.2.1. Spontaneous polarization

Polarization is measured by the hysteretic nature of a polarization-electric field hysteresis loop taken by application of an external electric field to a ferroelectric capacitor. Applying a field in one direction will pole the ferroelectric in one direction, and reversal of the field direction will pole the ferroelectric in the opposite direction. When a ferroelectric material switches, the current through the material spikes, which is integrated to calculate the polarization, P (Figure 1.3). The electric field required to switch a ferroelectric is denoted by the coercive field, E_C . This field is not always symmetric about zero field depending on the electrostatic boundary conditions and contacts of the system, thus one can use the average between the negative and positive versions of this value. Further application of stronger electric fields beyond the coercive field results in a saturation of the polarization, which can be traced back to zero field for the saturation polarization value, P_S . Decreasing the field to zero will decrease the remnant polarization, P_r through back-switching due to defects¹⁰. The degree of back-switching can be related to the difference between the saturation and remnant polarization values.

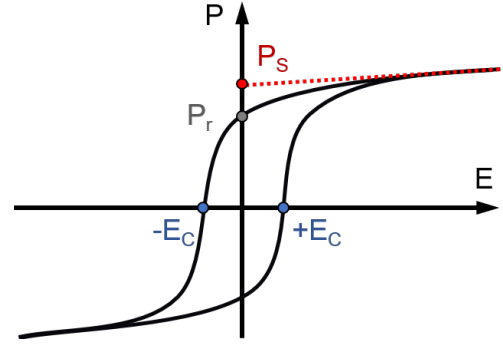


Figure 1.3. Polarization-electric field hysteresis behavior of a ferroelectric material.

The polarization-electric field loop can be interpreted as the displacement of the B -site cation, wherein the displacement D relates to the electric field E and polarization P by:

$$D = \varepsilon E + P \quad (1.1)$$

with the permittivity ε related to the magnitude of displacement due to the applied field. The permittivity is proportional to the slope of the hysteresis loop, wherein a large slope corresponds to a large displacement in response to an applied field.

1.3. Epitaxial ferroelectric thin films

Thin-film epitaxy provides the ability to engineer ferroelectric materials with precise strain and size effects. Strain can enhance and induce ferroelectricity in materials by, for example, compressively straining the in-plane lattice constants of a material and inducing an expansion in the out-of-plane direction that promotes out-of-plane oriented polarization. Strain can tune the T_C in ferroelectric oxides by stabilizing or destabilizing the ferroelectric phase¹¹. Thin-film versions of materials also scale down coercive fields, opening a pathway toward low-voltage operation and future applications.

1.3.1. Strain

Strain in thin films is typically given as a percentage in the lattice mismatch between film and substrate, with a negative number indicating compressive strain and a positive number indicating tensile strain. Lattice mismatch f is defined as:

$$f = \frac{a_s - a_f}{a_f} \times 100\% \quad (1.2)$$

where a_f and a_s correspond to film and substrate lattice constants. Lattice mismatch strain typically ranges from $-2\% \sim 2\%$ biaxial strain imposed by the substrate on the film, affecting a variety of physical properties of the film. In the scope of ferroelectric materials, the Curie temperature can be pushed by several hundred degrees or even induced in non-ferroelectric materials such as SrTiO_3 ^{11,12}. Many other properties can be tuned with strain, including remnant polarization¹³, dielectric susceptibilities¹⁴, etc. The structure-properties relationship of ferroelectric materials is leveraged to improve their utility in applications.

In a tetragonal ferroelectric structure, the strain is typically calculated by taking the high-temperature cubic version of the material and linearly approximating the lattice constant down according to the thermal expansion of the material. A variety of substrates are utilized in ferroelectric oxide epitaxy, with emphasis on materials that can closely lattice-match bulk constants in the range of 3.8-4.05 Å. Standard substrates include SrTiO_3 , LaAlO_3 , and DyScO_3 among others¹¹. Crystal lattice planes are typically indexed in a cubic lattice. For this reason, some substrates denote a pseudocubic lattice parameter, specifically in the case of GdFeO_3 -type orthorhombic substrates such as rare-earth scandates ReScO_3 . The $[110]_O$ of an orthorhombic substrate aligns with the $[001]$ of a cubic film (Appendix A). Through conversion to a pseudocubic lattice, orthorhombic substrates are typically not square in-plane and can lead to preferential in-plane directions of ferroelectric phases.

1.4. Electric fields in thin-film ferroelectrics

The displacement of the B -site cation under applied field produces a dipole moment in a ferroelectric. The internal dipole moment causes a build-up of opposite charges at surfaces perpendicular to the dipole moment of a ferroelectric. This is called the depolarization field, which works against the displaced cations and destabilizing the polarization (Figure 1.4). In capacitor structures, the depolarization field is typically screened by the presence of metallic electrode materials used as contacts. When the depolarization field is not properly screened, the electrostatic energy associated with the residual depolarization field can counteract the energy associated with the non-centrosymmetric ordering and the polarization of a ferroelectric can diminish or vanish entirely.

Factors that affect the depolarization field include the electrode-ferroelectric interface, ferroelectric domains, and more¹⁵. Externally, the electrode-ferroelectric interface requires compensation by a metallic electrode.

Conducting perovskites such as SrRuO_3 have become commonplace in this application due to their matching perovskite structure, interfacial chemistry, and lattice parameter for strain-engineering thin films¹⁶⁻¹⁹. Internally, ferroelectric

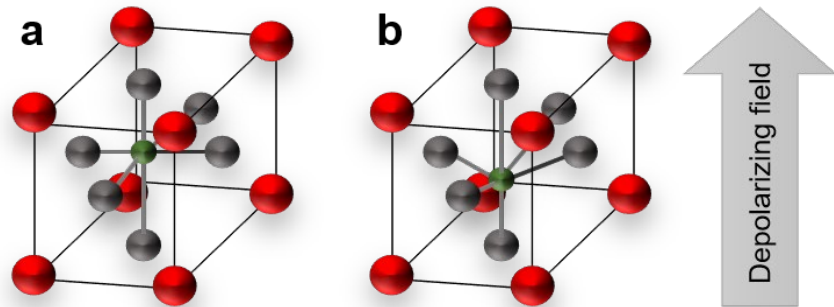


Figure 1.4. Schematic of (a) cubic perovskite with (b) distortion creating an electric polarization and consequent depolarization field.

domains can reduce the depolarization field. In thin-film ferroelectrics, the depolarization field can even shift non-centrosymmetric cations back into their centrosymmetric position and cause ferroelectric order to vanish.

1.4.1. Janovec-Kay-Dunn scaling

An intrinsic size-effect relevant in thin-film ferroelectrics is the Janovec–Kay–Dunn (JKD) law;

$$E_C \propto d^{-2/3} \quad (1.3)$$

wherein the coercive field E_C scales with film thickness d . The original empirical observations were based on ferroelectric crystals in the 1960s, but this relation holds for thin films ranging from 100 μm down to 100 nm ²⁰⁻²². This scaling law works against the decreasing total field required to switch a thinner film, and thus is a hurdle for potential ultra-thin applications. Deviations from JKD scaling have been reported in films thinner than 15 nm, wherein incomplete screening of the depolarization field was found to cause the deviation. The issue with thin films stems from the screening in the electrodes, and thus future research may require “better” metallic electrodes over the widely used SrRuO_3 . For applications in dynamic random-access memory, large capacitance is the key property of interest. For this application, ultra-thin devices need both; a more resistive ferroelectric component and more conducting electrodes²³. As thin films get smaller, depolarization fields become increasingly relevant.

1.4.2. Limits of ferroelectricity

Depolarization field is attributed with the disappearance of ferroelectric order in ultra-thin materials, reportedly on the order of 4-6 unit cells²⁴. This limit depends on the charge screening provided by the electrode. Some work has observed a ferroelectric structure in PbTiO_3 down to 3 unit cells ($\sim 12 \text{ \AA}$)²⁵, wherein no electrode was grown and the ferroelectric phase was confirmed by X-ray diffraction studies only. Given that these systems are relevant for their application in electronic systems, integration into devices is important. The orientation of the ferroelectric polarization is also key, wherein size effects are most prominent in out-of-plane polarization. Thin films with in-plane polarization can extend much longer distances in the a - b plane. In superlattice systems, ferroelectric layers 4-6 unit cells thick are typically grown with dielectric layers in repeating units, combining to 100 nm total thickness between electrodes. In these scenarios, size effects can be introduced into the system while still circumventing the devastating effects of depolarization fields on ferroelectricity.

1.5. Relaxor ferroelectrics

Relaxor ferroelectrics have garnered interest in recent years due to their high dielectric permittivity over a large temperature range and large electromechanical response such as piezoelectric coefficients²⁶. They are strong candidates for future applications in energy harvesting sensors, and energy storage^{27,28}. Relaxors are a type of ferroelectric characterized by three main factors; lack of remnant polarization, a broad dielectric peak about the transition temperature, and

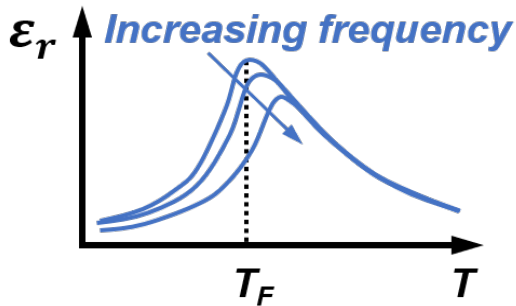


Figure 1.5. Frequency dispersion in the temperature-dependent permittivity maxima, as typically observed in relaxor ferroelectric materials.

relaxors do not follow Curie-Weiss behavior above T_{max} ^{26,29}, and they do not linearly follow the Arrhenius equation of frequency-dependent T_{max} ^{30,31}. Instead, relaxors follow the Vogel-Fulcher relation, which was initially introduced to explain glassy transitions^{30,32,33}.

Relaxors are typically characterized by chemical heterogeneity, wherein a solid solution such as $(1-x)\text{PbMg}_{1/3}\text{Nb}_{2/3}\text{O}_3-(x)\text{PbTiO}_3$ (PMN-PT) provides site and charge disorder that result in a wide distribution of relaxation times³⁴. This definition for relaxor materials is still debated in the community today, wherein certain characteristic temperatures and polar nano regions (PNRs) are used with caution to describe relaxor behavior. Relaxors can be structurally investigated by diffuse-scattering, wherein X-ray and neutron diffraction-based scattering techniques have been used to study structural signatures of relaxors³⁵⁻³⁷. The shapes and profiles of these patterns are used to quantitatively extract polarization correlation lengths, wherein butterfly shape in a diffuse-scattering pattern is indicative of many small domains with a high density of low-angle domain walls.

1.5.1. Slush model

Relaxor ferroelectrics with polar structures in a multi-domain state have been related to a slush-like state akin to water, wherein regions of polarization such as PNRs are transiently slushing around in a non-polar matrix³⁸. These regions are modulated in size, frequency response, and correlation with temperature. Specific phase transitions describe the appearance, growth and freezing of PNRs as a material is cooled from a high temperature. These transitions are denoted by the Burns temperature T_b , intermediate temperature T^* , and freezing temperature T_f . As a material is cooled below the Burns temperature, thermal excitation leads to dynamically-correlated polarization fluctuations (Figure 1.6)^{38,39}. Upon further cooling, these correlations become stronger to the point

frequency dispersion of the dielectric peak. The temperature at which the maximum dielectric permittivity is observed is denoted by T_{max} , which is dependent on the frequency of the applied ac field in a permittivity measurement. At a frequency of zero, this becomes the freezing temperature T_F . The freezing temperature T_f is at a lower temperature than T_{max} because T_{max} denotes the freezing out of some polar domains, with the limit of all polar domains freezing out at a frequency of 0 at T_f . Permittivity behavior in relaxors deviates from standard ferroelectric characteristics as follows:

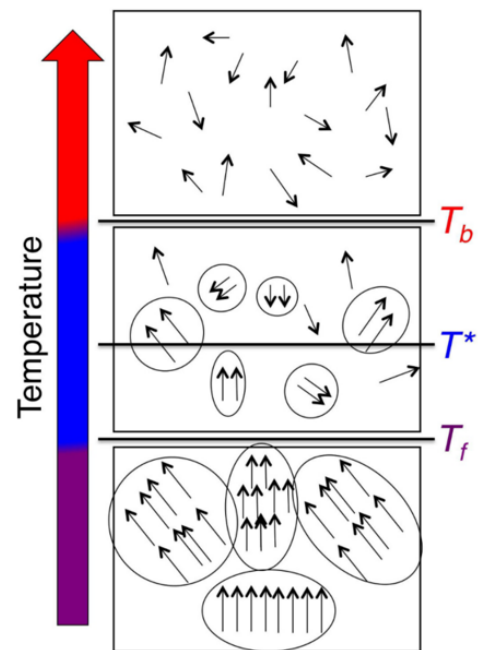


Figure 1.6. Schematic of relaxor-ferroelectric in the polar nano region model (adapted from [Takenaka 2017]).

where static displacements appear at the intermediate temperature. With more cooling, regions of static cation displacement (PNRs) increase in size and relaxation time^{40,41}. This eventually leads to the freezing of PNRs, wherein the smallest clusters with shortest relaxation time freeze out first and the largest and slowest regions freeze at the freezing temperature. Below this, all the polar regions are frozen into large, static regions of ferroelectric polarization. Thus, as the distribution of PNRs begin to freeze out, the permittivity of the system displays a frequency dispersion related to the distribution of PNR size and relaxation time. T_{max} in this model does not describe a phase transition, but instead the increasing proportion of frozen PNRs as a relaxor cools between the intermediate and freezing temperatures.

1.6. Dissertation Goal and Organization

The goal of this dissertation is to study the evolution of ferroic order parameters in oxide heterointerfaces. Mainly focusing on ferroelectric order, I analyze how ultra-thin layers of ferroelectric materials interact with other ferroelectric, dielectric, and metallic layers from structural and electronic perspectives to produce enhanced properties and novel phases. I focus on ferroelectric materials such as $\text{PbZr}_{1-x}\text{Ti}_x\text{O}_3$ and BaTiO_3 to take standard ferroelectrics and drive them to limits of stability via chemical composition, strain, and superlattice design. This work is enabled by pushing materials design and characterization to their limits, combining unit-cell-precise deposition of ultra-thin layers with electrical characterization that goes beyond standard switching regimes in both Rayleigh dielectric measurements and hysteresis loops. This dissertation includes two specific research advances.

First, I use two compositions of $\text{PbZr}_{1-x}\text{Ti}_x\text{O}_3$ on either side of the MPB to provide an average macroscopic MPB composition with ultra-thin layers of stable rhombohedral and tetragonal phases. First-order reversal curve analysis reveals the presence of switching distributions for each parent layer and a third, interfacial layer wherein superlattice periodicity modulates the volume fraction of each switching distribution and thus the overall material response. This reveals that deterministic creation of artificial superlattices is an effective pathway for designing materials with enhanced responses to applied bias.

Second, I study the observation of and mechanism behind relaxor behavior in $(\text{BaTiO}_3)_m/(\text{SrTiO}_3)_n$ superlattice structures. Dielectric studies as a function of temperature reveal frequency dispersion of dielectric response which increases in magnitude as the periodicity decreases. Subsequent Vogel-Fulcher analysis confirms the frequency dispersion of the dielectric maxima across a range of periodicities and the presence of relaxor-like behavior which becomes more robust at shorter periods. Bond valence molecular dynamics simulations suggest that the relaxor-like behavior observed experimentally in shorter-period superlattices arises from temperature-driven size variations of antipolar stripe domains in contrast to more thermally stable dipolar configurations in longer-period superlattices.

The remainder of this dissertation will contain the following chapters:

Chapter 2 describes how ferroelectric have been leveraged in superlattice heterostructures in previous work to produce phenomena such as improper ferroelectricity, vortex and skyrmion structures, etc.

Chapter 3 provides an overview of synthesis techniques for thin film structures used throughout the rest of this work and its comparison to other techniques. It also summarizes the structural and electrical characterization principles and tools used to analyze ferroelectric superlattices.

Chapter 4 focuses on simultaneous large susceptibility and polarization in the $\text{PbZr}_{1-x}\text{Ti}_x\text{O}_3$ system as a function of superlattice periodicity. In this Chapter, I show that $(\text{PbZr}_{0.8}\text{Ti}_{0.2}\text{O}_3)_n/(\text{PbZr}_{0.4}\text{Ti}_{0.6}\text{O}_3)_{2n}$ superlattices exhibit a large volume fraction of MPB-like character at the interfaces, which enables large permittivity while remnant parent phases maintain large polarization.

Chapter 5 focuses on experimental and computational relaxor-like behavior, which is typically associated with chemical inhomogeneity/complexity in solid solutions, in atomically precise $(\text{BaTiO}_3)_n/(\text{SrTiO}_3)_n$ symmetric superlattices.

Chapter 6 describes interfacially-driven order beyond ferroelectricity, such as ferromagnetic order and the interplay of electrostatic boundary conditions of an ultra-thin ferroelectric order between a light-induced metal-to-insulator.

Chapter 7 provides an outlook to future directions for research in the area of ultra-thin ferroic layers, wherein specific degrees of freedom in superlattice design criteria can be leveraged to explore exotic materials phases and properties.

Chapter 2

Ferroelectrics in superlattice structures

This Chapter focuses on the basic components, special considerations, and advances in superlattices with respect to oxide ferroelectric thin films. First, research into superlattice structures is motivated by its unique potential in the field of oxide thin films, and important distinctions are made between superlattices and other layered materials. Next, the basic elements of superlattices are covered, including how an epitaxial superlattice appears under a microscope. The energy landscapes behind superlattices and oxide thin films in general are introduced, which, in turn, helps explain the unique opportunities that such structures in oxides can enable. Last, a summary of recent and existing superlattice work in the literature is given to contextualize how these design parameters have been leveraged in the past to exhibit novel phases and enhanced physical properties of materials.

2.1. Why superlattices?

Superlattices offer a powerful design element for engineering materials with enhanced and novel properties by engaging layers the length scales of relevant effects. By definition, superlattices are periodic (and repeating) structures of at least two different layered materials. Some oxides, in fact, crystallize naturally in layered structures such as double perovskites, Ruddlesden-Popper phases, and Aurivillius phases^{42,43}. These are typically made via a self-assembly process wherein alternating layers are formed a result of a variety of structural instabilities^{44,45}. A distinction between artificially designed superlattices and naturally self-ordered compounds is that self-ordered compounds rely on thermodynamic equilibrium in their synthesis to settle into stable or metastable states. Pulsed-laser deposition (PLD) is particularly effective at synthesizing materials away from equilibrium (**Chapter 3**), which opens a pathway for a multitude of layered materials to be synthesized. With the availability of diverse states near the ground state in oxide materials, pairing PLD with layered oxides is an excellent avenue to explore enhanced properties and novel phases.

Superlattices are related to heterostructures in that they both have various layers of different materials. However, the periodic repetition of layers differentiates a superlattice from a heterostructure. This periodic repetition makes it easier to be down to ultra-thin layer thicknesses and still maintain an overall film thickness of ~ 100 nm to easily measure properties and draw meaningful conclusions in comparison to single-layer films. Getting down to ultra-thin layer thicknesses is important for interplay with relevant effects such as the experimental limits of ferroelectricity and sizes of polar domains in ferroelectrics and relaxors.

2.2. Superlattice structure and behavior

High-quality superlattices can be designed at the atomic level with various degrees of freedom. Primarily, these include the composition of each layer, the thickness of each layer, the strain state imposed by a substrate, and any other layers such as electrodes. The thickness of each layer can be further classified by periodicity n (as in the number of unit cells), where a symmetric superlattice has the same number of unit cells for each component. Asymmetric superlattices contain different thicknesses of each constituent layer, denoted by n and m for each component in a two-component superlattice.

A standard superlattice design has a substrate that imposes strain (via lattice mismatch) on the superlattice structure. Electrode materials such as SrRuO_3 are typically deposited first as a bottom electrode to serve as a metallic contact for electrical measurements and help stabilize the growth of the layers above. An example of a superlattice studied in the current work and in the literature^{11,46-48} is $(\text{BaTiO}_3)_n/(\text{SrTiO}_3)_m$ (Figure 2.1). This is schematically represented in the basic design, with a high-resolution scanning transmission electron microscope (HR-STEM) image overlay. Unit-cell precision is shown here at the atomic level, wherein 16-unit-cell-thick superlattice layers are seen by their difference in Z-contrast through the barium and strontium A -site cations. Interfaces between these layers mix at minimal length scale (typically <2 -unit cells) and high-quality crystallinity can be seen extending from the substrate into film.

Superlattice design criteria allow for a wealth of structures that can enable one to probe, explore, and discover properties that are not possible to synthesize in the parent materials alone. Advances in growth processes have allowed for superlattices to become atomically precise, and the field today is increasingly focused not just on producing them, but characterizing and analyzing the primary functionality of these structures. This in work, the primary focus is on the dielectric and ferroelectric responses.

2.2.1. Dielectric relaxation in layered structures

Dielectric relaxation is the delay in material response to an external ac field wherein, over a range of frequencies, the dielectric constant of a material changes when certain components of the material can no longer respond quickly enough to said field. Dielectric materials will primarily

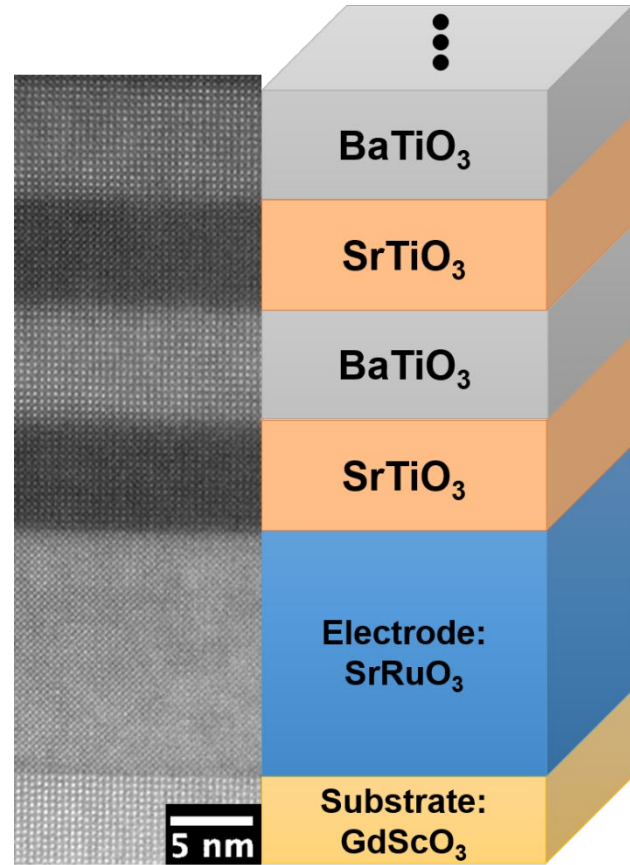


Figure 2.1. Schematic of a $(\text{BaTiO}_3)_{16}/(\text{SrTiO}_3)_{16}$ structure superlattice structure with HR-STEM overlay demonstrating the ability to control atomically-precise epitaxial layers.

respond to applied field by polarizing through several polarization mechanisms: electronic, ionic (or atomic), dipolar, and interfacial (space charges). Within these mechanisms, dipolar polarization is typically well-described by Debye relaxation. Debye relaxation assumes an ideal set of independent dipoles under an applied field and contains a single relaxation time for the population of dipoles in a material. This behavior describes the frequency-dependent relaxation of dipolar response to an applied field, and is broadly described by complex relative permittivity ε in the following relation:

$$\varepsilon = \varepsilon_{\infty} + \frac{\varepsilon_0 - \varepsilon_{\infty}}{1 + i\omega\tau} \quad (2.1)$$

with ε_{∞} and ε_0 corresponding to the permittivity at infinite and zero frequency, respectively. Here, ω is the frequency and τ is the characteristic relaxation time. Given that this is a complex value, the real (ε') and imaginary (ε'') parts of a Debye-type relaxation are defined as:

$$\varepsilon' = \varepsilon_{\infty} + \frac{\varepsilon_0 - \varepsilon_{\infty}}{1 + \omega^2\tau^2} \quad (2.2)$$

$$\varepsilon'' = \frac{(\varepsilon_0 - \varepsilon_{\infty})\omega\tau}{1 + \omega^2\tau^2} \quad (2.3)$$

Debye-type relaxation is observed as a drop-off in real permittivity as the frequency rises, with an associated peak in the imaginary permittivity at $\omega = \tau$. Debye-type relaxation is symmetric and sharp about the peak, with a single relaxation time for the entire material. In materials with a distribution of relaxation times, asymmetric and/or broad peaks in the imaginary permittivity are observed. Such relaxation is called Cole-Cole, Cole-Davidson, etc.

In the case of superlattices with dielectric materials, several reports have indicated Maxwell-Wagner relaxation. This type of relaxation is caused by interfacial polarization that stems from inhomogeneity in materials. More specifically, Maxwell-Wagner relaxation is caused by charge carrier migration to interfaces. This type of behavior can be introduced in a layered material with different dielectric constants and therefore different internal fields, causing space charges to accumulate at interfaces and bring about artificially enhanced response within limited frequency ranges. One way to analyze Maxwell-Wagner relaxation is to compare it to the simplest relaxation type, Debye relaxation. Real and imaginary component of the dielectric permittivity in a Maxwell-Wagner capacitor model are:

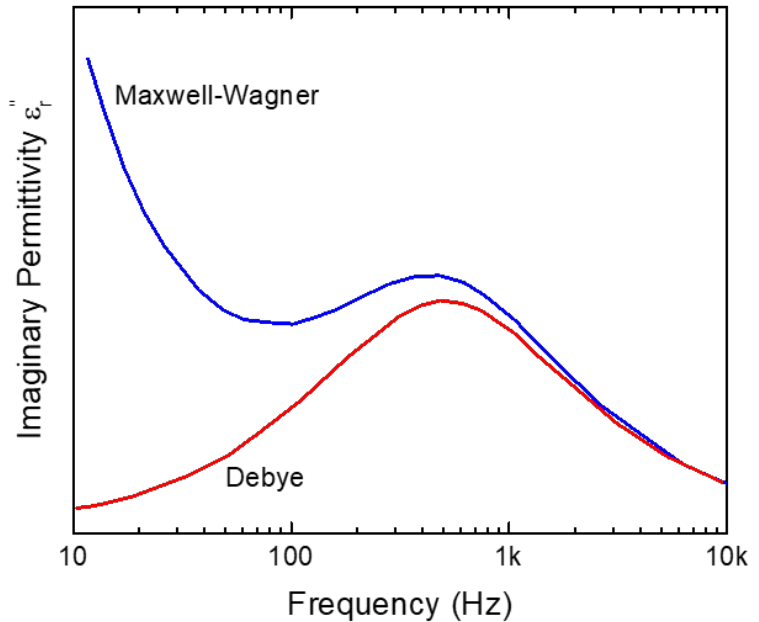


Figure 2.2. Maxwell-Wagner polarization demonstrates a key signature through a large imaginary component of dielectric permittivity at low (<100 Hz) frequencies.

$$\varepsilon' = \varepsilon_{\infty} + \frac{\varepsilon_0 - \varepsilon_{\infty}}{1 + \omega^2 \tau^2} \quad (2.4)$$

$$\varepsilon'' = \frac{1}{\omega C_0 (R_1 + R_2)} + \frac{(\varepsilon_0 - \varepsilon_{\infty}) \omega \tau}{1 + \omega^2 \tau^2} \quad (2.5)$$

wherein C_0 is a geometric factor and R_i is the resistance of each component (in a two-component system). Between Maxwell-Wagner and Debye relaxation, there should not be a notable difference in the real permittivity, but there is a notable difference in the imaginary permittivity. This difference is apparent in the limit of zero frequency, wherein the first term in Equation 2.5 is expected to rise sharply (Figure 2.2). This can be seen in previously reported data on Maxwell-Wagner relaxation in a $\text{Ba}_{0.8}\text{Sr}_{0.2}\text{TiO}_3/\text{Ba}_{0.2}\text{Sr}_{0.8}\text{TiO}_3$ superlattices⁴⁹. Maxwell-Wagner polarization is important to be aware of in superlattice structures because it can cause enhanced dielectric response in a material simply by space charge accumulation at interfaces^{50–53} instead of tuning the dielectric response of a material at the atomic level.

2.3. Energy landscapes of superlattice structures

Polarization is an important quantity to study in ferroelectrics because spontaneous polarization is the order parameter that defines ferroelectricity. Just as with spontaneous strain and magnetization in ferroelastics and ferromagnets, respectively, the order parameter in a ferroic material is critical to studying the evolution of a phase as various conditions are imposed. The evolution of polarization (P_i) in three dimensions can be modeled by solving the time-dependent Ginzburg-Landau equation:

$$\frac{\partial P_i(r,t)}{\partial t} = -L \frac{\delta F}{\delta P_i(r,t)} \quad (i = 1,2,3) \quad (2.6)$$

wherein r , t , and L correspond to the spatial, temporal, and kinetic coefficients of a system in three dimensions. In the scope of thin-film materials, the total free energy F :

$$F = \int (f_{\text{Landau}} + f_{\text{elastic}} + f_{\text{electric}} + f_{\text{gradient}}) dV \quad (2.7)$$

includes components of bulk (Landau), elastic, electric, and polarization gradient energies. The bulk Landau energy is the standard energy from a bulk material's composition. From bulk considerations, ferroelectric materials form domain structures upon cooling past the Curie temperature. In a standard tetragonal ferroelectric system, these domains will form in the [100], [010], and [001]. The relative volume fraction of each domain should be evenly split in the bulk, until other energies are thrown into the mix. Elastic energy is imposed by the substrate onto a film through epitaxy. Lastly, the gradient energy is the energy penalty associated with changing the magnitude or direction of a polar displacement. The following sections outline how the various considerations from each energy are factored into designing a ferroelectric superlattice.

2.3.1. Elastic energy

Elastic energy is imposed on a thin film through the lattice mismatch between substrate and film and can result in a dramatic change in the Curie temperature and saturation polarization of a ferroelectric among other effects⁵⁴. Elastic energy imposes a fixed elastic boundary condition on one side of a thin film, resulting in potentially highly anisotropic behavior^{55,56}. For starters, this results in a significant change in relative volume fraction of domains with out-of-plane versus in-

plane oriented polarization. When the lattice parameter of a substrate is larger than that of a substrate, the balance of domains is shifted to prefer domains with in-plane polarization. The opposite is also true for a smaller substrate leading to more domains with out-of-plane polarization. This all depends on the temperature, of course, with higher temperatures trending towards a paraelectric phase. Together, these behaviors can be collectively presented in a strain-temperature phase diagram for a standard multi-domain tetragonal ferroelectric material (Figure 2.3)⁵⁷. Here, compressive (negative) mismatch strain promotes the formation of domains

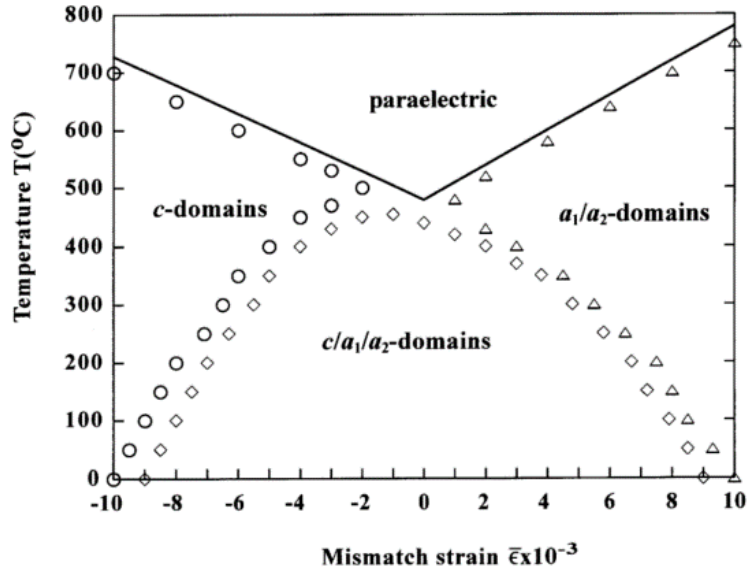


Figure 2.3. Strain phase diagram for a standard tetragonal ferroelectric material. Out-of-plane domains are stabilized with compressive strain (negative lattice mismatch) and in-plane domains are stabilized with tensile strain (positive lattice mismatch) (adapted from [Li 2002 Acta Materialia]).

with out-of-plane polarization, with a strain of -1.0% leading to a significant temperature range of an entirely out-of-plane polarized *c*-domain structure⁵⁸⁻⁶¹. At intermediate strain values, the temperature is important to note because a material could easily transition from paraelectric to all *c*-domains or *a*₁/*a*₂-domains to a mixed-phase within a couple hundred degrees. The relative position of these intersections is dependent on the material, but the same trends hold true for most tetragonal ferroelectric materials. In the scope of ferroelectric superlattices, elastic energy is a large contributor with respect to other terms and precise substrate selection is important for designing ferroelectric behavior.

2.3.2 Electrostatic interactions and gradient energy

Electrostatic interactions can affect the ferroelectric domain structure of a thin film. Applied external fields can promote the stability of domains in certain direction. In addition to applied external fields, the internal fields in a material also affect domains by reaching electrostatic equilibrium in a variety of scenarios. In general, the electric energy density *f* is given by:

$$f_{electric}(P_i, E_i) = -\frac{1}{2}E_i D_i = -\frac{1}{2}E_i(\epsilon_0 \epsilon_r E_i + P_i) \quad (2.8)$$

where *E*_{*i*} is the electric field, *P*_{*i*} is the polarization, ϵ_r is the relative permittivity, ϵ_0 is the permittivity of free space, and *D*_{*i*} is the displacement. This relation is explored in the context of thin films via two main scenarios of different electrical boundary conditions on the top and bottom of a film surface. The first electrostatic scenario is the so-called closed-circuit boundary condition, where the surface (or interface) of a film has its charge fully compensated by metals that are connected. In this scenario, constant electrical potential on the surface promotes the formation of

out-of-plane polarized c domains⁶². This is the case where good metallic contact is made by electrodes in a thin film. In the other scenario, so-called open-circuit boundary conditions, the potential on the surface is not compensated at the surface (as would be the case of a ferroelectric without metal electrodes on the surfaces). This leads to a build-up of charge at surfaces and consequent depolarization field. Depolarization field, as described in **Chapter 1**, reduces the polarization in the out-of-plane direction.

When extended to a ferroelectric superlattice, ultra-thin ferroelectric layers with no metallic contact to compensate for surface (or interface) charges can tend to push its polarization away from a c -domain structure into either a paraelectric (polarization vanishes), dense $c+/c-$ (up- and down-poled structure), or an a_1/a_2 -domain (polarization rotates to be fully in plan oriented). In either case, there is an energy associated with changing a polarization direction away from homogeneity. The energy of a domain wall is defined as:

$$f_{wall} = \frac{1}{2} G_{ijkl} P_{i,j} P_{k,l} \quad (2.9)$$

where the G_{ijkl} is the gradient coefficient according to the change in direction of the polarization, related to the vibrational spectrum of a crystal⁶³. Polarization gradient energy is non-zero only where the polarization is inhomogeneous: this typically occurs at interfaces, surfaces, defects, and domain walls. In a superlattice, gradient energy can be made to play a more important role by introducing spatially defined inhomogeneous distributions of polarization (superlattice layers). In general, gradient energy plays a smaller role than electrostatic boundary conditions in the evolution of polarization in most materials, but this might change in superlattices. More specifically, the depolarization field plays a large role in defining the evolution of ferroelectric polarization.

2.4. Relevant literature in ferroelectric superlattices

Pushing the limits of materials functionality can directly stem from adding more degrees of freedom in materials synthesis. Here, I examine important advances in recent years on the role of ferroelectric superlattices in discovering novel ferroelectric phases and enhancing materials properties. The key is the ability of such approaches to drive competition between the previously described relevant energy terms that can be manipulated by layering dissimilar materials (be that in lattice parameter, order parameter magnitude, dielectric constant, etc.) with unit-cell precision.

2.4.1. Improper ferroelectricity

While many ferroelectric-based heterostructures and superlattices have been studied to date, the most studied system is the $(\text{PbTiO}_3)_n/(\text{SrTiO}_3)_n$ system. Resulting polar structures vary as a function of the superlattice periodicity n . Emergent order such as improper ferroelectricity was reported in short-period superlattices ($n < 10$)⁶⁴, flux-closure domains in long-period superlattices ($n > 20$)⁶⁵, and polar vortices and skyrmions in intermediate-period superlattices ($10 < n < 20$)⁶⁶⁻⁶⁹. From first-principles calculations⁶⁴, improper ferroelectricity⁷⁰ has been reported to stem from coupling between antiferrodistortive and ferrodistortive instabilities (Figure 2.4). In these ultra-thin layers, asymmetric polar environments at the interfaces cause both instabilities, wherein the

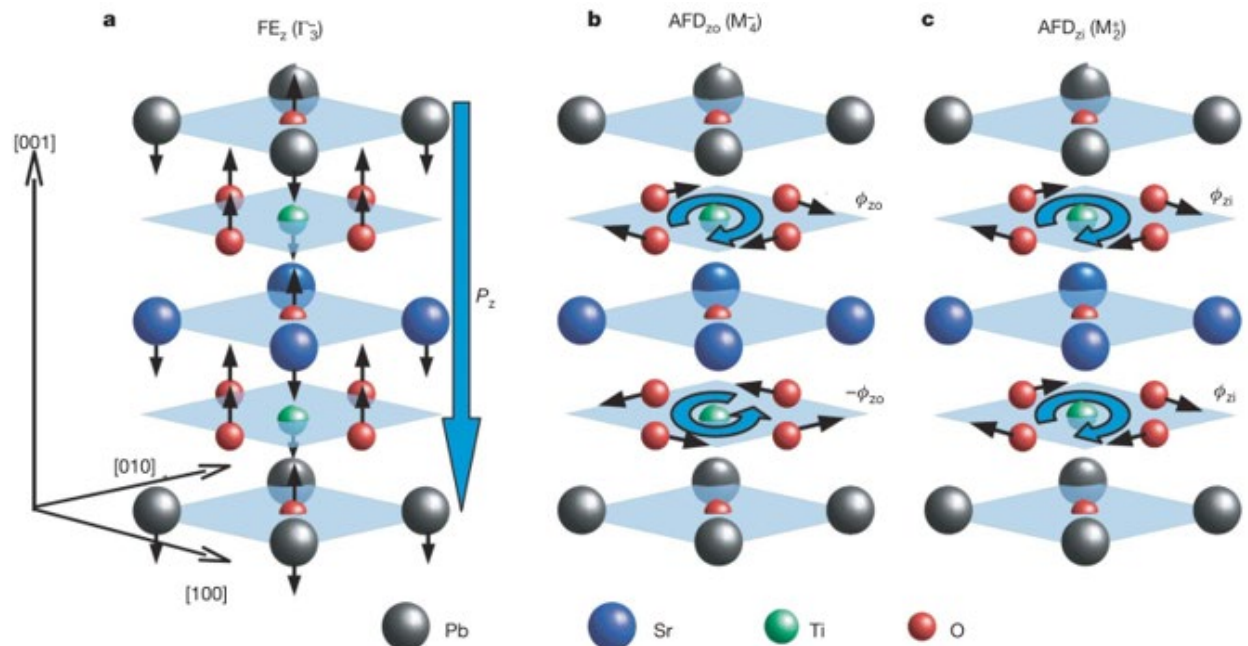


Figure 2.4. Improper ferroelectricity is observed in a short-period $(\text{PbTiO}_3)_n/(\text{SrTiO}_3)_n$ superlattice through the coupling of (a) ferrodistortive and (b,c) antiferrodistortive instabilities [adapted from Bousquet 2008]. resulting improper ferroelectricity can display interesting properties. One such property that stems from an antiferrodistortive instability is an insensitivity to depolarization fields. Thus, this type of emergent improper ferroelectricity can tackle highly relevant research endeavors regarding depolarization fields in ultra-thin films.

2.4.2. Polar vortex and skyrmion structures

Polar vortex and skyrmion structures have been reported in intermediate-period $(\text{PbTiO}_3)_n/(\text{SrTiO}_3)_n$ superlattice structures^{66–69,71,72}. These exotic polarization structures arise from the interaction of the strongly polar PbTiO_3 layer with the insulating and dielectric, but non-polar, SrTiO_3 layers that sandwich it as well as the elastic boundary conditions imposed by the substrate. The complex competition between polarization, elastic, electrostatic, and gradient energies drives the material into exotic phases with topological patterns that are highly interesting for condensed-matter physics, where analogous magnetic systems have garnered attention for possible applications in racetrack memories^{73,74}. At the atomic scale, polar skyrmions are characterized by diverging (top surface) and converging (bottom surface) Néel skyrmions (hedgehog-like) with a Bloch-wall structure at the waist. Taken together, this complex 3D structure was determined to have a skyrmion number of +1⁶⁹. 4D-STEM imaging confirmed the hedgehog-like structure, with signal and polarization maps matching simulations. These polarization topologies pose a great opportunity to study the behavior of multi-dimensional polarization structures and the potential for how applied electric fields can manipulate and control the skyrmion structure.

Initial studies are also showing that superlattices and heterostructures can exhibit novel phase transitions and enhanced susceptibilities. For example, superlattices with polar vortices and

skyrmions exhibit signatures of non-classical phase transitions that deviate strongly from Curie-Weiss-type behavior as well as dielectric permittivity that exceeds what is expected for a series capacitor or more complex equivalent-circuit models for such structures, thus leading to reports of negative capacitance⁷⁵. Increased interest on the concept of negative capacitance has also been driven by studies on multidomain ferroelectrics⁷⁶ and work on metal/Hf_{0.5}Zr_{0.5}O₂/Ta₂O₅/metal heterostructures wherein transient negative capacitance in a monodomain ferroelectric with a resistor in series has been shown⁷⁷. The design of this structure exposes the downward concavity in the center of the double-well structure of a standard ferroelectric system, which can be reconstructed from polarization hysteresis loops. Such reports pave the way for the current work to manipulate the energy landscape of ferroelectric materials thereby producing new phenomena.

Chapter 3

Synthesis and characterization of ferroelectric superlattice structures

This Chapter highlights the techniques used to synthesize and characterize ferroelectric thin-films and superlattice structures in this work. Growth methodologies are briefly introduced, with considerable attention given to pulsed-laser deposition due to its relevancy to this work. Growth mechanisms and how to monitor them *in situ* are covered as well, wherein reflection high-energy electron diffraction is highlighted in its unique utility for optimizing deposition stoichiometry through a novel technique in pulsed-laser deposition. The processes used to fabricate device structures are then highlighted. I will review methods for characterization of materials properties, namely X-ray diffraction, standard hysteresis loops, first-order reversal curves, and dielectric measurements dependent on frequencies and field strengths. Together, this Chapter gives an overview of how thin-film processing techniques are leveraged to realize and understand ferroelectric order in ultrathin-film layers.

3.1. RHEED-assisted pulsed-laser deposition

There are numerous methods to deposit thin films of materials, with many methods under the umbrella terms chemical-vapor deposition (CVD) and physical-vapor deposition (PVD). Both can achieve high-quality films and have their advantages and disadvantages. In CVD, vaporized chemical precursors react with the surface of a substrate and deposit materials in fast and uniform manner⁷⁸. This process can be sped up even further by controlling substrate temperature or plasma-assisted deposition methods, or it can be slowed down for precise layer control in processes such as atomic-layer deposition. PVD methodologies evaporate a solid-phase material onto a substrate. How the solid-phase material is evaporated varies, but this approach, in general, has the advantage of being a simpler process from an operational standpoint, offers more precise stoichiometric control of deposited compounds, and can work with lower operating temperatures⁷⁹. With advances in deposition technologies, many similar techniques have been employed in CVD and PVD to provide more accurate deposition stoichiometry, faster growth rates, and uniformity of films. Pulsed-laser deposition (PLD), which is a subset of PVD, is the most widely used technique in the laboratory setting and is the main tool used to deposit materials in this work^{80,81}.

3.1.1. Pulsed-laser deposition

PLD is a thin-film deposition technique that uses a high-energy pulsed laser to ablate a target material, creating a plasma plume that then deposits the target material onto a heated substrate. PLD can deposit materials at precise stoichiometries^{82–86} away from equilibrium, providing a major advantage for exploring a wide range of deposition materials (Figure 3.1). There is a

perception (which is ultimately unfounded), however, that PLD has historically produced lower-quality films compared to techniques such as molecular beam epitaxy (MBE)⁸⁷⁻⁸⁹. Advances in PLD have enhanced the capabilities of high-quality growth by synchronizing target motion and laser firing, multi-sample approaches, etc⁹⁰⁻⁹³, yet standard parameters are important to note.

In PLD, the primary growth parameters are temperature, pressure, laser settings, and materials selection.

Within temperature, the substrate temperature, post-deposition anneal, and ramp rates all affect the growth of a thin film. The main variable here is the substrate temperature during deposition, wherein the substrate is heated to provide enough energy to ensure high-quality epitaxy. The rate at which the substrate is heated depends on the limitations and infrastructure of the deposition system, such as resistive versus laser heaters. The rate at which a sample is cooled down after deposition is particularly important, given that two materials with different thermal expansion coefficients are in close contact with one another. Typical growth temperatures are 600-800 °C, with ramp rates in the range of 10-20 °C min⁻¹ rising and 1-10 °C min⁻¹ falling.

Within pressure, the base chamber pressure, purity of the gas cylinder, partial pressure (in this case oxygen), and dimensions of the chamber affect the pressure of a PLD process. Transferring a set of growth parameters from one system to another includes careful consideration to where in the chamber the pressure is measured, where gas is flowed in/out of the chamber, where the substrate is located, and the overall base pressure of the system. A system with a low base pressure will typically achieve cleaner, more consistent depositions⁹⁴ due to a larger ratio of partial pressure of oxygen versus background. Typical base pressures are 10⁻⁹-10⁻⁵ Torr, with growth pressures in the range of 0.1-200 mTorr. The pressure at growth affects the laser-material interaction, which is the flash evaporation, ablation, excitation, formation of plasma, and exfoliation that occurs when the laser radiation is absorbed by a target⁹⁵.

Laser settings are key to high-quality epitaxy via PLD⁹⁶⁻⁹⁸. Laser repetition rate, focus, beam spot size, energy density (fluence), and target-to-substrate distance account for the laser settings in a PLD process. The repetition rate affects how often the target is pulsed by the laser, with higher rates affecting the amount of time that deposited atoms have to find a low energy configuration on the substrate before a new wave of atoms are deposited. The focus of the beam affects the spot size, which in combination with the energy of the laser, combines to a fluence in the range of 1-3 J cm⁻² for a typical deposition. In summation, laser settings combine to ensure proper plume dynamics coming off the target and onto the substrate. While the plume does indeed occur in a (partial) vacuum, the pressure and composition of gaseous particles in the vacuum matter are important for the shape and therefore the delivery of the target species onto the substrate.

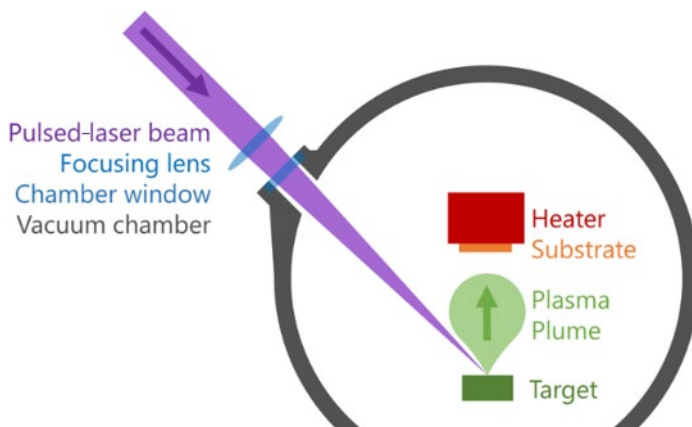


Figure 3.1. Schematic depicts pulsed-laser deposition in a vacuum chamber.

The substrate and target are incredibly important for high-quality epitaxy. In heteroepitaxy, lattice mismatch between the substrate and deposited material is perhaps the most important parameter in a deposition. Beyond mismatch, the volatility of target species is a relevant consideration to make, especially with the example of lead-based deposition. Lead is easily lost during deposition due to its volatility, which is typically compensated for by adding extra lead into the target composition compared to the intended stoichiometry, normally on the order of 10-20% excess. The distance between the target and substrate also matters, along with the location of the substrate with respect to the plume⁹⁹. Standard target-to-substrate distance is about 5 cm.

It is important to note that PLD occurs quite far from equilibrium, wherein the kinetics play a large role. The large kinetic energy in PLD is a benefit, wherein the vapor can be tuned to provide a stoichiometric transfer to the substrate. Growth kinetics are complex, but generally dominated by the diffusivity of adatoms (D)

$$D = \frac{d_{nn}^2 v_0}{4} e^{-E_a/k_B T} \quad (3.1)$$

on the surface of the substrate, with an assumption of four nearest neighbors and a distance d_{nn} to each. The activation energy E_a of each jump to a nearest neighbor typically occurs at a frequency v_0 in the range of 10^{13} Hz¹⁰⁰. With the assumption that adatoms travel an average distance λ from first reaching substrate to settling into a lattice site.

$$\lambda \approx \left(\frac{D}{F_{dep}}\right)^{1/6} \quad (3.2)$$

with a substrate miscut angle leading to a given terrace width d on the surface, the relationship between λ and d is important for growth kinetics. In this relationship, the deposition flux F_{dep} directly relates to laser settings such as repetition rate and fluence. If $\lambda > d$, step-flow growth can occur and is commonplace in growth of ruthenates such as SrRuO₃ and Ba_{0.5}Sr_{0.5}RuO₃¹⁰¹. If $\lambda < d$, layer-by-layer growth can occur as is standard in homoepitaxy, namely in SrTiO₃. Growth modes can occur depending on many factors and even change from one to another in a single growth. Beyond kinetic considerations, there are three standard growth mechanisms.

3.1.2. Growth mechanisms

There are three standard thin-film growth modes: island growth (Volmer-Weber), layer-by-layer (Frank-van der Merwe), and layer-plus-island (Stranski-Krastanov). Island growth is when deposited species cluster together and grow out-of-plane from the substrate, due to effects such as a large difference in bond strength between the deposited atoms versus the deposited atoms and the substrate (Figure 3.2a). For this reason, heteroepitaxy can lead to island growth because there is an inherent difference between the deposited species and the substrate. Layer-by-layer growth is achieved in the opposite circumstances, when deposited species do not cluster together and instead cover an entire unit-cell-thick layer on the substrate before adding on to the next layer (Figure 3.2b). This growth mode is ideal in most scenarios, including high-quality superlattice structures such as the focus of this work. Layer-plus-island growth is a deposition mode where layer-by-layer occurs for at least one layer (usually a handful of layers) and then islands start to form. This growth mode is a cross-over point in the energetics of the other two growth modes, and

is common in deposition optimization¹⁰². Simple thermodynamic models can describe the balance of growth modes in terms of interfacial energy and contact angle.

$$\cos(\theta) = \frac{\gamma_{sv} - \gamma_{fs}}{\gamma_{fv}} \quad (3.3)$$

Young's equation describes the energetics of deposition modes by relating the contact angle θ to adhesive interfacial energies (γ) between the substrate, vapor, and film, (s, v, f). Together, this relation yields regions for each growth mode, wherein the contact angle θ should be zero for an atomically smooth surface as in the layer-by-layer growth mode. If the contact angle $\theta < 0$, island

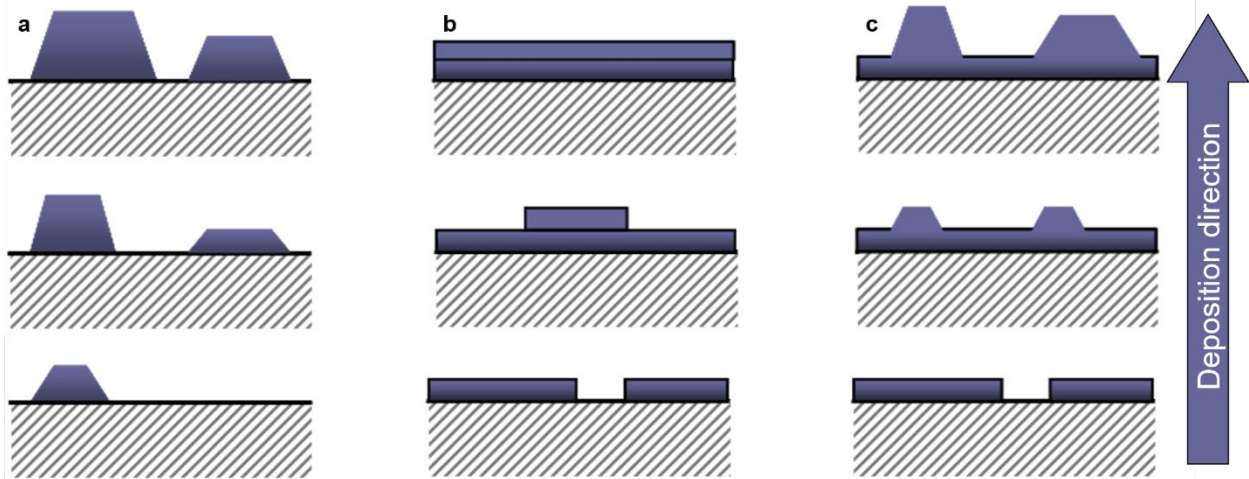


Figure 3.2. Schematic of (a) island (b) layer-by-layer and (c) layer-plus-island thin film growth modes. growth occurs. The contact angle is not stagnant for a given material deposition: it can change over time, giving rise to layer-plus-island growth. The contact angle also depends on the aforementioned growth parameters that also affect overall smoothness, coherency to the substrate, and stoichiometry of deposited materials.

The thin-film growth community has focused on the layer-by-layer growth mode with technological advances meant to improve growth mode control, with the overall goal to deposit more materials onto more substrates with smooth and coherent quality. Advances have led to unit-cell precise deposition controls, which has in turn opened opportunities for new design parameters that ultimately lead to novel phases and properties in thin-film materials. One of the critical advances for monitoring growth mode *in situ* has been reflection high-energy electron diffraction (RHEED)^{103–105}.

3.1.3. Reflection high-energy electron diffraction

RHEED is a tool used for monitoring the surface of a thin film during the deposition process. An electron beam installed in a PLD vacuum chamber is made incident with the substrate surface at a grazing angle of about 1° - 3° and is typically operated at about 10-30 keV. The incident beam both reflects and diffracts off the surface of the sample and creates a specular spot and a diffraction pattern, wherein the intensity of the specular spot is monitored as a function of time. As a full layer is deposited in the layer-by-layer growth mode, the intensity of the spot increases¹⁰⁶. After a full layer is deposited and a new layer starts to form, the intensity drops. This is due to the areal step

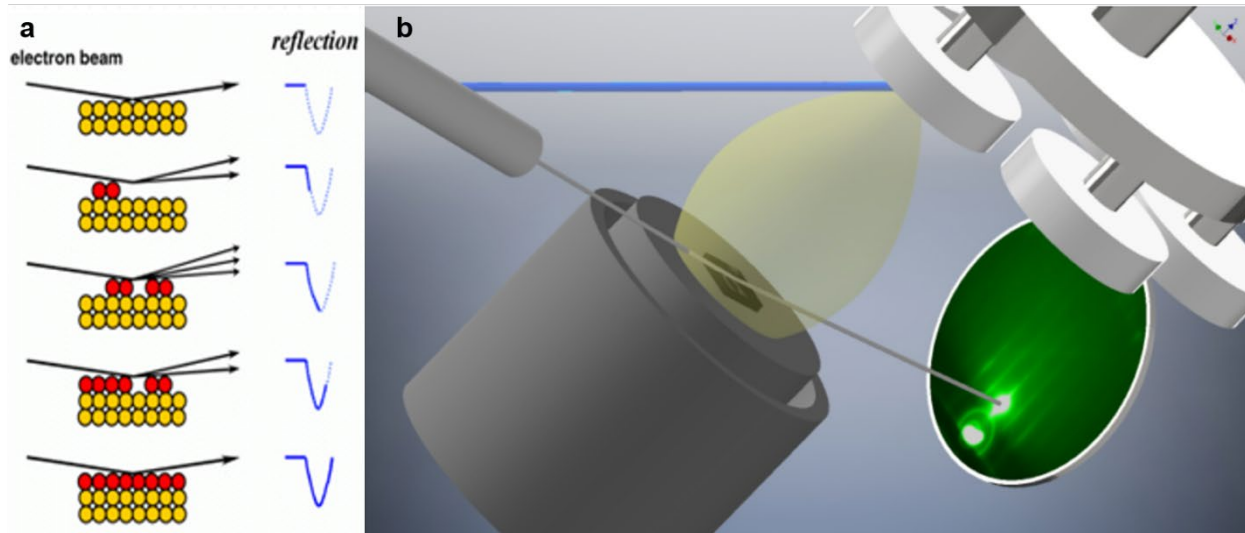


Figure 3.3. Reflection high-energy electron diffraction monitors thin film deposition in situ.

density of the surface, wherein a smooth surface results in a high RHEED intensity¹⁰⁷. In the layer-by-layer growth mode, this is seen as an oscillating pattern of intensity versus time (Figure 3.3a). Recent advances in RHEED have pushed the boundary to enable high-pressure growths^{108,109}, sequential binary oxide growth, and of course high quality layer-by-layer deposition^{103–105}.

The incident beam is at such a small angle that only the layers closest to the surface contribute to the diffracted RHEED pattern on the phosphor screen opposite to the electron beam. Because of the diffraction pattern stems from only the first few layers on the surface, the reciprocal space pattern observed is not a set of points in 3D, but instead reciprocal lattice rods extending from the sample surface. These lattice rods are the result of the intersection of the reciprocal surface with Ewald's sphere. The main diffraction beam analyzed in RHEED is the zeroth (specular) Laue circle, which aligns with the elongated reciprocal lattice rods and is denoted by (00) given that the third dimension is reduced in the interaction volume¹¹⁰. Standard RHEED techniques observe the specular spot as it has the highest intensity, yet some studies have analyzed higher-order spots for their utility in growth optimization.

RHEED is particularly useful in denoting the growth mode of film depositions. In the ideal layer-by-layer scenario, it will demonstrate a streaky pattern with oscillating intensity. However, in the island-growth scenario, the diffraction peaks (including the specular spot) will shift and look like an array of spots with no streaks. The intensity of the original specular spot from the substrate on the phosphor screen will decrease due to the shifting spot as the island film is grown. In the layer-plus-island growth mode, both scenarios are played out, with the transition denoted by both the drop in intensity and the change in pattern. Real materials can display more complex growth modes, such as layer-by-layer to step-flow growth in SrRuO₃ films. In this material, standard growth includes 1-5 unit cells of layer-by-layer growth, followed by step-flow growth.

3.1.4. RHEED for film optimization: the SrTiO₃ prototype

RHEED can be used as a tool for rapid optimization of deposition conditions. Although this work focuses on its application in PLD, it has been extensively used in MBE as well. Recent work using RHEED-assisted MBE¹¹¹ has shown a pathway for optimizing deposition conditions of SrTiO₃ (STO) in a single growth (Figure 3.4a). The benefits include time and resources spent in the optimization of high-quality crystal structure, exact stoichiometry, and smooth surfaces of deposited materials. These are necessary elements for studying materials properties in thin films, and STO is a common material in this space. The termination of STO (001) is important to consider when depositing ultra-thin films, where the interface is significant. For the case of homoepitaxial growth, the phase of the RHEED pattern has been shown to shift depending on the surface termination of the STO from substrate acid treatment and anneal before growth^{110,112}. TiO₂-terminated STO and SrO-terminated STO have different RHEED intensities, thus an oscillation is seen between each of these as STO is grown. In addition to the termination, the stoichiometry of the surface layer of the material determines the smoothness and therefore the RHEED intensity at any given point during homoepitaxial STO growth¹¹³. Because RHEED probes the near-surface layers of a sample, the intensity rises with strontium-rich STO and falls with strontium-poor STO (Figure 3.4b). As such, I utilized fluence as the primary parameter to tune the stoichiometry of deposited material onto the substrate (Figure 3.4c). The fluence was changed in this scenario by adjusting the voltage applied to the laser and thus the energy of each pulse. The optics were kept the same to provide the same spot size. The voltages were noted during deposition and used to measure corresponding energy monitor readouts immediately after deposition. The red line follows the 00 specular spot (upper middle spot) and the black line follows the 10 spot (upper right spot). The initial flat line on the far left is just the substrate, which is STO which should be spot-on stoichiometric. Starting a fluence of 0.85 J cm⁻², the growth seems to be stable and rising. This is

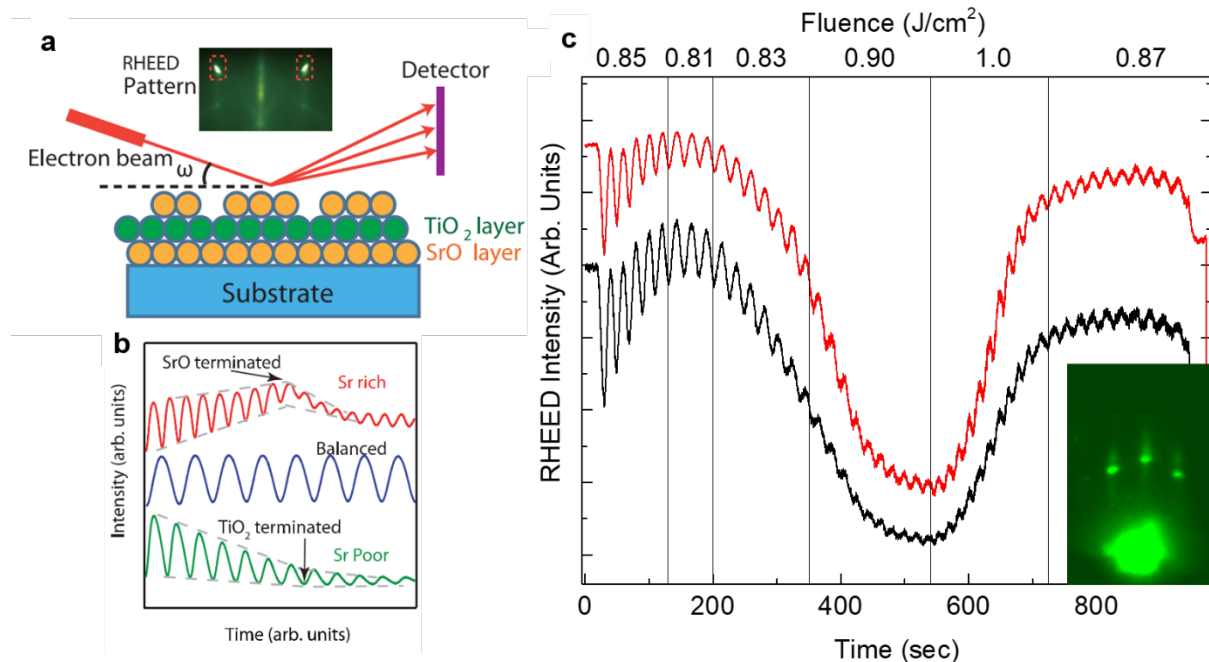


Figure 3.4. (a,b) RHEED-assisted stoichiometry optimization of SrTiO₃ deposition in molecular beam epitaxy (adapted from [2017 Zhang]). (c) Stoichiometry optimization in pulsed-laser deposition using laser fluence.

indicative of close to stoichiometric deposition. Turning down the fluence to 0.81 J cm^{-2} at 160 seconds in, the rise stops and start to falter. The bump to 0.83 J cm^{-2} sees a continuous decrease in RHEED intensity, marking a strontium-poor growth regime. Turning the fluence up to 0.9 J cm^{-2} and even up to 1.0 J cm^{-2} brings the intensity back up, with a delayed effect on the sample. Once back at the original intensity, a fluence of 0.87 J cm^{-2} demonstrates stable intensity oscillations once again, confirming near-stoichiometric growth in the range of $0.85\text{-}0.87 \text{ J cm}^{-2}$ for this particular growth. This short study demonstrates the versatility that RHEED provides in PLD, wherein stoichiometric growth is achieved in a timely and effective manner. Once structures are grown by PLD, devices are fabrication using a series of processing steps including photolithography, sputtering, wire-bonding, etc.

3.2. Fabrication of device structures

Electrical measurements were performed on parallel-plate capacitor structures achieved by deposition of a vertical stack of bottom electrode – ferroelectric – top electrode, wherein the bottom and top electrodes were grown *in situ*, immediately before and after the ferroelectric layer, respectively. SrRuO_3 and $\text{Ba}_{0.5}\text{Sr}_{0.5}\text{RuO}_3$ were primarily utilized as electrode materials due to their structural and chemical compatibility with standard ferroelectric materials analyzed in this work such as BaTiO_3 and $\text{PbZr}_{1-x}\text{Ti}_x\text{O}_3$. The compatibility and symmetric usage of these electrodes have been shown to alleviate issues such as dead layers, delamination from surfaces, high and/or asymmetric leakage, low thermal stability, and electrode-induced fatigue^{17,114–117}. This all-oxide heterostructure allows for epitaxial growth of every layer *in situ*, which also gives the benefit of RHEED monitoring throughout.

After deposition, two types of device structures were fabricated. The first structure type consists of patterning the top electrode into an array of circular structures directly (Figure 3.5a). Photolithography was used to achieve this pattern, by first spin-coating a blanket layer of photoresist on top of the sample. Samples were then placed under a mask with a desired pattern (circles 10-

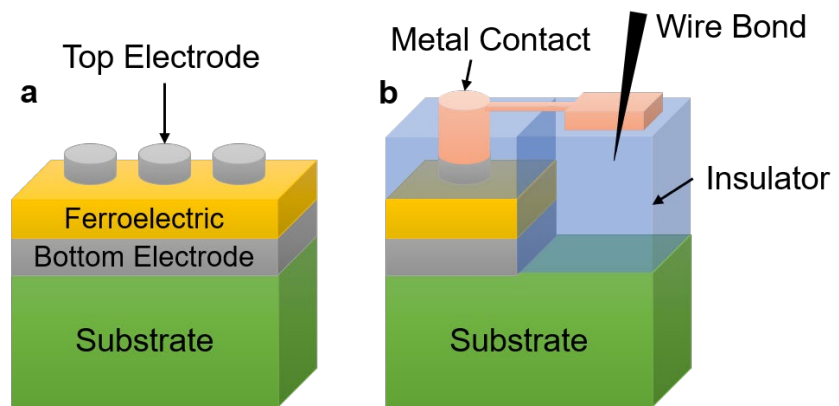


Figure 3.5. Schematic depiction of parallel-plate capacitor structures used to measure (a) standard electrical measurements and (b) temperature-dependent measurements.

100 μm in diameter) and exposed to ultraviolet radiation. An aqueous developer solution removed photoresist inverse to the circular patterns, leaving photoresist in circular arrays above the top electrode. At this stage, the top electrode that was not covered by photoresist was removed by either ion-milling or chemically etching SrRuO_3 . Lastly, the remaining photoresist was washed off before the start of electrical measurements. This structure is effective for measuring a wide range of electrical properties at room temperature. In temperature sweeps done in this study, however,

the stability of the electrical connection between a probe tip (tip diameter 5-25 μm) and the electrode (usually 15-50 μm in diameter) faltered between measurements and resulted in inconsistent and noisy results.

The second device structure used in this work mitigates the issues encountered in temperature sweeps by contacting the top electrode with a Pt metal contact, which was then connected to a pad for wire-bonding (Figure 5.3b). To fabricate this structure, four over-arching processing steps were employed. First, large trenches were ion milled into the substrate to provide space to wire-bond. Then, top electrodes were patterned into circular structures similar to the first device design. Third, an MgO insulating layer was deposited by a room-temperature PLD process. Lastly, Pt metal contacts were sputtered to provide consistent contact to each of the top electrodes. Each of these four steps had some combination of spin-coating, exposure, developer, and washing procedures with visual and electrical checkpoints throughout. From these device fabrication processes, electrical properties of superlattice heterostructures were able to be thoroughly investigated.

3.3. Structural characterization of ferroelectric superlattice structures

Structural characterization was performed using X-ray diffraction. This technique is an efficient and powerful method to non-destructively probe the structure of a high-quality material. A Panalytical X'Pert³ MRD 4-circle diffractometer with Cu K_{α} radiation at a wavelength of 1.54 \AA was used to carry out these studies. More delicate features in thin-film structures can be analyzed using an X-ray beam with higher flux generated in a synchrotron, but the features of focus for this work relied on a laboratory-based system.

X-ray diffraction is based on the elastic scattering of incident monochromatic X-ray photons by the electrons in a periodic lattice. The scattered photons form interference patterns, with constructive interference in accordance with Bragg's law¹¹⁸:

$$2d \sin \theta = n\lambda \quad (3.4)$$

where λ is the X-ray wavelength, n is the order of reflection, and d is the spacing in the out-plane direction. The angle 2θ denotes the angle between the diffracted beam and the incident beam. When an integer value of n is met, constructive interference occurs and a large intensity can be read out by a detector¹¹⁹. ω denotes the angle between the incident beam and the sample surface. The standard diffraction measurement used in this work is an $\omega - 2\theta$ scan, wherein ω and θ are set equal in what is called a symmetric scan. X-ray diffraction studies were performed before the fabricating device structures described in Section 3.2, wherein the smooth surface of the sample allows for a cleaner surface to scatter incident X-rays from. This is especially important for superlattice heterostructures, wherein fringes from the thickness of the film and the superlattice unit provide important structural information.

The thickness of thin-films can be extracted from an $\theta - 2\theta$ scan if the film is particularly pristine, wherein Laue fringes are observed^{120,121}. These fringes occur from the spacing between each layer, for example the film and the substrate, which corresponds to the thickness of the film. In superlattices specifically, satellite peaks between each of the superlattice units can also be observed, with angle differences corresponding to the thickness of each superlattice unit. These satellite peaks are observed in increasing order of magnitude, with the 0th order stemming from the average out-of-plane lattice parameter of the superlattice and negative satellites in smaller angles and positive satellites at larger angles¹²². In a $\theta - 2\theta$ scan, superlattice peaks and thickness fringes alike arise from the difference in angles according to the relation:

$$t = \frac{(n_1 - n_2)\lambda}{2(\sin \theta_1 - \sin \theta_2)} \quad (3.5)$$

wherein n_i corresponds to the order of the superlattice or thickness fringe. The difference in angle between adjacent peaks is related here to the spacing t of the total film thickness or average unit cell thickness in a superlattice. Such peaks can be seen simultaneously in one scan (Figure 3.6), where superlattice peaks up to $SL_{(+2)}$ and $SL_{(-2)}$ can be seen along with thickness fringes between $SL_{(0)}$ and $SL_{(-1)}$.

In addition to line scans, reciprocal space maps (RSMs) can provide information about the structure of thin-films such as in-plane spacing components and tilting. This is achieved by a two-axis scan along both ω and θ . This results in a 2D intensity map, with the coordinates of the map defined by two reciprocal lattice vectors Q_x and Q_y

$$Q_x = \frac{2\pi}{\lambda} [\cos(\omega) - \cos(2\theta - \omega)] \quad (3.6)$$

$$Q_y = \frac{2\pi}{\lambda} [\cos(\omega) + \cos(2\theta - \omega)] \quad (3.7)$$

for in-plane and out-of-plane crystallographic directions, respectively. Thus, for the example of an RSM taken at the 103-diffraction condition used throughout this work, the in-plane component Q_x relates to the h -direction and out-of-plane component Q_y relates to the l -direction. For analyzing the strain state of a thin-film on a substrate, this type of RSM is particularly useful. When the Q_x is maintained across substrate and film peaks, the thin is coherently strained to the substrate. A relaxed peak will be located at the bulk theoretical value for the film material, and a partially

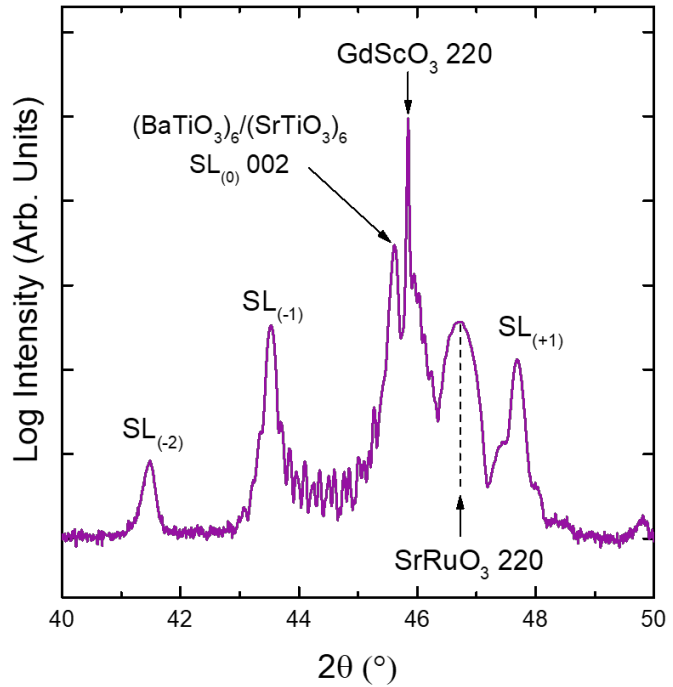


Figure 3.6. A standard symmetric θ - 2θ scan of a superlattice demonstrating both superlattice and thickness fringes related to their respective thicknesses.

relaxed film will stretch across the two. RSMs can also provide information about any periodic in-plane spacings that occur in superlattice systems, such as vortices in the $(\text{PbTiO}_3)_n/(\text{SrTiO}_3)_n$ system taken at $00l$ -diffraction conditions⁶⁶. These types of periodicities are explored in **Chapter 4** and **Chapter 5**.

3.4. Electrical characterization of ferroelectric superlattice structures

The electrical response of ferroelectric superlattice structures is vital to advances in the applicability of these materials in device applications, wherein large polarization and dielectric constants are goals to strive for in future materials. The following sections denote the manners by which hysteresis and permittivity are measured in this work.

3.4.1. Hysteretic response and beyond

Ferroelectric hysteresis loops were obtained by applying a dc field with a bipolar triangular voltage profile (Figure 3.7). In these measurements, frequencies ranging from 0.1-100 kHz were used, with a standard frequency of 10 kHz for most measurements. A Precision Multiferroic Tester (Radiant Technologies, Inc.) applied the voltage profile and measured the change in charge in the capacitor structure, which then was equated to a current and a polarization. From this measurement, polarization-electric field hysteresis loops were constructed, with coercive field E_C denoting the field strength required to switch the ferroelectric. At high fields, the polarization saturates to P_{sat} and at zero field, the polarization that remains is denoted by the remnant polarization P_r .

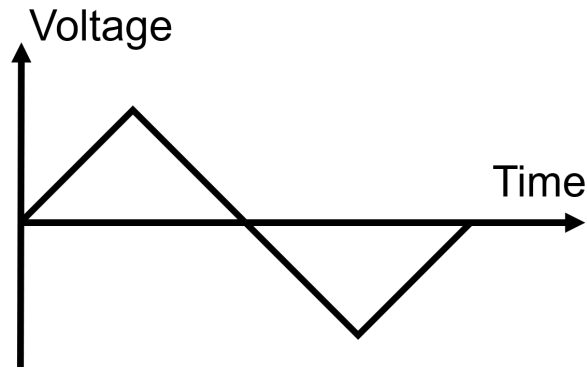


Figure 3.7. Voltage profile used to measure ferroelectric hysteresis.

This work focuses on the response of ferroelectric superlattices when a series of minor hysteresis loops are taken with increasing reversal fields. These measurements, called first-order reversal curves (FORC), were employed to provide additional insight to microscopic characteristic switching mechanisms in these systems¹²³⁻¹²⁵. FORC diagrams show a distribution of hysterons, which are switchable units in a system, as they switch with applied field. This is achieved by employing a monopolar triangular voltage profile starting at a field strong enough to saturate the material in one direction and sweeping in the opposite direction with an increasing reversal field, E_r . In this work, the saturation field was applied as a strong negative field and the reversal field denoted by each of the thin black lines returning to the bottom-left starting point (Figure 3.8). A FORC diagram presents a contour plot of hysterons switching:

$$\rho(E_r, E) = \frac{1}{2} \frac{\delta^2(P_{FORC}(E_r, E))}{\delta E_r \delta E} \quad (3.8)$$

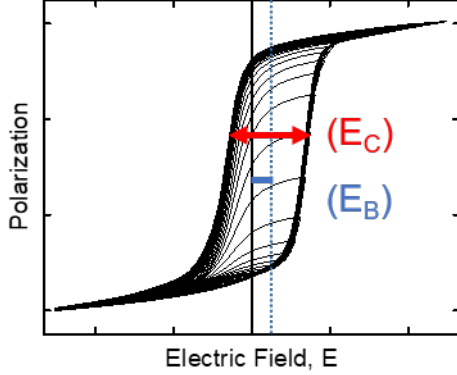


Figure 3.8. A series of minor hysteresis loops at increasing reversal fields (E_r), with coercive field (E_c) and bias field (E_B) highlighted.

wherein the coercive field E_C denotes the same as it does in a normal hysteresis loop, and the bias field E_B denotes the shift in field from symmetric about $E = 0$. When plotting the distribution of hysterons in a FORC diagram, the axes are converted from E and E_r to E_C and E_B , with important distinctions coming out of this switch. FORC distributions along the bias axis correspond to reversible polarization contributions and along the coercive axis correspond to irreversible contributions¹²⁵. FORC diagrams are used in this work to analyze how each layer of a superlattice unit biases the other. Additionally, this analysis uses the relationship between hysterons in the Preisach model¹²⁶ and their volumetric interpretation to the contribution of interfacial regions in ferroelectric switching events.

3.4.2. Dielectric response

Dielectric measurements were carried out as a function of frequency, ac field strength, dc field strength, and temperature. These measurements reveal important behavior of oxide thin films, which are primarily of interest for their large dielectric constants. In measuring the dielectric susceptibility, a small ac voltage was applied in an out-of-plane capacitor structure outlined in Section 3.2. The dielectric capacitance was measured as the proportion of 90° lagging signal, defined as:

$$V_{(t)} = RI_m \sin(\omega t - \theta_z) \quad (3.9)$$

the readout voltage lagging the applied current. This phase angle θ_z is -90° in the case of purely capacitive response and 0° in the purely resistive scenario when the applied signal is in-phase with the readout. In analyzing dielectric, the loss associated with deviation from a purely capacitive response is related to the loss tangent, which relates the real ϵ'_r and imaginary ϵ''_r components of permittivity together, wherein:

$$\tan \delta = \frac{\epsilon''_r}{\epsilon'_r} \quad (3.10)$$

the loss tangent $\tan(\delta)$ indicates an ideal capacitor when it is equal to 0. In experiment, capacitance measured from the impedance analyzer (E4990A, Keysight Technologies) was converted into permittivity using the parallel plate capacitor relation, given by:

$$\epsilon'_r = \frac{Cd}{\epsilon_0 A} \quad (3.11)$$

where C is the capacitance measured, A is the area of the top electrode circular capacitor, ϵ_0 is the permittivity of free space, and d is the thickness of the film. In the following sections, more detail will be provided about how ferroelectric materials behave under varying ac field strength, temperature, and frequency.

3.4.3. Rayleigh studies of ferroelectric materials

Rayleigh dielectric measurements analyze the evolving contributions to dielectric response in ferroelectric materials. These measurements are achieved by sweeping the field strength of an ac excitation, wherein three regions can be observed. The first region is called the low field region, wherein the applied field results in reversible motion of domain walls and other extrinsic effects (Figure 3.9). Increasing the field will eventually enter the Rayleigh region, wherein irreversible motion of domain walls and extrinsic effects contribute to a larger overall dielectric response, observed as both an increase in the loss tangent and the real permittivity. Further increasing the field will eventually surpass the coercive field E_C , wherein the sample begins the ferroelectric switching process¹²⁷. This region, called the high field region, typically is denoted by a sharp uptick in the permittivity consistent with the expectation of an increased switching current. The low field and Rayleigh region are sub-switching, wherein no switching is observed. The low field regime is denoted by the flat, field-independent starting value of the permittivity. The Rayleigh regime sees a linear increase in permittivity proportional to the Rayleigh coefficient^{127,128} α . Thus, the sub-switching Rayleigh behavior is defined by the empirical Rayleigh law¹²⁹:

$$\epsilon'_r(E_0) = \epsilon'_r(0) + \alpha E_0 \quad (3.12)$$

where E_0 denotes the ac field strength. Standard permittivity measurements are taken at a low field such as 5-30 mV for a 100 nm film of a standard ferroelectric material, wherein no switching will occur.

At higher fields, switching current demonstrates a rapid rise in the permittivity, followed by a tapering off at extremely high voltages. This can be correlated to the slope of a hysteresis loop, wherein the switching current is large near the coercive field. Beyond that, the ferroelectric saturates and the permittivity decreases. In a relaxor, the hysteresis loop looks like a ferroelectric except the sub-switching region is gone – thus the remnant polarization is zero. Rayleigh dielectric measurements of relaxor materials display just the switching regime, wherein permittivity either rises or falls with increasing field strength according to the proximity to the freezing temperature of the relaxor.

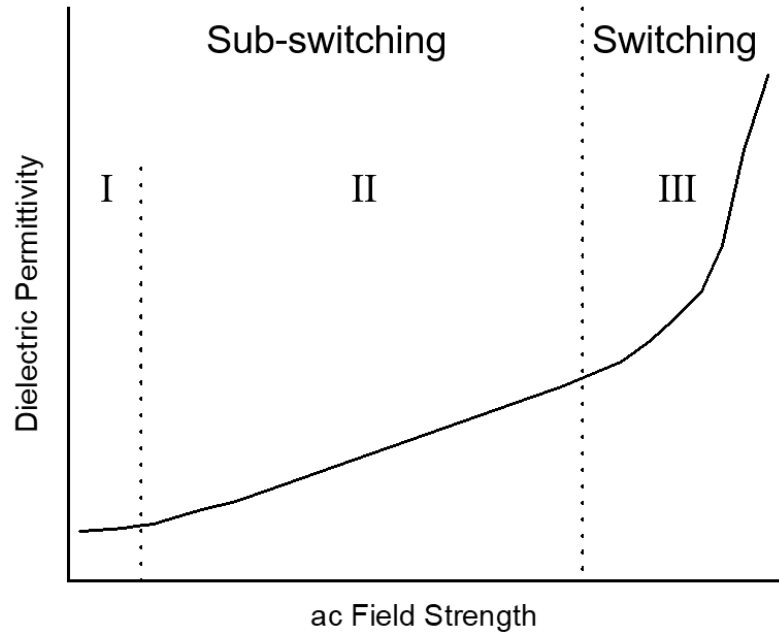


Figure 3.9. Rayleigh behavior in ferroelectric materials is illustrated in three distinct regions (adapted from [1999 Stevenson]).

3.4.4. Relaxor ferroelectrics: Vogel-Fulcher analysis

Relaxor ferroelectric materials can be analyzed by their transition temperatures, wherein temperature-dependent frequency sweeps can confirm two of the main relaxor characteristics; broad maximum of temperature-dependent dielectric maximum and frequency dispersion of this maximum, T_{max} . This is a deviation from Curie-Weiss behavior in standard ferroelectric materials¹³⁰. The Vogel-Fulcher relation describes the freezing out of PNRs in relaxor materials:

$$f = f_0 \exp \left[-\frac{E_a}{k(T_{max} - T_F)} \right] \quad (3.13)$$

where T_F is the static freezing temperature, f_0 the Debye frequency, E_a the activation energy, and T_{max} the temperature at which the permittivity is at its maximum. Vogel-Fulcher analysis can be done on temperature- and frequency-dependent data, wherein data with at least three orders of magnitude in the frequency domain is recommended for fitting this equation³⁰. In this work, frequency-maximum temperature pairs are fitted to the Vogel-Fulcher relation to extract the freezing temperature, Debye frequency, and activation energy. The degree of relaxor behavior is represented by the curvature of $\ln(f)$ vs T_{max} , wherein a flat vertical line demonstrates no frequency dispersion in the dielectric maximum. The fitted parameters reveal insight to relaxor behavior such as the energy required for a thermally activated transition between polarization configurations and thermally activated polarization fluctuation frequencies. Standard values for relaxor films are 10^{11} - 10^{13} Hz and 0.005-0.05 eV for the Debye frequency and activation energy, respectively¹³¹. The freezing temperature of a relaxor is also extracted from this analysis, which represents the zero-frequency dielectric maximum and is associated with the freezing out of all PNRs. At non-zero frequencies, a distribution of PNRs begin to freeze-out at higher temperatures, giving rise to the frequency-disperse maxima in the dielectric permittivity.

Chapter 4

Enhanced dielectric and ferroelectric properties in $\text{PbZr}_{1-x}\text{Ti}_x\text{O}_3$ superlattice structures

This Chapter focuses on the enhancement of dielectric and ferroelectric properties in a classic ferroelectric system through modulation of superlattice-design parameters. Superlattice periodicity is tuned to simultaneously demonstrate large susceptibility and polarization in the $\text{PbZr}_{1-x}\text{Ti}_x\text{O}_3$ system. The ability to produce atomically precise, artificial oxide heterostructures provides for the possibility of producing exotic phases and enhanced susceptibilities not found in parent materials. Typical ferroelectric materials exhibit either large saturation polarization away from a phase boundary or large dielectric susceptibility near a phase boundary. Here, I attain *both* large ferroelectric polarization and dielectric permittivity wherein fully epitaxial $(\text{PbZr}_{0.8}\text{Ti}_{0.2}\text{O}_3)_n/(\text{PbZr}_{0.4}\text{Ti}_{0.6}\text{O}_3)_{2n}$ ($n = 2, 4, 6, 8, 16$ unit cells) superlattices are produced such that the overall film chemistry is at the morphotropic-phase boundary (MPB), but constitutive layers are not. Long- ($n \geq 6$) and short-period ($n = 2$) superlattices reveal large ferroelectric saturation polarization ($P_s = 64 \mu\text{C cm}^{-2}$) and small dielectric permittivity ($\epsilon_r \approx 400$ at 10 kHz). Intermediate-period ($n = 4$) superlattices, however, exhibit both large ferroelectric saturation polarization ($P_s = 64 \mu\text{C cm}^{-2}$) and dielectric permittivity ($\epsilon_r = 776$ at 10 kHz). First-order reversal curve analysis reveals the presence of switching distributions for each parent layer and a third, interfacial layer wherein superlattice periodicity modulates the volume fraction of each switching distribution and thus the overall material response. This reveals that deterministic creation of artificial superlattices is an effective pathway for designing materials with enhanced responses to applied bias.

4.1. Introduction

Superlattices comprised of thin layers of ferroelectric and/or dielectric materials provide ample opportunity for designing artificial heterostructures with tunable and emergent properties. For example, ferroelectrics can exhibit large susceptibilities to electric fields, stress, temperature, *etc.* which can be enhanced by the competition of structure and polarization between phases and can even lead to the development of novel order parameters^{132–134}. In this regard, ferroelectric-dielectric superlattices have been widely studied^{135,136]} with particular interest on $\text{BaTiO}_3/\text{SrTiO}_3$ ^{46,48,137–141} and $\text{PbTiO}_3/\text{SrTiO}_3$ superlattices^{64,65,142}. In $\text{PbTiO}_3/\text{SrTiO}_3$ superlattices, for example, researchers have observed the evolution of novel order (*i.e.*, improper ferroelectricity),⁶⁴ emergent, smoothly-evolving polar structures (*e.g.*, vortices and skyrmions)^{66,69}, and even classical flux-closure-domain structures depending on the periodicity and strain state⁶⁵. Considerably less work, however, has focused on superlattices of two different ferroelectric materials^{143,144} wherein differences in symmetry¹⁴⁵, polarization magnitude and direction, transition temperature¹⁴⁶, *etc.* provide for an alternative approach to novel and/or enhanced responses and phases.

4.2. Morphotropic-phase boundary

The $\text{PbZr}_{1-x}\text{Ti}_x\text{O}_3$ system provides interesting opportunities in this regard as there are both zirconium-rich rhombohedral and titanium-rich tetragonal phases that are bridged by an MPB^{147,148} wherein those phases compete and provide for interesting properties (Figure 4.1). Polarization rotation at this phase boundary enables an easier route to switching at lower coercive fields and enhances susceptibilities – including both dielectric and electromechanical.

Large susceptibilities in the $\text{PbZr}_{1-x}\text{Ti}_x\text{O}_3$ system have historically been attained by selecting materials in the compositional vicinity of the MPB^{149–151}. This typically comes as a trade-off with saturation polarization, as polarization diminishes and susceptibility rises at a phase transition. While there has been considerable research on the compositional evolution of structure and properties in this system^{152–154}, little work exists on the creation of artificial heterostructures and superlattices^{155–157}. That which does exist focuses on long-period (*i.e.*, layers of thickness ≥ 30 nm), ferroelectric-ferroelectric heterostructures. The exploration

of short-period (down to 2 unit cells) ferroelectric-ferroelectric superlattices bridged across the MPB in the $\text{PbZr}_{1-x}\text{Ti}_x\text{O}_3$ system has a potential route to enhanced functionalities. Such a systematic study of ultra-thin superlattice periodicities can elucidate the complex interplay of competing energy terms (*e.g.*, elastic, electrostatic, gradient, *etc.*) present in ferroelectric systems.

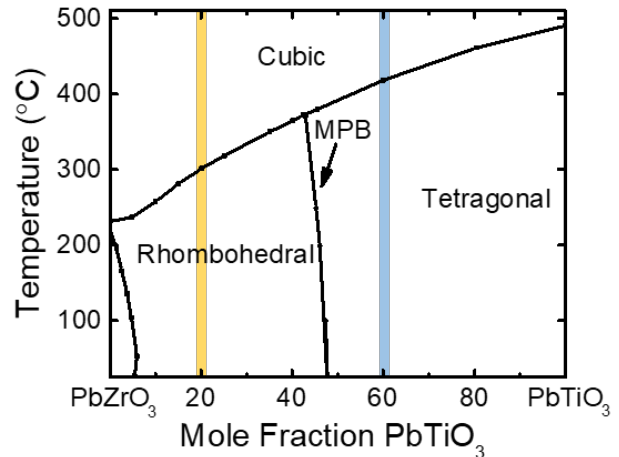


Figure 4.1. The phase diagram of the $\text{PbZr}_{1-x}\text{Ti}_x\text{O}_3$ system with vertical bars indicating selected parent compositions.

4.3. Compositional tuning

Here, I take advantage of unit-cell-precise growth (see **Chapter 3**) to introduce ferroelectric-ferroelectric interfaces as an additional design parameter wherein the material response can be tuned by both composition and superlattice periodicity. I focus on heterostructures with overall chemistry near the MPB, but built from compositions far from the phase boundary itself: rhombohedral $\text{PbZr}_{0.8}\text{Ti}_{0.2}\text{O}_3$ and tetragonal $\text{PbZr}_{0.4}\text{Ti}_{0.6}\text{O}_3$. Using reflection high-energy electron diffraction (RHEED)-assisted pulsed-laser deposition, I synthesized atomically-precise $(\text{PbZr}_{0.8}\text{Ti}_{0.2}\text{O}_3)_n/(\text{PbZr}_{0.4}\text{Ti}_{0.6}\text{O}_3)_{2n}$ ($n = 2, 4, 6, 8,$ and 16 unit cells) superlattices with overall film chemistry of $\text{PbZr}_{0.53}\text{Ti}_{0.47}\text{O}_3$. Rhombohedral $\text{PbZr}_{0.8}\text{Ti}_{0.2}\text{O}_3$ and tetragonal $\text{PbZr}_{0.4}\text{Ti}_{0.6}\text{O}_3$ were chosen for this work because they are robust ferroelectric phases that differ in terms of symmetry, polarization direction, and have relatively close lattice parameters ($a = 4.115$ Å for $\text{PbZr}_{0.8}\text{Ti}_{0.2}\text{O}_3$ and $a = 4.008$ Å, $c = 4.134$ Å for $\text{PbZr}_{0.4}\text{Ti}_{0.6}\text{O}_3$) such that high-quality superlattices of various periods can be synthesized. All heterostructures were grown on 20 nm $\text{Ba}_{0.5}\text{Sr}_{0.5}\text{RuO}_3/\text{PrScO}_3$

(110) substrates (which were chosen because of the compressive strain¹⁵⁸ that is imposed on both the $\text{PbZr}_{0.8}\text{Ti}_{0.2}\text{O}_3$ (-2.5%) and $\text{PbZr}_{0.4}\text{Ti}_{0.6}\text{O}_3$ (-0.3%) layers).

It has been observed in prior studies that the exact chemical composition of the MPB in $\text{PbZr}_{1-x}\text{Ti}_x\text{O}_3$ can shift (slightly) towards higher concentrations of zirconium with compressive epitaxial strain¹⁵⁹. Thus, a preliminary study was conducted to assess the average superlattice composition required to access phase-boundary-like behavior, namely an enhancement of dielectric susceptibility¹⁶⁰. To sweep across various average compositions, 80-nm-thick $(\text{PbZr}_{0.8}\text{Ti}_{0.2}\text{O}_3)_n/(\text{PbZr}_{0.4}\text{Ti}_{0.6}\text{O}_3)_m$ superlattices with varying $n \times m$ ratios were produced while the total periodicity $n + m$ was held constant at 12 unit cells (specifically I studied $n \times m = 7 \times 5, 5 \times 7, 4 \times 8$, and 3×9 , corresponding to average superlattice compositions of $\text{PbZr}_{0.63}\text{Ti}_{0.37}\text{O}_3$, $\text{PbZr}_{0.57}\text{Ti}_{0.43}\text{O}_3$, $\text{PbZr}_{0.53}\text{Ti}_{0.47}\text{O}_3$, and $\text{PbZr}_{0.5}\text{Ti}_{0.5}\text{O}_3$, respectively). Subsequent θ - 2θ X-ray diffraction studies reveal high-quality, epitaxial superlattices (Figure 4.2a). Capacitor-based dielectric-permittivity measurements indicate an enhancement of the out-of-plane dielectric response, akin to that expected near the phase boundary, for the 4×8 superlattices (Figure 4.2b)

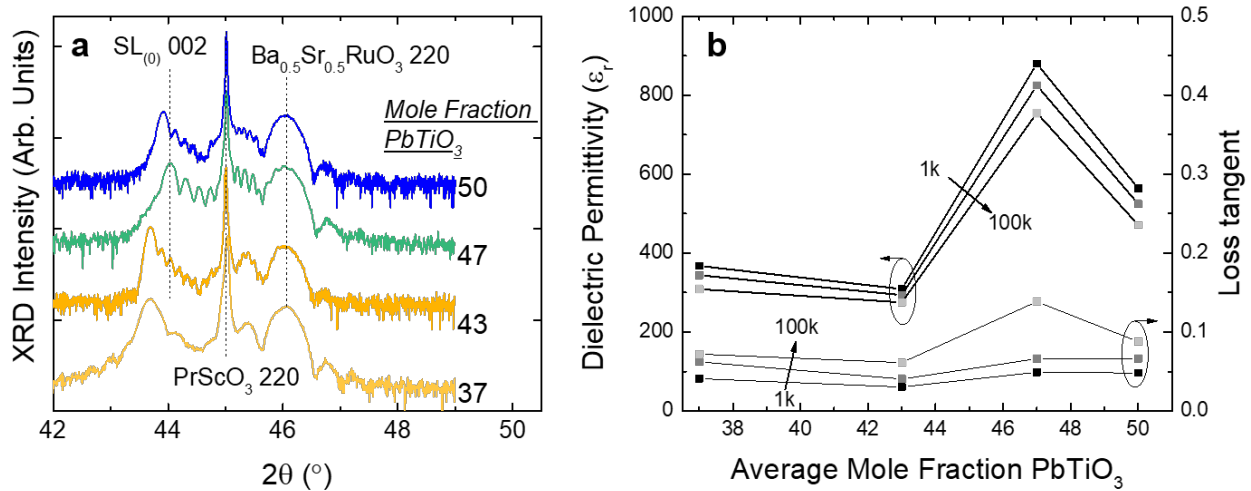


Figure 4.2. A series of $(\text{PbZr}_{0.8}\text{Ti}_{0.2}\text{O}_3)_n / (\text{PbZr}_{0.4}\text{Ti}_{0.6}\text{O}_3)_m$ superlattices with varying average composition. The ratio $n \times m$ was adjusted while $n + m = 12$ u.c. was held constant. (a) θ - 2θ X-ray scans and (b) dielectric permittivity reveals phase boundary-like behavior at an average mole fraction of PbTiO_3 of 47, as in $\text{PbZr}_{0.53}\text{Ti}_{0.47}\text{O}_3$.

which corresponds to an average composition of $\text{PbZr}_{0.53}\text{Ti}_{0.47}\text{O}_3$. Based on this observation, for the remainder of the study I fixed the overall heterostructure chemistry to be $\text{PbZr}_{0.53}\text{Ti}_{0.47}\text{O}_3$ thus requiring the production of various $n \times 2n$ superlattices.

4.4. Superlattice structures

At this overall film composition ($\text{PbZr}_{0.53}\text{Ti}_{0.47}\text{O}_3$), periodicity-dependent studies were completed. I focused on 80-nm-thick heterostructures including the following variants: 1) superlattice structures of the form $(\text{PbZr}_{0.8}\text{Ti}_{0.2}\text{O}_3)_n/(\text{PbZr}_{0.4}\text{Ti}_{0.6}\text{O}_3)_{2n}$ (with $n = 2, 4, 6, 8$, and 16), 2) bilayer structures with 27 nm of $\text{PbZr}_{0.8}\text{Ti}_{0.2}\text{O}_3$ and 53 nm of $\text{PbZr}_{0.4}\text{Ti}_{0.6}\text{O}_3$ (*i.e.*, a 1:2 ratio of the parent materials, equivalent to the ratio found in all the superlattices), 3) parent rhombohedral $\text{PbZr}_{0.8}\text{Ti}_{0.2}\text{O}_3$, 4) parent tetragonal $\text{PbZr}_{0.4}\text{Ti}_{0.6}\text{O}_3$, and 5) MPB $\text{PbZr}_{0.52}\text{Ti}_{0.48}\text{O}_3$. The production

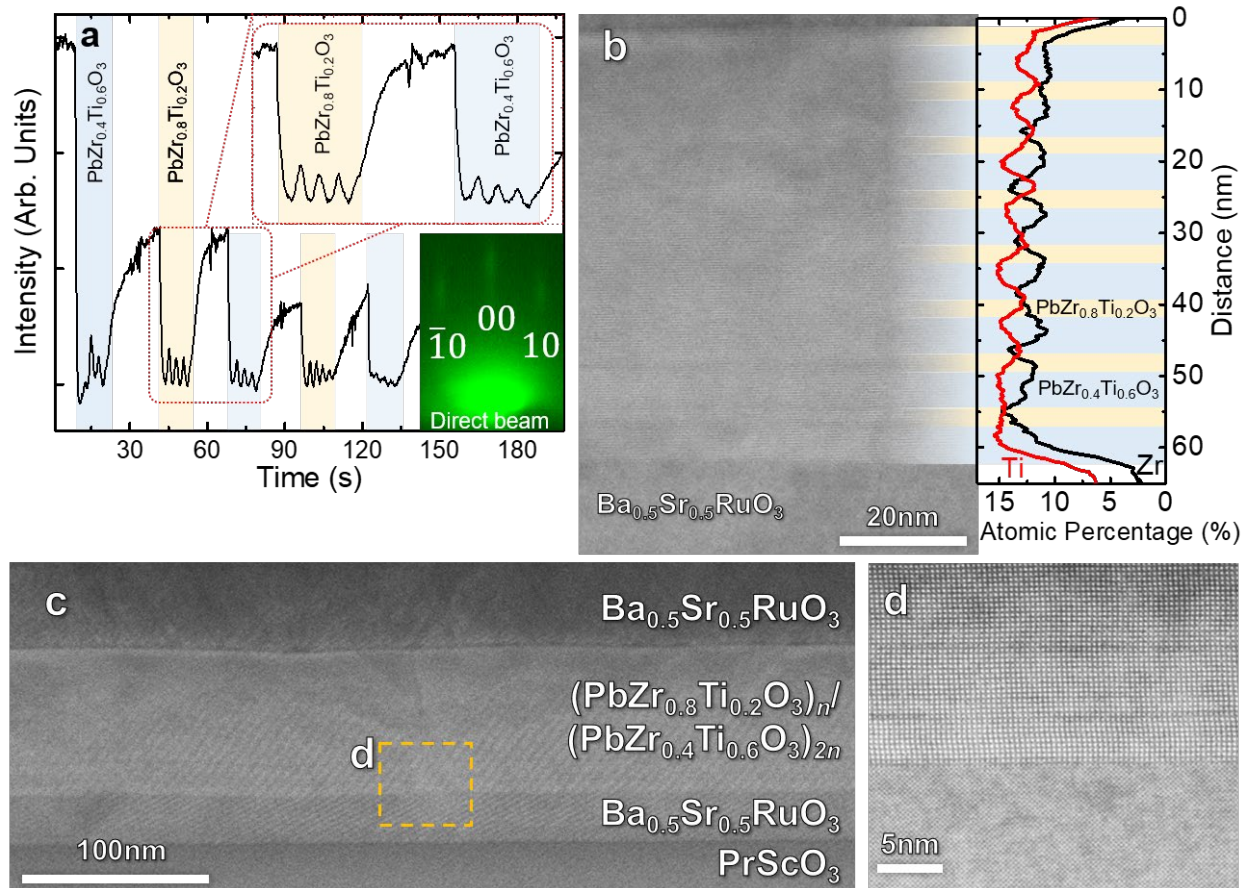


Figure 4.3. (a) RHEED-assisted PLD of heterostructures demonstrates persistent layer-by-layer deposition and sharp interface control. (b) STEM image of the superlattice structure with overlaid EDS mapping of Ti and Zr. (c) A lower-resolution image across a wide area of the heterostructure, here for an $n = 8$ superlattice, reveals (d) smooth interfaces with no apparent defect structures.

of high-quality superlattices was enabled by my ability to achieve layer-by-layer growth as monitored during deposition via RHEED (Figure 4.3a). Throughout (and after growth) the presence of a “streaky” RHEED pattern demonstrates a persistent 2D-growth mode and a smooth surface for a representative superlattice growth (inset, Figure 4.3a).

Z-contrast, high-angle annular dark-field (HAADF) scanning transmission electron microscopy (STEM) imaging and energy dispersive spectroscopy (EDS) studies were completed for two superlattice structures $[(\text{PbZr}_{0.8}\text{Ti}_{0.2}\text{O}_3)_n]/(\text{PbZr}_{0.4}\text{Ti}_{0.6}\text{O}_3)_{2n}$ with $n = 6, 8$. Due to the similar chemistry between the layers (*i.e.*, both layers in the superlattice contain lead, zirconium, and titanium) the Z-contrast between the layers is not as distinct as one might expect for a superlattice made from vastly different materials. To confirm the production of the superlattice structures, EDS studies were employed to map the local chemical variations throughout the superlattice structure (Figure 4.3b). The EDS signatures from the titanium and zirconium are observed to oscillate or alternate in intensity due to the chemical variations in each layer of the superlattice (*i.e.*, from zirconium-rich $\text{PbZr}_{0.8}\text{Ti}_{0.2}\text{O}_3$ to titanium-rich $\text{PbZr}_{0.4}\text{Ti}_{0.6}\text{O}_3$) and this helps identify the superlattice structure in the absence of robust Z-contrast. A lower-resolution image across a wide area of the heterostructure, here for a $n = 8$ superlattice, reveals smooth interfaces with no apparent defect structures (Figure 4.3c). Additional atomic-resolution imaging, here at the interface between

the bottom electrode and superlattice structure, further confirms the high-quality structures and highly commensurate nature of the interface (Figure 4.3d).

θ - 2θ X-ray diffraction studies of the resulting superlattices reveal epitaxial, $00l$ -oriented films with superlattice peaks varying as a function of superlattice periodicity (Figure 4.4a). Wide-angle θ - 2θ X-ray studies show no secondary phases and high-quality, epitaxial growth for all heterostructure variants (Figure 4.4b). Reciprocal space maps about the 103_{pc} -diffraction conditions for all superlattice heterostructures show fully strained films (Figure 4.5). All told, the STEM and EDS data, in conjunction with extensive RHEED and X-ray diffraction studies, confirm that high-quality superlattices of various periodicities can be produced. Thus, it is appropriate to

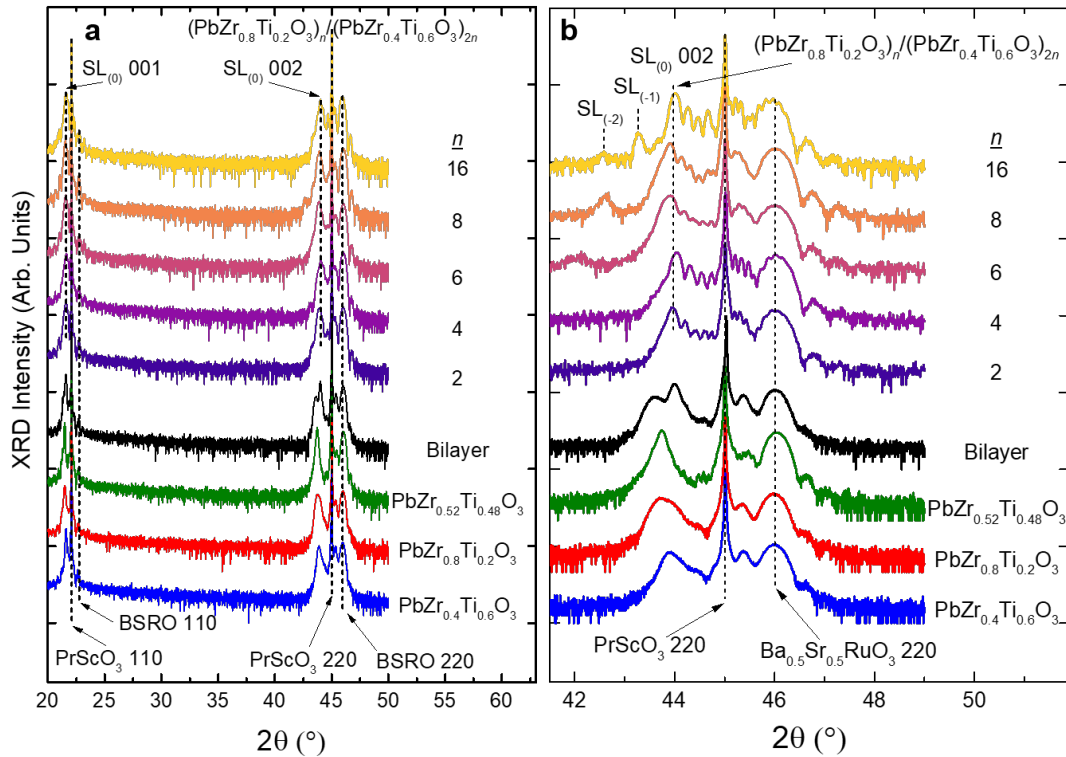


Figure 4.4. (a) Full-range θ - 2θ X-ray diffraction patterns about the 002-diffraction condition for superlattices of various periodicities and accompanying reference films demonstrate excellent epitaxial crystalline quality. (b) θ - 2θ X-ray diffraction patterns about the 002-diffraction condition demonstrate precise superlattice control.

proceed to study the impact of superlattice design on dielectric and ferroelectric response.

4.5. Periodicity-dependent dielectric enhancement

Frequency-dependent dielectric-permittivity measurements demonstrate low-loss response in all heterostructure variants, but a strong superlattice periodicity dependence of the permittivity itself (Figure 4.6a-b). Similar studies were completed for the parent tetragonal $PbZr_{0.4}Ti_{0.6}O_3$ ($\epsilon_r = 362$ at 10 kHz), the parent rhombohedral $PbZr_{0.8}Ti_{0.2}O_3$ ($\epsilon_r = 492$ at 10 kHz), and MPB $PbZr_{0.52}Ti_{0.48}O_3$ ($\epsilon_r = 799$ at 10 kHz). Both the $PbZr_{0.4}Ti_{0.6}O_3$ and $PbZr_{0.8}Ti_{0.2}O_3$ show low dielectric loss, while the $PbZr_{0.52}Ti_{0.48}O_3$ shows slightly increased loss consistent with the complex structural evolution

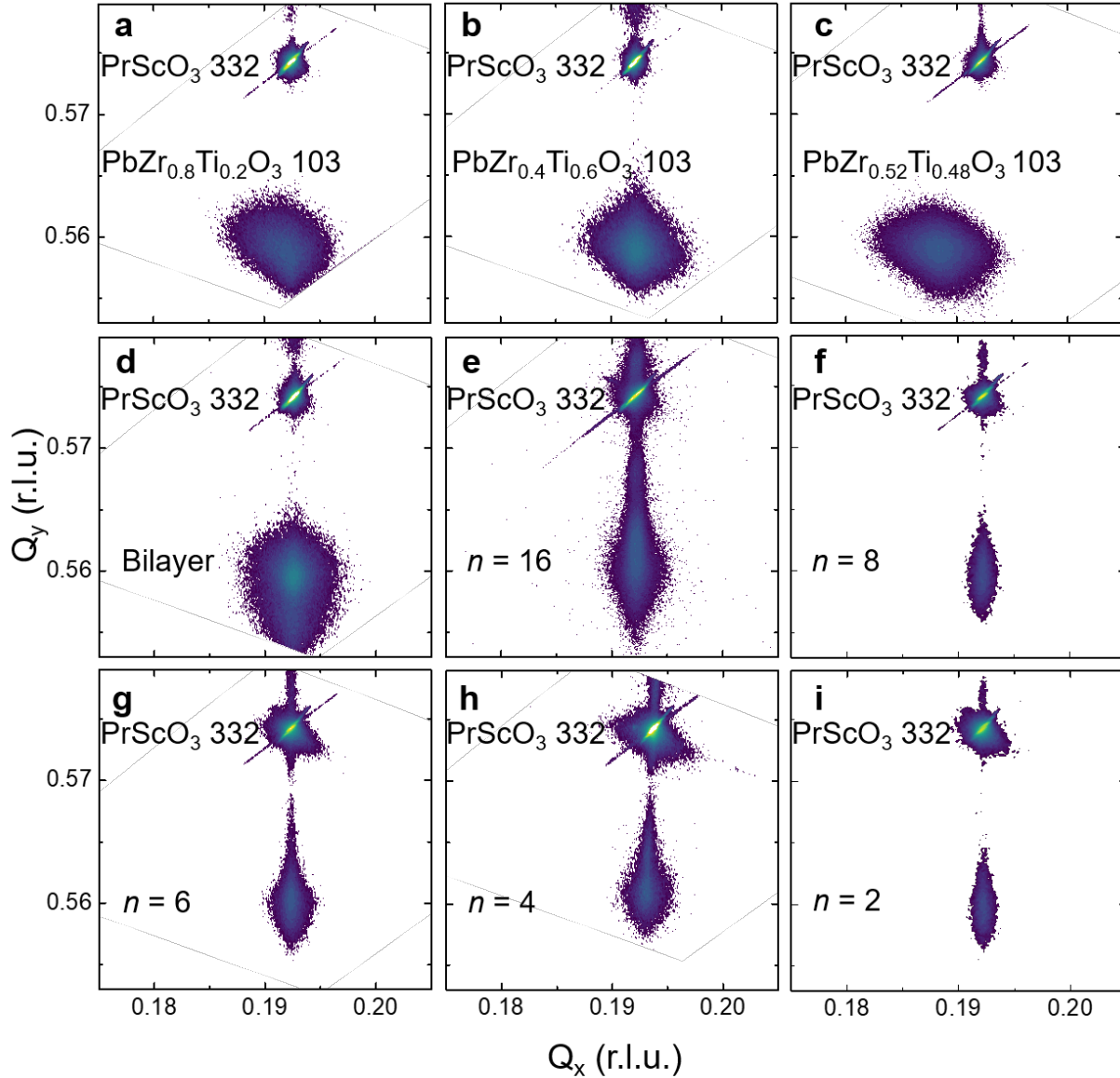


Figure 4.5. Reciprocal space maps about $(103)_{pc}$ indicate slightly larger c/a ratio for (a-c) parent phases compared to (d-h) superlattices and (i) bilayer on the same substrate, consistent with trends in ferroelectric polarization saturation.

under applied external fields. This range of properties provides an important framework in which to probe the superlattice heterostructures. The dielectric permittivity hovers around ≈ 400 (at 10 kHz) for the bilayer heterostructures and all long-period superlattices ($n \geq 6$). At the other end of the spectrum, short-period superlattices ($n = 2$) also exhibit permittivity in a similar range. Intermediate-period superlattices ($n = 4$), however, display dramatically enhanced permittivity (≈ 776 at 10 kHz, Figure 4.6c). Naively, one might expect that reducing the superlattice period should result in a more uniform, MPB-like heterostructure and, thus, systematically increasing dielectric response. These observations, however, suggest a more complex evolution of dielectric response with superlattice periodicity and beg the question: what gives rise to the dielectric enhancement in the $n = 4$ superlattices?

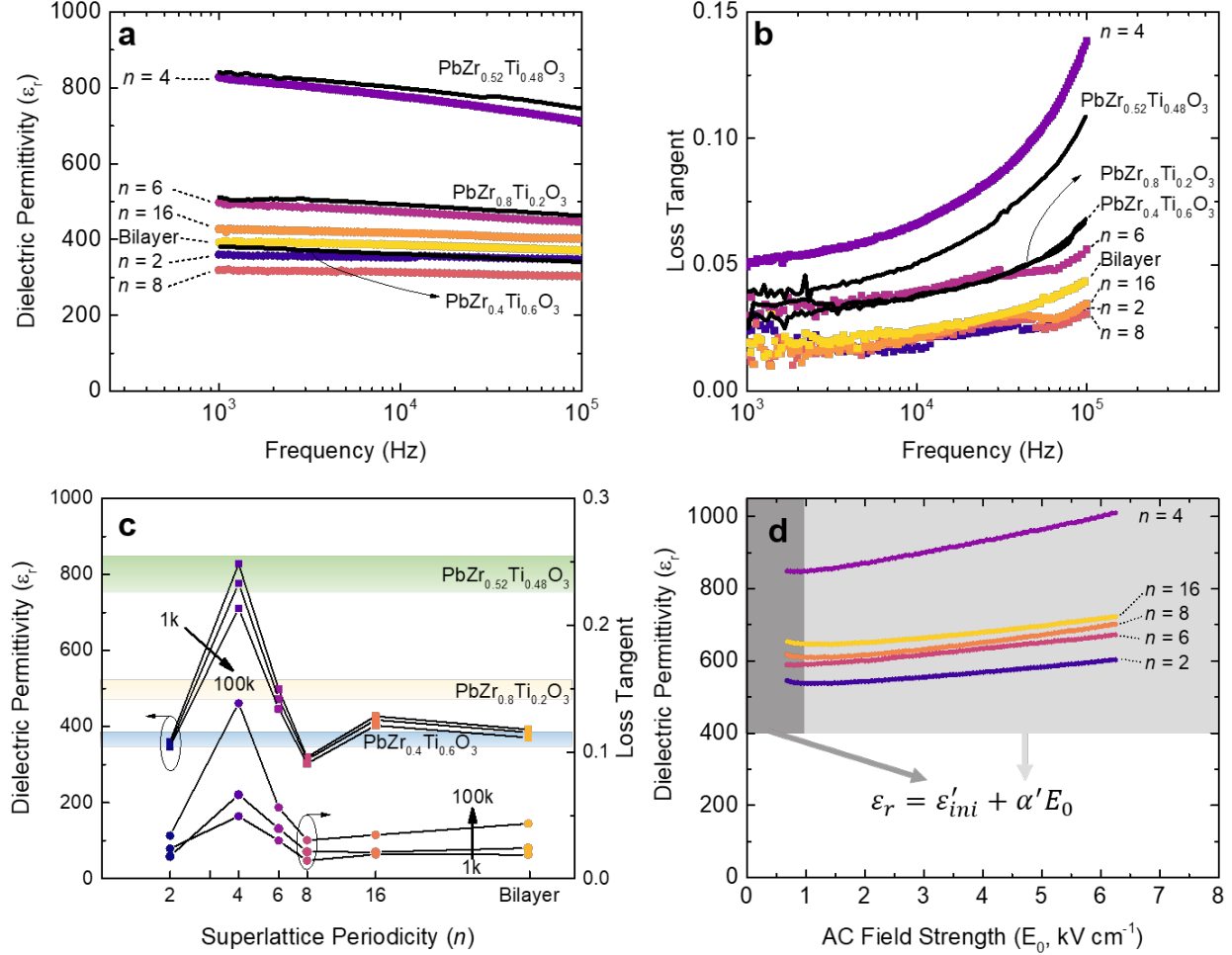


Figure 4.6. Dielectric response: (a) permittivity and (b) loss show a variety of permittivities while maintaining low-loss. (c) Summarized dielectric response demonstrates an enhancement at a critical superlattice unit $n = 4$ unit cells. (d) Rayleigh dielectric measurements at sub-switching fields.

To explore the nature of this enhancement in intermediate-period superlattices, Rayleigh dielectric measurements were employed at sub-switching fields. Rayleigh studies utilize an ac-field-dependent measurement to probe the behavior of ferroelectric materials in three different regimes: low, high, and switching fields (Figure 4.6d). Both the low- and high-field regimes are sub-switching linear regimes from which the reversible and irreversible extrinsic contributions to dielectric response, respectively, can be extracted. In the low-field regime¹²⁷, an enhanced field-independent constant permittivity represented by the reversible Rayleigh parameter ϵ'_{ini} indicates large intrinsic lattice and reversible extrinsic contributions¹⁰. In the high-field (Rayleigh regime), a steep linear slope indicated by the Rayleigh coefficient α' is typical of an enhanced irreversible contribution¹⁶¹. Thus, the overall dielectric response is represented as:

$$\epsilon_r = \epsilon'_{ini} + \alpha' E_0. \quad (4.1)$$

Analysis of the Rayleigh studies at sub-switching fields reveals both parent phases and the bilayer heterostructures to have small ϵ'_{ini} (≈ 360) and α' ($\approx 4 \text{ cm kV}^{-1}$), while the phase-boundary $\text{PbZr}_{0.52}\text{Ti}_{0.48}\text{O}_3$ exhibits large ϵ'_{ini} (865) and α' (87.6 cm kV^{-1}) (Table 4.1). In this context, the

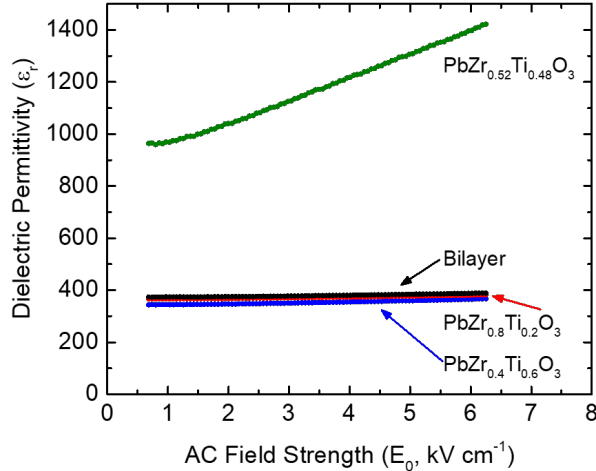


Figure 4.7. Low- and Rayleigh-regime measurements for reference samples: parent phases, bilayer heterostructures, and phase-boundary composition.

Film	ϵ'_{ini}	α' (cm kV ⁻¹)	α'/ϵ'_{ini} (cm kV ⁻¹)
$n = 2$	515	13.5	0.026
4	805	32	0.040
6	567	16.6	0.029
8	583	16.8	0.029
16	613	16.8	0.027
PbZr _{0.4} Ti _{0.6} O ₃	338	4.1	0.012
PbZr _{0.8} Ti _{0.2} O ₃	362	2.8	0.008
PbZr _{0.52} Ti _{0.48} O ₃	865	87.6	0.101
Bilayer	370	2.8	0.007

Table 4.1. Dielectric Rayleigh parameters of various single-layer films and heterostructures.

intermediate-period superlattices ($n = 4$) demonstrate enhanced ϵ'_{ini} (805) and α' (32 cm kV⁻¹) (Figure 4.7); values considerably larger than those in all other superlattices and similar to literature values for bulk PbZr_{0.52}Ti_{0.48}O₃¹⁰. This suggests that this periodicity ($n = 4$) behaves quite similarly to a phase-boundary material, yet it was created from compositions away from the phase boundary.

One potential explanation is that reducing the size (or thickness) of the ferroelectric layers destabilizes the polarization and effectively lowers the Curie temperature which would result in an enhanced room-temperature dielectric permittivity in the ultra-thin superlattices. To probe this concept, temperature-dependent dielectric measurements were completed on the parent PbZr_{0.4}Ti_{0.6}O₃ and PbZr_{0.8}Ti_{0.2}O₃ heterostructures and the $n = 4$ superlattices (Figure 4.8). These studies reveal, however, that enhancement in dielectric response does not stem simply from a lower transition temperature as Curie-Weiss analysis of the phase transition shows that the transition temperatures are 580, 500, and 560°C for PbZr_{0.4}Ti_{0.6}O₃, PbZr_{0.8}Ti_{0.2}O₃, and $n = 4$ superlattice heterostructures, respectively. Motivated by the observation of this strong periodicity dependence of the small-field dielectric response, I proceed to study ferroelectric behavior under large applied fields wherein I expect to observe hysteresis phase-boundary-like switching behavior.

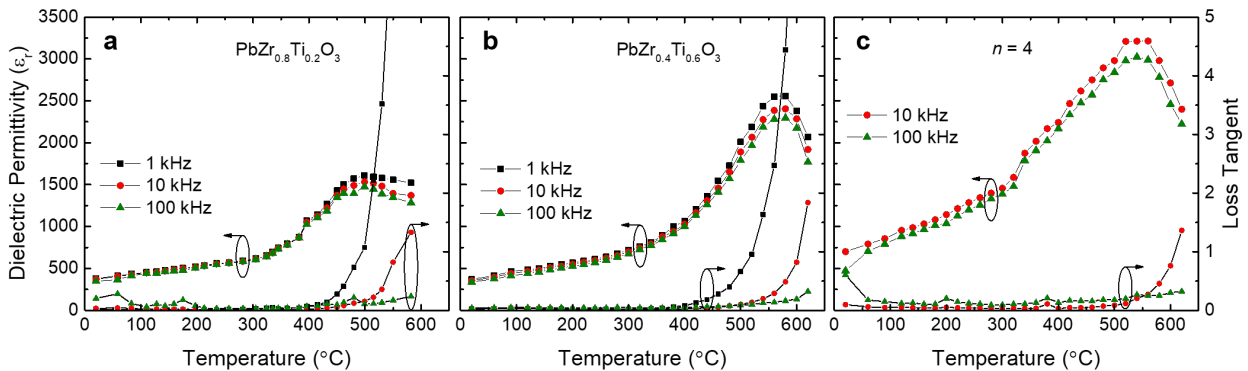


Figure 4.8. Transition temperatures as indicated by dielectric permittivity are persistent between (a),(b) parent phases and (c) $n = 4$ superlattice.

4.6. Periodicity-independent polarization saturation

Polarization and current-electric field hysteresis loops (for brevity shown only at 10 kHz) demonstrate the evolution of both the polarization and switching current in the heterostructures. Hysteresis loops for the parent phases $\text{PbZr}_{0.8}\text{Ti}_{0.2}\text{O}_3$ (Figure 4.9a) and $\text{PbZr}_{0.4}\text{Ti}_{0.6}\text{O}_3$ (Figure 4.9b) show a large saturation polarization $P_s = 67 \mu\text{C cm}^{-2}$ and a single switching event as illustrated by the single current peak (yellow for $\text{PbZr}_{0.8}\text{Ti}_{0.2}\text{O}_3$ and blue for $\text{PbZr}_{0.4}\text{Ti}_{0.6}\text{O}_3$). The $\text{PbZr}_{0.52}\text{Ti}_{0.48}\text{O}_3$ phase exhibits a much smaller saturation polarization ($P_s = 45 \mu\text{C cm}^{-2}$, Figure 4.9c). The bilayer (Figure 4.9d) and superlattice heterostructures (Figure 4.9e-i) exhibit a consistent $P_s = 64 \mu\text{C cm}^{-2}$. In the current loops, two switching events are evident (as illustrated by the two current peaks) with an intensity ratio that is related to the volume fraction of the parent phases in the heterostructures. The two switching events, therefore, are hypothesized to be related to the two parent phases present. The puzzling conclusion from this data is that the intermediate-period superlattices ($n = 4$) do not behave like the phase-boundary film, but instead are similar to the other superlattice periodicities which show indications of mixed-parent-phase behavior.

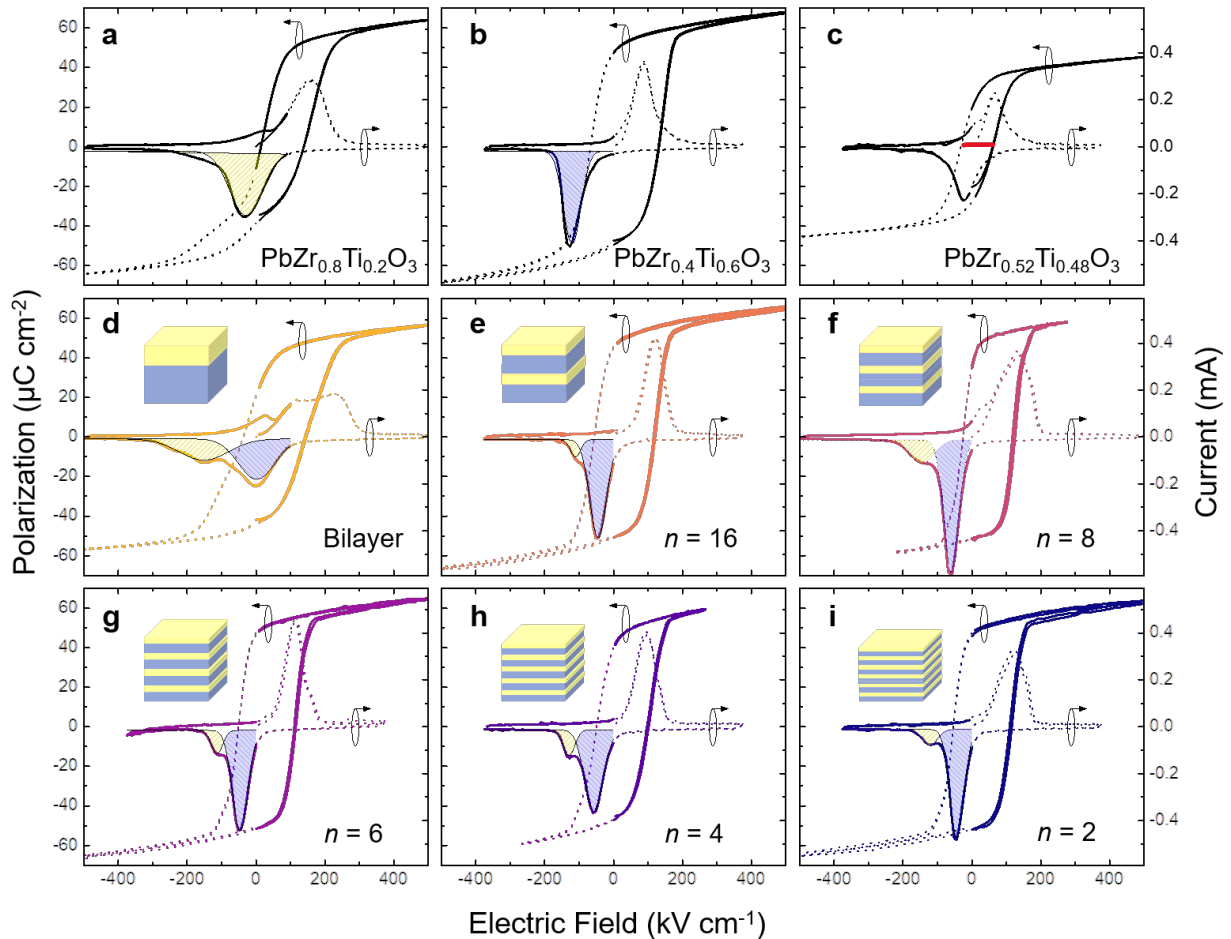


Figure 4.9. Ferroelectric current-voltage behavior for (a-c) single layer parent films, (d) bilayer, and (e-g) superlattices taken at 10 kHz. Polarization and current are simultaneously shown to show constant polarization saturation and varying mixed-step intensities as superlattice periodicity increases.

Intermediate-period superlattices ($n = 4$) have the most interesting behavior, wherein there is both enhanced permittivity (*i.e.*, large $\epsilon_r = 776$ at 10 kHz, $\epsilon'_{ini} = 805$ and $\alpha' = 32 \text{ cm kV}^{-1}$) akin to phase-boundary-like response and simultaneously large saturation polarization ($P_s = 64 \mu\text{C cm}^{-2}$) akin to the parent-phase materials and other superlattices. While the large-field switching response is consistent among the various superlattices, the small-field dielectric response varies greatly with periodicity.

4.7. Pushing the limit of dielectric Rayleigh studies

This unusual combination of large dielectric permittivity and ferroelectric polarization in the intermediate-period superlattices ($n = 4$) calls for further study as a function of external bias. Here, I extended the dielectric Rayleigh measurements (which are typically performed in sub-switching fields) to the third regime – the switching-field regime – at higher fields. Parent phases

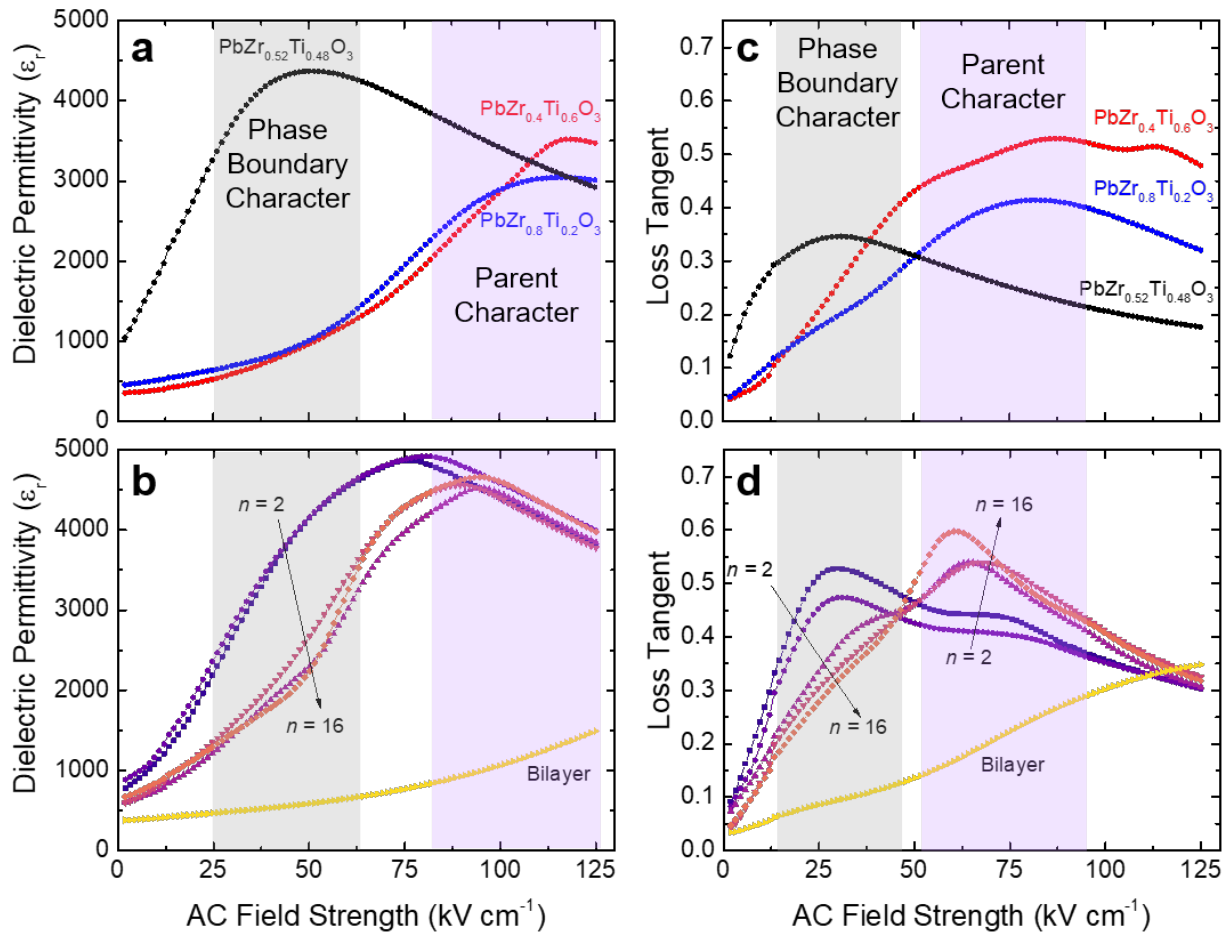


Figure 4.10. Dielectric Rayleigh measurements employed at switching fields indicate split switching behavior in (a),(b) dielectric permittivity. (c) Reference parent phases require a large AC field strength (50-90 kV cm^{-1}) whereas the single-layer $\text{PbZr}_{0.52}\text{Ti}_{0.48}\text{O}_3$ exhibits switching at a smaller AC field strength (15-40 kV cm^{-1}). (d) Superlattice samples exhibit a varying proportion of small and large AC field switching events as a function of periodicity.

$\text{PbZr}_{0.8}\text{Ti}_{0.2}\text{O}_3$ and $\text{PbZr}_{0.4}\text{Ti}_{0.6}\text{O}_3$ exhibit peaks in the dielectric response corresponding to switching at relatively large fields (80-125 kV cm^{-1}), whereas phase-boundary $\text{PbZr}_{0.52}\text{Ti}_{0.48}\text{O}_3$ exhibits a peak corresponding to switching at lower fields (25-60 kV cm^{-1}) (Figure 4.10a). This behavior can be used as a reference frame to understand the response of the superlattice heterostructures which exhibit features similar to both $\text{PbZr}_{0.52}\text{Ti}_{0.48}\text{O}_3$ (*i.e.*, low-field response within the switching-field regime) and the parent phases $\text{PbZr}_{0.8}\text{Ti}_{0.2}\text{O}_3$ and $\text{PbZr}_{0.4}\text{Ti}_{0.6}\text{O}_3$ (*i.e.*, high-field response within the switching-field regime). While all bilayer and superlattice heterostructures exhibit some features of parent- and phase-boundary-like character in the switching-field regime, the short- and intermediate-period superlattices ($n = 2, 4$) have a particularly pronounced phase-boundary character and the long-period superlattices ($n \geq 6$) and bilayer heterostructures have pronounced parent character (Figure 4.10b). This mixed phase-boundary- and parent-like character suggests that while aspects of the response of the parent $\text{PbZr}_{0.8}\text{Ti}_{0.2}\text{O}_3$ and $\text{PbZr}_{0.4}\text{Ti}_{0.6}\text{O}_3$ materials are maintained, the intimate interfacing of these materials gives rise to a response more akin to $\text{PbZr}_{0.52}\text{Ti}_{0.48}\text{O}_3$, most likely at the interface between the two layers. Additional insight in this regard can be extracted from the dielectric loss data taken simultaneously. Again, the $\text{PbZr}_{0.52}\text{Ti}_{0.48}\text{O}_3$ phase exhibits a peak in loss at lower fields (20-50 kV cm^{-1}) while the parent phases $\text{PbZr}_{0.8}\text{Ti}_{0.2}\text{O}_3$ and $\text{PbZr}_{0.4}\text{Ti}_{0.6}\text{O}_3$ exhibit peaks in loss at relatively larger fields (50-90 kV cm^{-1}) (Figure 4.10c). Likewise, all superlattice heterostructures exhibit mixed loss character (*i.e.*, loss signatures at both low and high fields), but in general the shorter the superlattice period ($n \leq 4$) the larger the proportion of the small-field effects, whereas the opposite trend is observed for long-period superlattices. In turn, this suggests that the superlattices with more interfaces exhibit more phase-boundary-like switching behavior, thus a higher permittivity in small fields, while maintaining aspects of ferroelectric polarization switching akin to that of the parent phases $\text{PbZr}_{0.8}\text{Ti}_{0.2}\text{O}_3$ and $\text{PbZr}_{0.4}\text{Ti}_{0.6}\text{O}_3$.

4.8. First-order reversal curve analysis

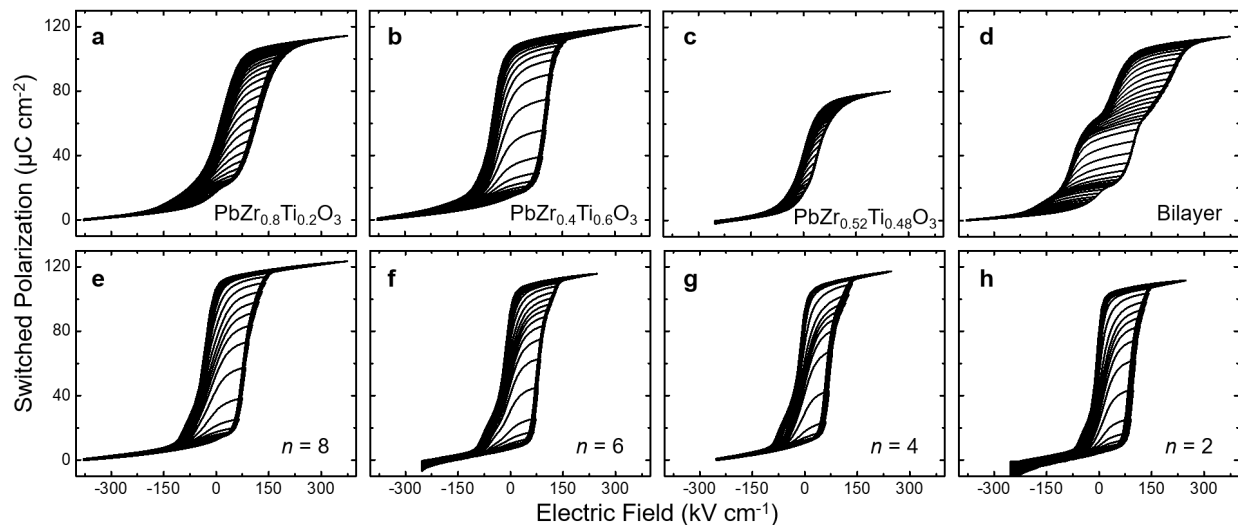


Figure 4.11. Minor polarization-hysteresis loops from which FORC plots are extracted.

Large-field Rayleigh studies suggest the potential for a complex switching process wherein – particularly in the superlattices – multiple switching phenomena including aspects not only related to the parent phases ($\text{PbZr}_{0.8}\text{Ti}_{0.2}\text{O}_3$ and $\text{PbZr}_{0.4}\text{Ti}_{0.6}\text{O}_3$), but also to the phase boundary $\text{PbZr}_{0.52}\text{Ti}_{0.48}\text{O}_3$. To probe this idea, first-order reversal curve (FORC) analysis, which reveals the Preisach distribution of switchable units (so-called hysterons) over bias and coercive fields¹²⁵, was performed by measuring a series of minor loops at 1 kHz. All heterostructures were first poled with a negative bias and gradually switched with positive biases of increasing magnitude (Figure 4.11)¹⁶². Analyses of the $\text{PbZr}_{0.8}\text{Ti}_{0.2}\text{O}_3$ (Figure 4.12a) and $\text{PbZr}_{0.4}\text{Ti}_{0.6}\text{O}_3$ (Figure 4.12b) parent phases reveal singular FORC distributions wherein $\text{PbZr}_{0.4}\text{Ti}_{0.6}\text{O}_3$ has a larger coercive field ($\sim 70 \text{ kV cm}^{-1}$ versus $\sim 50 \text{ kV cm}^{-1}$). The $\text{PbZr}_{0.52}\text{Ti}_{0.48}\text{O}_3$ phase-boundary material (Figure 4.12c) demonstrates a much lower coercive field ($\sim 20 \text{ kV cm}^{-1}$) consistent with the polarization-electric field hysteresis loops (Figure 4.9). The bilayer heterostructures (Figure 4.12d) exhibit two distinct distributions likely arising from the two parent-phase layers. These two switching distributions are matched in coercive field ($\sim 80 \text{ kV cm}^{-1}$), which suggests that the entirety of the film switches together to prevent large penalties in electrostatic energy. Because two-thirds of the total ferroelectric layer volume is comprised of $\text{PbZr}_{0.4}\text{Ti}_{0.6}\text{O}_3$, which has a large coercive field, it sets the overall coercive field for the entire film and pushes the switching distribution of the $\text{PbZr}_{0.8}\text{Ti}_{0.2}\text{O}_3$ component to match in coercive field. In the superlattice heterostructures (Figure 4.12e-h), a third distribution emerges at lower coercive fields ($\sim 36 \text{ kV cm}^{-1}$) which can be attributed to a phase-boundary-like interfacial region. To better quantify the periodicity-dependent

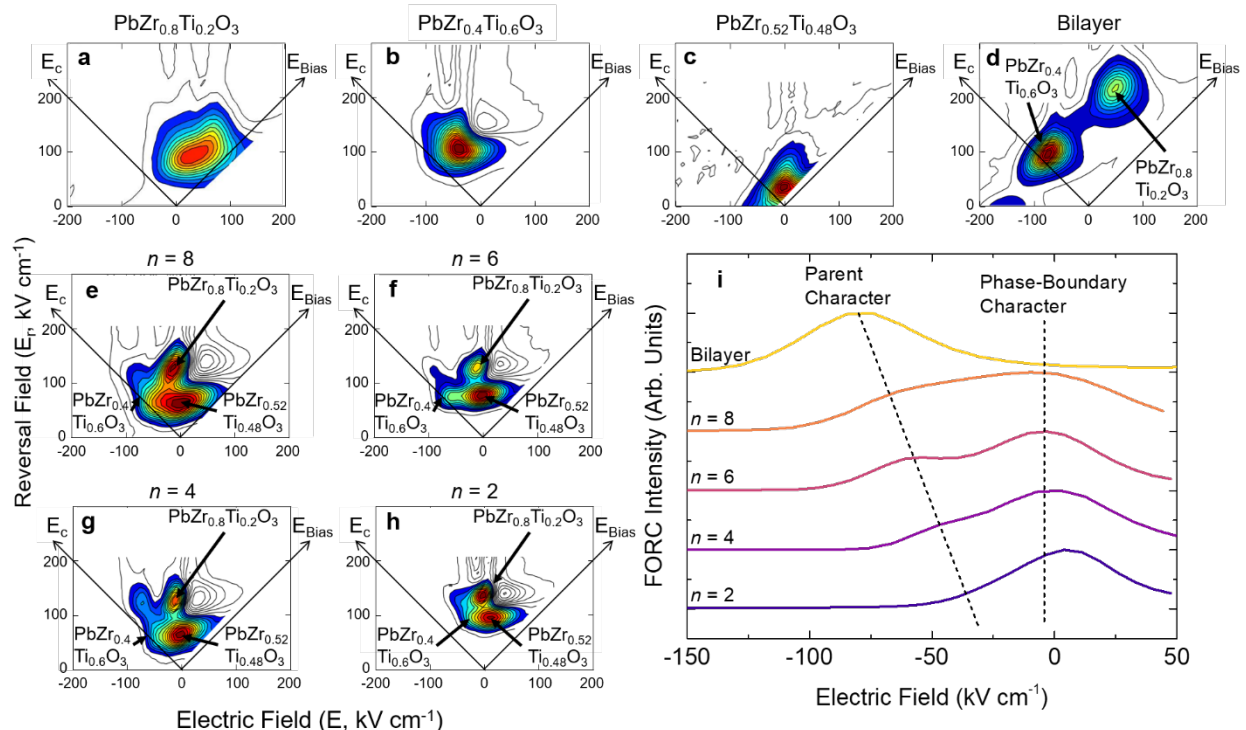


Figure 4.12. Polarization-electric field hysteresis measured between a negative saturation field and increasing positive reversal fields for (a) a reference single-layer film and (b-d) corresponding FORC contour plots. (e) Bilayer heterostructure shows two distinct switching events. (f) Superlattice minor loops are analyzed with (g-j) FORC to reveal a third switching event at high coercive fields for various periodicities.

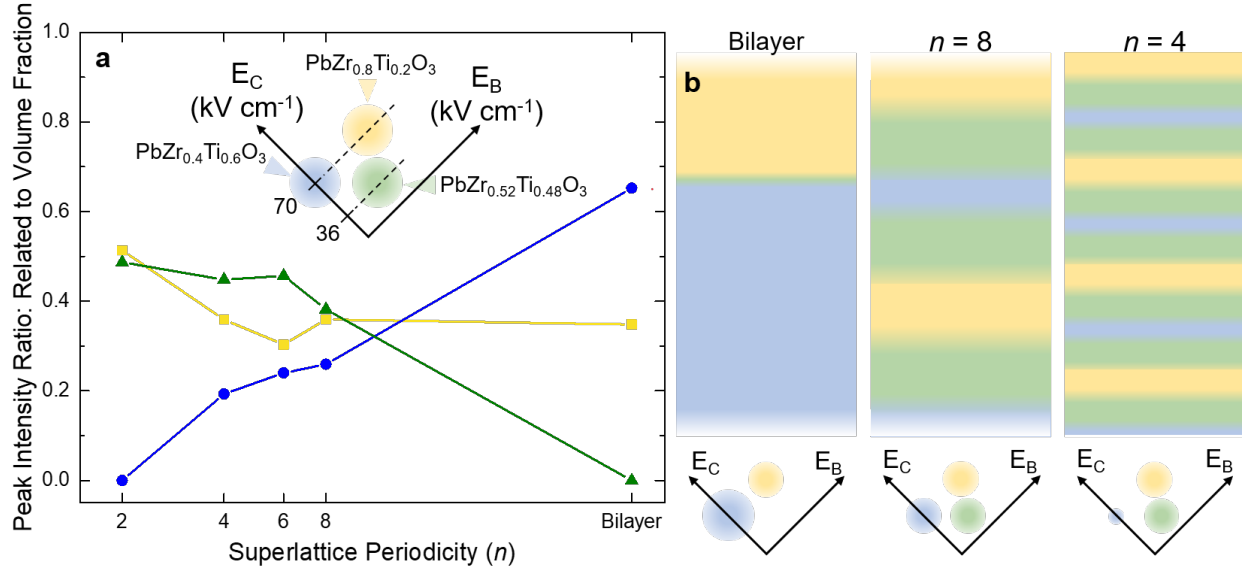


Figure 4.13. (a) The evolution of peak intensities for various FORC distributions as a function of superlattice periodicity. (b) Schematic representation of the evolution of peak intensities for various FORC distributions wherein an increasing phase-boundary-like green peak (corresponding to volume fraction) with decreasing superlattice periodicity (n).

evolution of the different switching distributions, a line-profile of the FORC distribution was taken at a reversal field of $\sim 70 \text{ kV cm}^{-1}$ (cutting through both the distributions attributed to parent $\text{PbZr}_{0.4}\text{Ti}_{0.6}\text{O}_3$ and phase-boundary $\text{PbZr}_{0.52}\text{Ti}_{0.48}\text{O}_3$). As the superlattice periodicity is shortened, two changes are observed. First, there is a decrease in the intensity of the distribution attributed to the parent- $\text{PbZr}_{0.4}\text{Ti}_{0.6}\text{O}_3$ -like character simultaneous to an increase in the intensity of the distribution attributed to the phase-boundary-like character (Figure 4.12i). Second, the distinct switching distributions start to converge as the distribution attributed to the parent- $\text{PbZr}_{0.4}\text{Ti}_{0.6}\text{O}_3$ -like character shifts to lower fields.

Additional insight about the evolution of the heterostructures can be extracted by recalling that the Preisach density of each FORC distribution (Figure 4.12) also indicates a population map of switching fields in a material¹⁶³, thus the FORC peak intensity can be related to a volume fraction of material responsible for that distribution. For example, in the bilayer heterostructures the ratio of distribution intensities attributed to the parent- $\text{PbZr}_{0.4}\text{Ti}_{0.6}\text{O}_3$ - (blue) and parent- $\text{PbZr}_{0.8}\text{Ti}_{0.2}\text{O}_3$ -like (yellow) character is consistent with the heterostructure volume fraction (66% $\text{PbZr}_{0.4}\text{Ti}_{0.6}\text{O}_3$ and 33% $\text{PbZr}_{0.8}\text{Ti}_{0.2}\text{O}_3$; a 2:1 ratio) (Figure 4.13a). As the superlattice periodicity is shortened, the intensity of the distribution attributed to the parent- $\text{PbZr}_{0.4}\text{Ti}_{0.6}\text{O}_3$ -like character decreases and the intensity of the distribution attributed to the phase-boundary-like character (green) increases. The intensity of the distribution attributed to the parent- $\text{PbZr}_{0.8}\text{Ti}_{0.2}\text{O}_3$ -like character remains relatively unchanged with periodicity, which is attributed to the larger difference in chemical proximity to the phase-boundary for this composition than the parent- $\text{PbZr}_{0.4}\text{Ti}_{0.6}\text{O}_3$ phase. This suggests that as the number of interfaces is increased, the fraction of material in the superlattices exhibiting phase-boundary-like character increases – a trend shown schematically (and quantitatively based on the intensity evolution of the FORC distributions; Figure 4.13b). In the bilayer heterostructures, the predominant character is that of the parent phases; essentially no phase-boundary-like character is observed. Upon transition, first to the $n = 8$ and then to the $n = 4$

superlattices, however, increasingly strong phase-boundary-like character is observed in the FORC corresponding to increasing interfacial volume behavior more like that material. In the short-period superlattices ($n = 2$), the three FORC distributions merge together, albeit with a higher coercive field than in the reference single-layer phase-boundary $\text{PbZr}_{0.52}\text{Ti}_{0.48}\text{O}_3$, suggesting that even in this ultra-thin structure, some remnant parent character is maintained. This also explains why this film retains the same coercive field as other superlattices.

4.9. Conclusions

In conclusion, this work examined the role of superlattice periodicity in the observation of simultaneous large susceptibility and polarization in the $\text{PbZr}_{1-x}\text{Ti}_x\text{O}_3$ system. While atomically-precise $(\text{PbZr}_{0.8}\text{Ti}_{0.2}\text{O}_3)_n/(\text{PbZr}_{0.4}\text{Ti}_{0.6}\text{O}_3)_{2n}$ superlattices with overall film chemistry near the MPB exhibit uniformly large polarization, there is significant superlattice-periodicity-dependent evolution of the dielectric permittivity and switching behavior. FORC studies reveal separate switching events for each of the parent layers in addition to a phase-boundary-like interfacial layer – with the intensity of the latter increasing as the superlattice period is shortened. This corresponds to the creation of a large volume fraction of phase-boundary-like character at the interfaces in these heterostructures such that one can simultaneously achieve large polarization (enabled by the remnant parent character in those layers) and large permittivity (enabled by the emergent interfacial phase-boundary-like character layers). Ultimately, this study opens a pathway for artificial heterostructure design to enhance responses to external perturbation.

Chapter 5

Artificial relaxor behavior in $(\text{BaTiO}_3)_n/(\text{SrTiO}_3)_n$ superlattices

This Chapter describes relaxor-like behavior, which is typically associated with chemical inhomogeneity/complexity in solid solutions, in atomically precise $(\text{BaTiO}_3)_n/(\text{SrTiO}_3)_n$ symmetric superlattices. Using reflection high-energy electron diffraction assisted pulsed-laser deposition, a range of symmetric superlattice structures are produced. X-ray diffraction and scanning-transmission electron microscopy reveal the production of high-quality structures and interfaces. Then, dielectric studies as a function of temperature reveal frequency dispersion of dielectric response which increases in magnitude as the periodicity decreases. Subsequent Vogel-Fulcher analysis confirms the frequency dispersion of the dielectric maxima across a range of periodicities and the presence of relaxor-like behavior which becomes more robust at shorter periods. Next, bond valence molecular dynamics (BVMD) simulations suggest that the relaxor-like behavior observed experimentally in the shorter-period superlattices ($n = 4$) arises from temperature-driven size variations of antipolar stripe domains in contrast to the more thermally stable dipolar configurations in the longer-period superlattices ($n = 6$ and $n = 16$). 2D discrete wavelet transforms, used to quantify spatial and temporal dipolar correlations, reveal that the phenomenological Vogel-Fulcher freezing temperature marks the transition between a relaxor-like phase and one with diagonal antipolar domains. Moreover, the size and shape of the antipolar domains are tuned by superlattice periodicity following Kittel's Law thus providing an artificial route to relaxor-like behavior which may expand the ability to control desired properties in these complex systems.

5.1. Introduction

Superlattices, or unit-cell-precise layered structures, provide researchers with the ability to fine tune competing energy contributions and leverage the interplay of various degrees of freedom in complex oxides to produce emergent phenomena. Those energies and interactions can be further manipulated via epitaxial strain, superlattice periodicity, superlattice asymmetry, and other variables which make oxide-based superlattices a veritable playground for new effects. Superlattices based on alternating layers of ferroelectric and dielectric materials, in particular, have garnered considerable interest due to the prospect of producing exotic polar order and function such as improper ferroelectricity, vortex structures, skyrmions, and large piezoelectric responses^{64,66,69}. Such superlattice structures provide researchers with the opportunity to control the energy landscape of materials by manipulating the electrostatic, elastic, and gradient energies systematically, thus providing a route to induce exotic order and function. For example, in $(\text{PbTiO}_3)_n/(\text{SrTiO}_3)_n$ (where n is the number of unit cells) superlattices alone, researchers have shown the onset of improper ferroelectricity^{64,70}, flux-closure domain structures⁶⁵, and emergent-

polar structures such as vortices^{66,67,71} and skyrmions^{69,164}. Superlattice structures have even been used in all-ferroelectric layered structures to enhance ferroelectric polarization and dielectric response simultaneously as was recently demonstrated in the $\text{PbZr}_{1-x}\text{Ti}_x\text{O}_3$ system¹⁶⁵. These examples illustrate the expansive design space and potential to explore behavior beyond previously reported novel phases and enhanced properties in oxide superlattices.

5.2. Prior art in the $\text{Ba}_{1-x}\text{Sr}_x\text{TiO}_3$ system

Yet another superlattice system that has been widely studied is $(\text{BaTiO}_3)_n/(\text{SrTiO}_3)_n$ ^{139,140,166}, where BaTiO_3 (SrTiO_3) is a prototypical ferroelectric (dielectric). As a solid solution, $\text{Ba}_{1-x}\text{Sr}_x\text{TiO}_3$ has been widely investigated and utilized for its dielectric properties^{167,168}, including nonlinear dynamics¹⁶⁶ and high tunability¹⁶⁹. As a superlattice, $(\text{BaTiO}_3)_n/(\text{SrTiO}_3)_n$ has been studied in an attempt to enhance polarization values, produce exotic domain structure, etc. Going back to even some of earliest work on these superlattices, researchers reported effects akin to what is typically observed in relaxors^{40,170}. Despite these intriguing observations, the attention has been more focused on tuning interlayer strain to produce a broad range of physical properties^{139,140}, and less on explaining the mechanism behind effects such as the relaxor-like behavior. Observation of relaxor-like order in superlattice structures is surprising since it is typically observed in chemically disordered materials^{40,131,171} such as $(1-x)\text{PbMg}_{1/3}\text{Nb}_{2/3}\text{O}_3-x\text{PbTiO}_3$ ^{170,172}, wherein local heterogeneous chemical fluctuations drive a shallow potential energy barrier between competing structures, leading to a distribution of polar domains, relaxation frequencies, and consequent frequency dispersion of dielectric response. Such behavior, at least in part, is ascribed to strong disorder and variation in the valence state of *A*- and *B*- site cations in a solid solution³⁸. In the $(\text{BaTiO}_3)_n/(\text{SrTiO}_3)_n$ system, *A*-site barium and strontium cations can be precisely layered in a superlattice structure, thus begging the question: can one artificially design relaxor properties? To answer this question, the mechanism driving relaxor behavior in this system must be understood.

5.3. Experimental superlattices – growth and structure

Here, I explore $(\text{BaTiO}_3)_n/(\text{SrTiO}_3)_n$ superlattices both experimentally and theoretically, with the goal of confirming relaxor-like behavior and subsequently explaining the mechanism behind its origin. Using reflection high-energy electron diffraction (RHEED)-assisted pulsed-laser deposition, superlattices of the form $(\text{BaTiO}_3)_n/(\text{SrTiO}_3)_n$ ($n = 4$ -20 unit cells) have been produced. While X-ray diffraction and scanning-transmission electron microscopy reveal the production of high-quality structures and precise interfaces, frequency- and temperature-dependent dielectric studies reveal enhanced permittivity and tunability as the periodicity decreases. Vogel-Fulcher (VF) analysis confirms frequency dispersion of the dielectric maxima across a range of periodicities and the presence of relaxor-like behavior which becomes more robust at shorter periods. Bond valence molecular-dynamics simulations (BVMD) indicate that the relaxor-like behavior in the shorter-period superlattices ($n = 4$) derives from thermally induced width modulations of antipolar stripe domains as opposed to the more temperature-independent dipolar configurations in the longer-period superlattices ($n = 6$ and $n = 16$). In addition to introducing a novel strategy for quantifying dipolar correlations, this study sheds light on the mechanism of

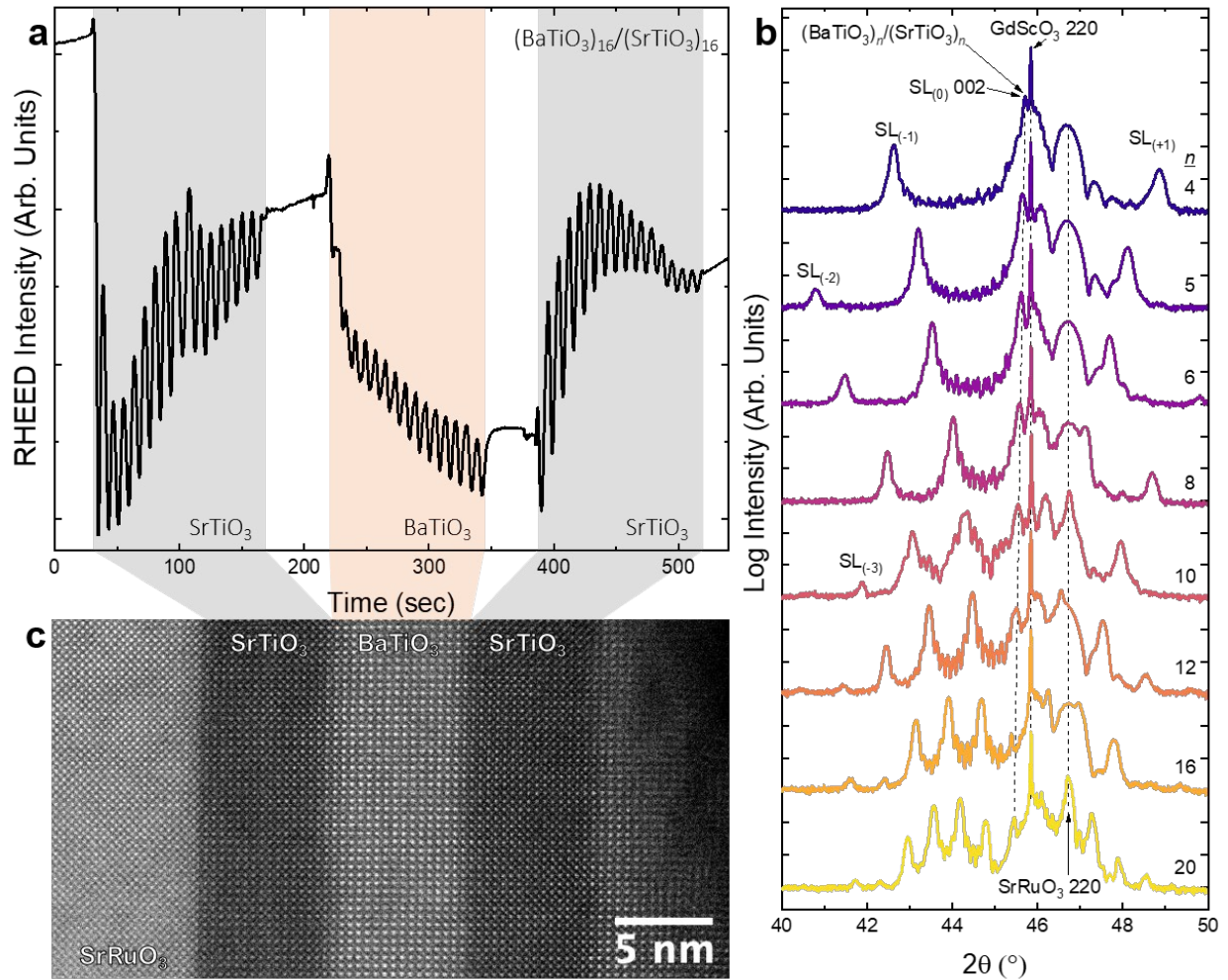


Figure 5.1. (a) RHEED-assisted PLD of $(\text{BaTiO}_3)_{16}/(\text{SrTiO}_3)_{16}$ demonstrates persistent layer-by-layer deposition control. (b) θ - 2θ X-ray diffraction patterns about the 002-diffraction condition for various superlattice periodicities (n). (c) HAADF-STEM image confirming sharp deposition control in $(\text{BaTiO}_3)_{16}/(\text{SrTiO}_3)_{16}$.

Vogel-Fulcher freezing in $(\text{BaTiO}_3)_n/(\text{SrTiO}_3)_n$ and outlines a pathway for artificial design of relaxational properties in superlattices.

The current work focuses on symmetric $(\text{BaTiO}_3)_n/(\text{SrTiO}_3)_n$ ($n = 4, 5, 6, 8, 10, 12, 16,$ and 20 unit cells) superlattice heterostructures with overall film composition of $\text{Ba}_{0.5}\text{Sr}_{0.5}\text{TiO}_3$ synthesized via RHEED-assisted pulsed-laser deposition on 20 nm $\text{SrRuO}_3/\text{GdScO}_3$ (110) substrates (Methods). GdScO_3 was selected as the substrate due to its lattice parameter ($a_{\text{pc}} = 3.96$ Å) being between that of BaTiO_3 ($a_{\text{pc}} = 4.005$ Å; where pc denotes pseudocubic) and SrTiO_3 ($a = 3.905$ Å) and thus induces moderate compressive strain on the BaTiO_3 (-0.8%) and tensile strain on the SrTiO_3 (1.6%). Note that, in the BVMD simulations, this compressive strain is applied artificially by fixing the in-plane a and b lattice constants. As a comparative reference, a single-layer $\text{Ba}_{0.6}\text{Sr}_{0.4}\text{TiO}_3$ solid-solution film (henceforth referred to as the single-layer film) was grown

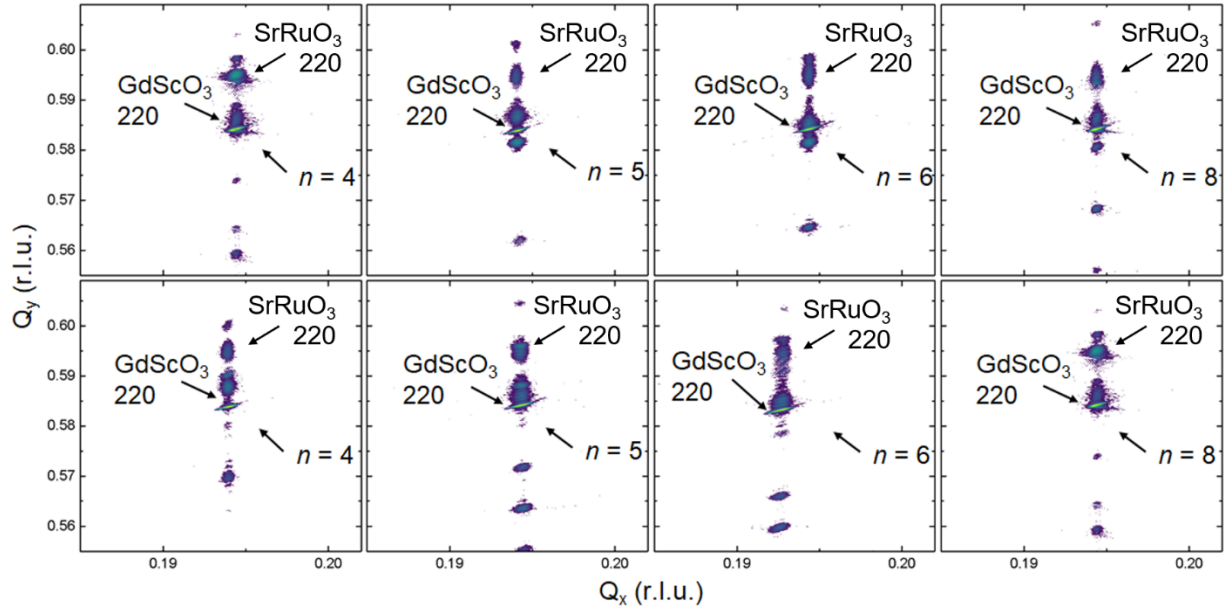


Figure 5.2. Off-axis reciprocal space maps about the 103_{pc} -diffraction condition demonstrate coherent strain for all $(\text{BaTiO}_3)_n/(\text{SrTiO}_3)_n$ superlattice structures to the GdScO_3 substrate. Superlattice fringes varying in spacing along $Q_x = 0$ according to the periodicity n of each structure.

for similar measurements. This composition was readily available and is close in chemical composition and relevant electrical properties to be used as a reference material^{169,173,174}. During the growth of the superlattice heterostructures, persistent and streaky RHEED intensity oscillations indicative of a layer-by-layer growth mode were observed for all depositions, with representative data shown for a $n = 16$ superlattice (Figure 5.1a). θ - 2θ X-ray diffraction studies reveal single-phase, fully epitaxial, $00l$ -oriented films (all 70 nm in total thickness) with superlattice peaks

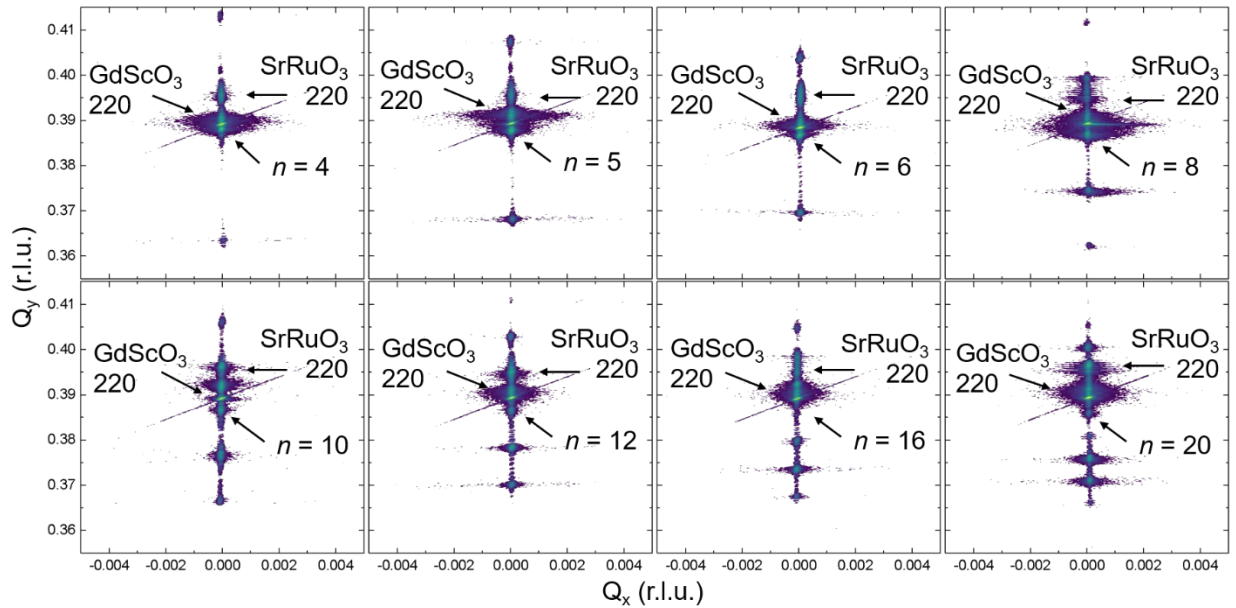


Figure 5.3. On-axis reciprocal space maps about the 002_{pc} -diffraction condition show periodic out-of-plane features as seen in the line scan at the same diffraction condition (Figure 1b). With no detectable peaks at $Q_x \neq 0$, no in-plane periodic features are observed.

varying as expected according to the evolving superlattice periodicity (Figure 5.1b). This initial structural characterization reveals high-quality superlattices have been produced. Reciprocal space maps about the 103_{pc} -diffraction conditions of the substrates and superlattices are also consistent with high-quality epitaxial growth as expected by the *in situ* RHEED and reveal that the heterostructures are all coherently strained to the substrates (Figure 5.2). On-axis reciprocal space maps at room temperature about the 002_{pc} -diffraction conditions do not show any peaks at $Q_x \neq 0$ (Figure 5.3). This indicates an absence of periodic in-plane features at room temperature (as are observed, for example, in vortex structures in $(\text{PbTiO}_3)_n/(\text{SrTiO}_3)_n$ heterostructures)⁶⁶. Z-contrast, high-angle annular dark-field (HAADF) scanning transmission electron microscopy (STEM) imaging further confirms the high-quality nature of the superlattice structures and reveals the presence of sharp interfaces between the layers, as the Z-contrast primarily comes from the barium and strontium cations (Figure 5.1c). In summation, the RHEED, X-ray diffraction, and STEM analyses all confirm high quality superlattice heterostructures with controlled periodicities and sharp interfaces (with minimal interdiffusion/mixing of the layers) have been produced. With this

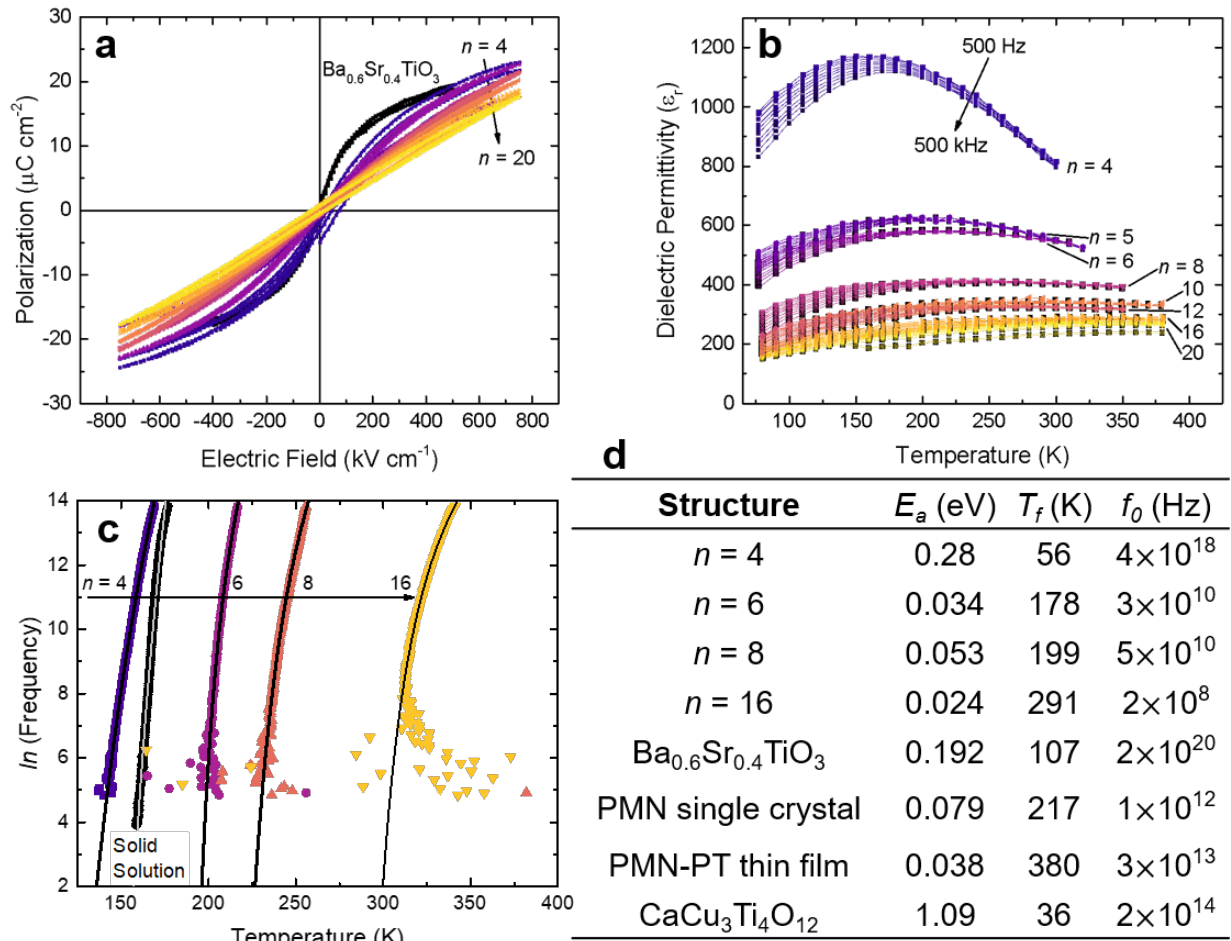


Figure 5.4. (a) Hysteresis loops demonstrate no significant remanent hysteresis across all superlattices and single-layer $\text{Ba}_{0.6}\text{Sr}_{0.4}\text{TiO}_3$. (b) Frequency-disperse temperature-dependent dielectric permittivity maxima are (c) fitted to the Vogel-Fulcher relation. (d) Vogel-Fulcher fitted parameters are tabulated for $(\text{BaTiO}_3)_n/(\text{SrTiO}_3)_n$ superlattices in addition to $\text{Ba}_{0.6}\text{Sr}_{0.4}\text{TiO}_3$ and literature values for $\text{Pb}(\text{Mg}_{0.33}\text{Nb}_{0.67})\text{O}_3$ (PMN), $0.7\text{Pb}(\text{Mg}_{0.33}\text{Nb}_{0.67})\text{O}_3-0.3\text{PbTiO}_3$ (PMN-PT), and $\text{CaCu}_3\text{Ti}_4\text{O}_{12}$.

foundation, I proceed to study the evolution of dielectric and ferroelectric properties in these heterostructures.

5.4. Relaxor behavior in electrical response

Symmetric $\text{SrRuO}_3/(\text{BaTiO}_3)_n/(\text{SrTiO}_3)_n/\text{SrRuO}_3$ capacitor structures were fabricated to enable dielectric and ferroelectric measurements (**Chapter 3**). Room-temperature polarization-electric field hysteresis loops (Figure 5.4a) reveal no significant remanence but strong polarization values at high fields ($17\text{-}23 \mu\text{C}/\text{cm}^2$) for all superlattice heterostructures and the single-layer film comparison. In general, however, non-linear response is more pronounced in short-period superlattices while long-period superlattices trend more towards linear dielectric response. As compared to the single-layer film (which demonstrates strong non-linear and non-hysteretic behavior – as expected since the transition temperature ($\sim 250 \text{ K}^{175}$) is below room temperature), the response of the shortest-period superlattices ($n = 4$) is most similar. The lack of remanence in the hysteresis loops at room temperature suggests a lack of stable long-range ferroelectric order in all heterostructures. The single-layer film and all superlattices begin to show some hysteresis upon cooling to 80 K, yet only the single-layer film reveals a robust remanent polarization consistent with that expected for a ferroelectric below its transition temperature (Figure 5.5)¹⁷⁶.

To investigate the nature of any potential phase transitions in the superlattice heterostructures, temperature- (80-350 K) and frequency-dependent (0.5-500 kHz) dielectric measurements were completed on all superlattice-heterostructure variants (Figure 5.4b). Several trends and observations are noted. First, the maximum value of dielectric response decreases systematically

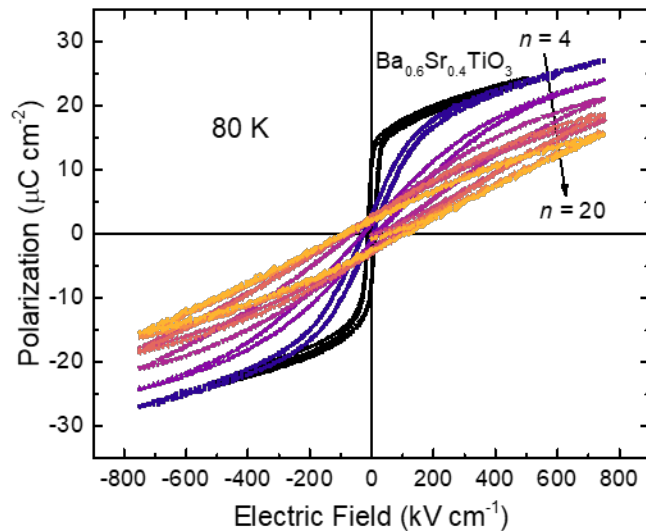


Figure 5.5. Low-temperature hysteresis loops at 80 K, 10 kHz demonstrate a lack of significant remanent polarization for superlattice samples ($n = 4, 6, 8, 10, 12, 16, 20$) in contrast to a remanent polarization $P_r = 11 \mu\text{C}/\text{cm}^2$ for $\text{Ba}_{0.6}\text{Sr}_{0.4}\text{TiO}_3$. Stronger non-linearity is demonstrated in shorter-period superlattices, maintaining the same trend from room-temperature hysteretic response.

as the periodicity n increases. Second, the temperature corresponding to the maximum in the dielectric response (T_{max}) increases as the periodicity n increases. Third, all samples show broad temperature-dependent dielectric peaks and frequency dispersion ($\Delta T_{\text{max}} = 20\text{-}35 \text{ K}$ corresponding to changing the frequency from 500 Hz to 500 kHz). In relaxor ferroelectrics, it is typical to observe a broad temperature-dependent peak and significant frequency dispersion of T_{max} (ΔT_{max})^{175,177}. Both of these features are present in all superlattice periodicities studied, but the total dielectric permittivity and ΔT_{max} are enhanced in short-period structures. For comparison, the single-layer film has a Curie temperature $\approx 165 \text{ K}$ with essentially no frequency dispersion (Figure 5.6). This suggests that, despite having similar

chemical compositions, short-period superlattice heterostructures exhibit distinctly different responses from single-layer materials.

The unique nature of the short-period superlattices is further illustrated in room-temperature capacitance-voltage measurements which reveal larger tunability in short-period superlattices. The tunability of the dielectric constant up to a dc field of 125 kV cm^{-1} jumps from 0% for $n = 16$ superlattices to 24% for $n = 4$ superlattices (Figure 5.7). The increase in tunability in short-period superlattices suggests that either the polarization or the domain structures in these superlattices must be more readily modulated. Likewise, the long-period superlattices display field-independent permittivity which is suggestive of larger energy barriers to polarization and/or domain reorientation; which is consistent with the linear shape of polarization-electric field response in long-period superlattices. Both of these ideas will be explored in more detail in the later BVMD simulations. Large tunability has been reported in $\text{Ba}_{1-x}\text{Sr}_x\text{TiO}_3$ solid-solutions (which has made such materials a focal point for numerous applications)^{169,178,179}, and the single-layer films in this study live up to this expectation with a tunability of 68% at a field strength of 125 kV cm^{-1} (Figure 5.7). These observations are consistent with heterogeneous chemical fluctuations in the solid solutions of these materials and close proximity to the Curie temperature at room temperature.

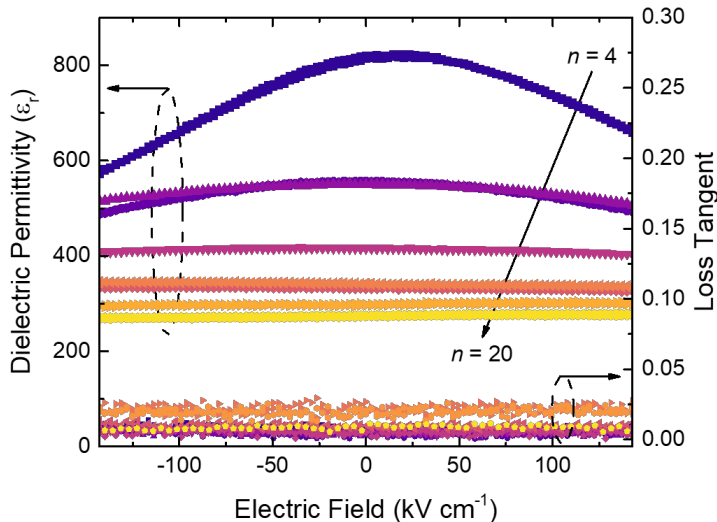


Figure 5.7. Capacitance – voltage measurements up to applied dc field strengths of 125 kV cm^{-1} demonstrate an increase in tunability at shorter superlattice periodicities. Long-period superlattices display a tunability of the dielectric permittivity near 0% and the short-period $n = 4$ superlattice shows a tunability of 24%. Low-loss tangents (<0.05) are consistent for all measurements.

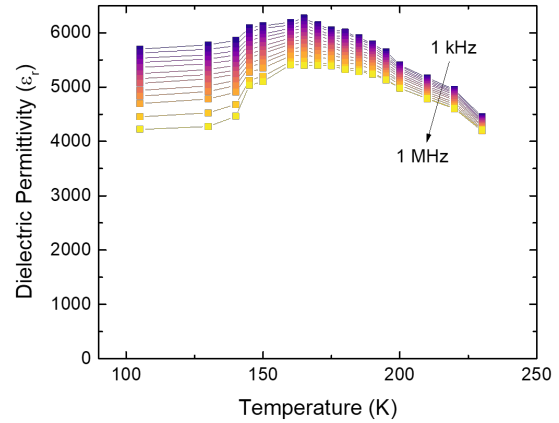


Figure 5.6. Temperature-dependent dielectric permittivity from 1 kHz to 1 MHz for $\text{Ba}_{0.6}\text{Sr}_{0.4}\text{TiO}_3$ demonstrates negligible frequency dispersion across a Curie temperature of 165 K.

proximity to the Curie temperature at room temperature.

To further explore relaxor-like behavior in this superlattice system, I analyzed the temperature- and frequency-dependent dielectric response within the VF framework (Methods)³³. For brevity and due to the similar nature of the observed responses, I downselect to the $n = 4, 6, 8,$ and 16 superlattice heterostructures and the single-layer films for this analysis (Figure 5.4c). Fitting the data with the VF relationship (Figure 5.4c, black lines) results in values that align well with existing relaxor literature (Figure 5.4d)³⁰. Dielectric response from the single-layer was fitted to the VF relation for reference, but gave

unphysical values due to its transition to a ferroelectric demonstrating negligible frequency dispersion¹⁸⁰. The activation energy E_a ranges between 0.024-0.053 eV for all periodicities longer than $n = 4$, with an increase to 0.28 eV in the $n = 4$ superlattices. The jump in activation energy is accompanied by a jump in the characteristic frequency f_0 which is $\sim 10^{18}$ Hz for the $n = 4$ superlattices compared to values in the range of 10^8 - 10^{10} Hz for longer-period superlattices. Reported relaxors such as single-crystal $\text{PbMg}_{0.33}\text{Nb}_{0.67}\text{O}_3$ (PMN), thin-film $0.7\text{PbMg}_{0.33}\text{Nb}_{0.67}\text{O}_3$ - 0.3PbTiO_3 (PMN-PT), and ceramic $\text{Ba}_{0.55}\text{Sr}_{0.45}\text{TiO}_3$ are in the same range of fitted VF parameters as those noted here for the long-period superlattices (Figure 5.4d)¹⁸¹. In the short-period superlattices, non-interfacial BaTiO_3 layers are more involved in the dielectric response (see titanium flipping frequency below), increasing the active volume responding to external fields at shorter periodicities. The increased active volume, in turn, increases the energy required to oscillate polar regions in BaTiO_3 in a dielectric-permittivity measurement. Polar domains in $n = 4$ superlattices have a lower energy barrier to not only other domain configurations, but also smaller domains. Smaller domains are consistent with the increased characteristic frequency from the VF fit. Experimental freezing temperatures (T_f) extracted from the VF relationship increase directly with superlattice periodicity, with T_f rising from 56 K in $n = 4$ to 291 K in $n = 16$. The freezing temperature increases with increasing periodicity because larger, more thermally stable domains are present in longer-period superlattices.

5.5. Molecular dynamics simulations

To understand the experimentally observed slowing down of dipolar fluctuations, *NPT*-BVMD simulations of the $n = 4, 6,$ and 16 superlattices were performed¹ in the Large-scale Atomic/Molecular Massively Parallel Simulator (LAMMPS)¹⁸² using a composition-transferable bond-valence interatomic potential for $\text{Ba}_{1-x}\text{Sr}_x\text{TiO}_3$ ¹⁷⁶. Every structure is a $20 \times 20 \times 2$ ($n+m$) supercell containing $4000(n+m)$ atoms and has two periods, i.e., $(\text{BaTiO}_3)_n/(\text{SrTiO}_3)_m/(\text{BaTiO}_3)_n/(\text{SrTiO}_3)_m$, in order to include inter-period correlations. Ti displacements of 0.05 \AA were initialized along $[111]$ so as to start from the low-temperature ferroelectric and rhombohedral phase of BaTiO_3 ¹⁸³.

To confirm that the shorter-period $(\text{BaTiO}_3)_n/(\text{SrTiO}_3)_n$ superlattices ($n = 4$ and 6) give rise to relaxor-like phases, I analyze the temperature- and periodicity-dependent evolution of the underlying dipolar structure in the BVMD simulations. Dynamics snapshots of the equilibrium minimum-potential-energy dipolar configuration reveal a relaxor-like polarization texture as a function of temperature (horizontal axis) and periodicity (vertical axis) (Figure 5.8). First, I will discuss the short-period $n = 4$ superlattice. At temperatures less than 50 K, a phase with ≈ 6 antipolar stripe domains per 80 \AA is preferred. Between 50 and 90 K, the number of antipolar stripe domains per 80 \AA becomes ≈ 4 . In other words, the domain width w increases from ≈ 13 to 20 \AA . From 90 to 110 K, the system favors antipolar diagonal domains, which enables the formation of

¹MD simulations were accomplished in collaboration with Dr. Robert B. Wexler and Prof. Andrew M. Rappe from the Department of Chemistry at the University of Pennsylvania and the Department of Mechanical and Aerospace Engineering at Princeton University.

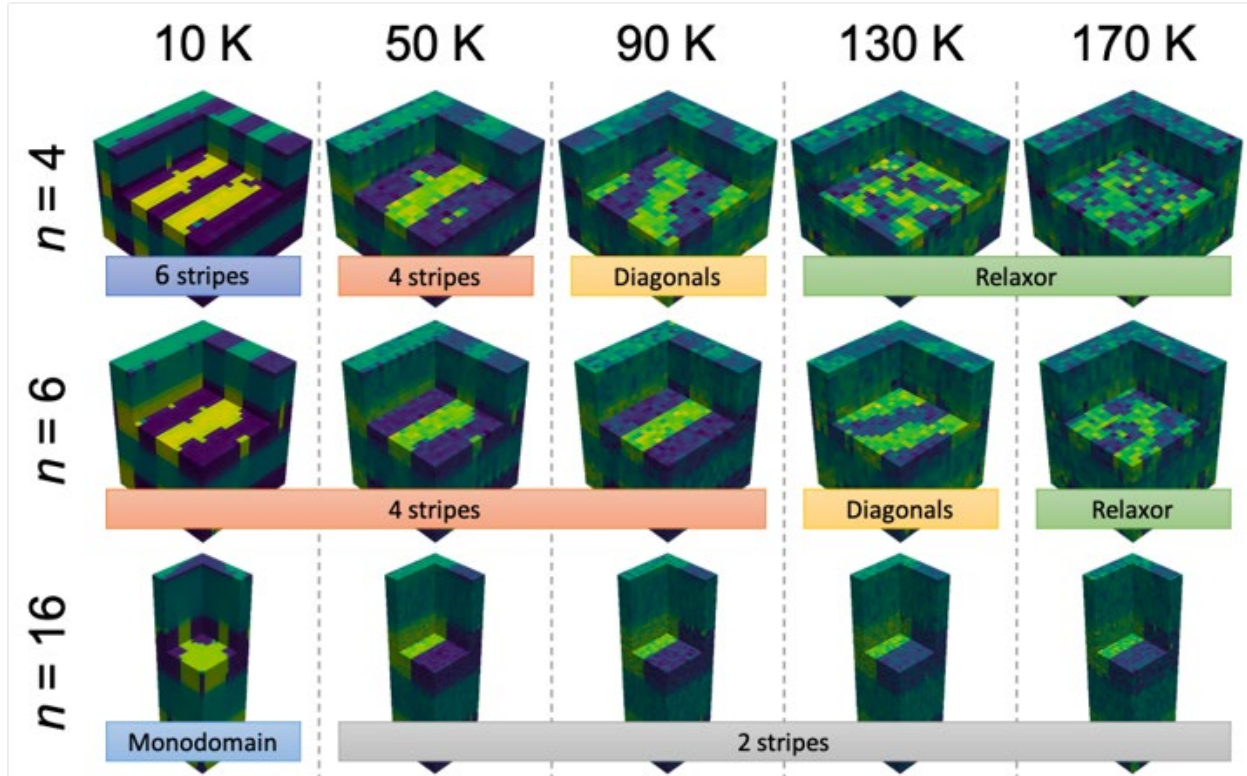


Figure 5.8. Dipolar configuration-temperature stability diagram for (top) $n = 4$, (middle) $n = 6$, and (bottom) $n = 16$. $n = 4$ has two dipolar configuration transitions ≤ 90 K whereas the lowest phase transition temperature for $n = 6$ is 130 K. Qualitatively defining T_f as the temperature above which the relaxor-like phase is stable, the results show that $n = 4$ freezes at a lower temperature (90 K) than $n = 6$ (130 K) and $n = 16$ (>170 K), which agrees with the fitted Vogel-Fulcher parameters.

≈ 28 -Å-wide stripe domains in the simulation cell. Therefore, at temperatures less than or equal to 110 K, the dipolar-structure evolution of the $n = 4$ superlattice upon heating (cooling) is characterized by the widening (narrowing) of domains. Finally, above 110 K, a relaxor-like phase composed of slush-like polar structures is stable. The emergence of a relaxor-like polarization texture above the calculated T_f (90 K for $n = 4$) is in excellent qualitative agreement with the experimental dielectric response. As a point of reference, the calculated and measured Curie temperatures of BaTiO_3 are 160 K¹⁸⁴ and 393 K¹⁸⁵, respectively. Considering the measurements correspond to temperatures less than 393 K, the simulated temperature range of 10-170 K is appropriate. While the thermal evolution of the $n = 6$ dipolar configuration is similar to that of $n = 4$, the stripe-diagonal and diagonal-relaxor transition temperatures are higher, and the narrowest ($w \approx 13$ Å) stripe-domain configuration disappears at low temperatures. Finally, for $n = 16$, the ground-state dipolar configuration is ≈ 2 antipolar stripe domains per 80 Å for the entire range of simulation temperatures except at those less than 50 K for which there is remanence, but it is minor in magnitude. For this reason, 50 K appears to mark the transition between antipolar stripe domains (≥ 50 K) and monodomain ferroelectric periods (< 50 K).

I now rationalize the effect of periodicity and temperature on domain width (Figure 5.8). At a constant temperature, the domain width increases with periodicity. This dependence was initially explained by Kittel^{186,187} for antipolar stripe domains in ferromagnetic materials and

recently generalized by Bennett *et al.*¹⁸⁸ for those in ferroelectric/paraelectric periodic superlattices. Both derivations begin with the following expression for the free energy per unit volume (F) of a ferroelectric thin film of thickness d in an arbitrary dielectric medium:

$$F = \frac{\sigma}{w} + F_{elec}(w, d) \quad (5.1)$$

where σ is the domain-wall energy and F_{elec} is the electrostatic depolarization energy. Upon applying the latter theory¹⁸⁸ to $(\text{BaTiO}_3)_n/(\text{SrTiO}_3)_n$, the relationship between the equilibrium domain width and periodicity is given by:

$$w^2 \approx \frac{7.37 \varepsilon_0 \sigma (\varepsilon_S + \sqrt{\varepsilon_a \varepsilon_c})}{P^2} d \quad (5.2)$$

where ε_S is the dielectric constant of SrTiO_3 , ε_a (ε_c) is the xx (zz) component of the dielectric tensor for BaTiO_3 , and P is the polarization. This relation clearly demonstrates that the domain width increases with periodicity by $w \propto \sqrt{n}$. The intuition behind the positive correlation between domain width and periodicity is that thicker layers need larger domain walls to make the same number of antipolar stripe domains per unit length. Since the energy cost of creating these domain walls is greater for thicker layers than thinner ones, the former favor fewer domain walls per unit length, *i.e.*, wider domains. At a constant periodicity, the domain width decreases with temperature. This dependence can be obtained by taking into account the measured temperature-dependence of the polarization and dielectric constants in Equation 5.2. Since the polarization increases (Figure 5.9) and the dielectric constant decreases upon cooling below T_f , the domain width should decrease with temperature.

To analyze the dipolar fluctuations within these layers, 2D discrete wavelet transforms (2D-DWTs) were employed to capture both spatial and temporal information about a given 2D signal, in this case the P_c correlations in an ab -layer of the $(\text{BaTiO}_3)_n/(\text{SrTiO}_3)_n$ superlattice structure. The 2D-DWT of a 2D dipolar configuration is calculated by transforming it to the spatial frequency domain (using wavelets), applying a series of spatial-frequency filters, and inverse transforming it back to the spatial domain. First it is passed through a low-pass filter, revealing polar domains with longer-range order because these regions change polarization with lower spatial frequencies (*i.e.*, longer spatially resolved domains). The dipolar configuration is also decomposed simultaneously using a high-pass filter, exposing domains with shorter-range order, which, for the highest spatial frequency changes in the polarization, correspond to white Gaussian “polar” noise (when biorthogonal 3.5 wavelets are used)¹⁸⁹.

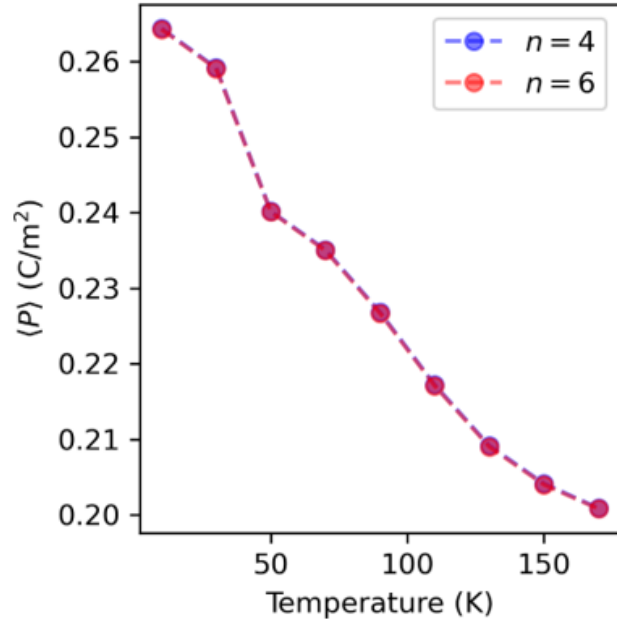


Figure 5.9. Same decrease in the average polarization of the BaTiO_3 layers upon heating for $n = 4$ and 6 .

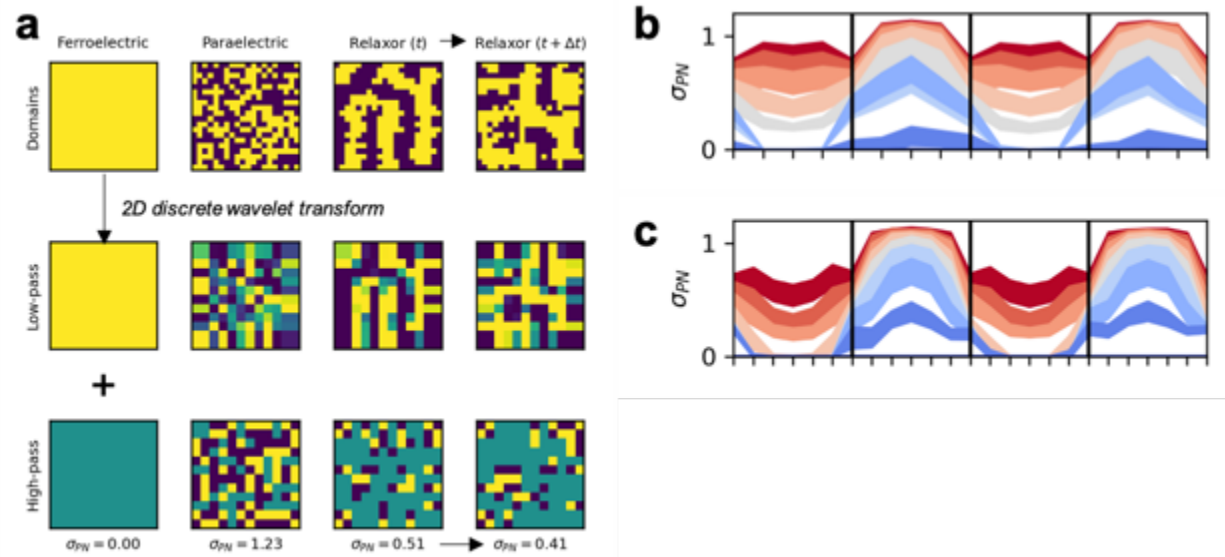


Figure 5.10. Wavelet-based estimator of the polar noise standard deviation (σ_{PN}). (a) 2D discrete wavelet transform of schematic, 2D dipolar configurations for a ferroelectric, paraelectric, relaxor at some time t , and the same relaxor some time later $t + \Delta t$. Time-averaged, layer-resolved σ_{PN} for the (b) $n = 4$, (c) $n = 6$, and (d) $n = 16$ superlattices at different temperatures. σ_{PN} and $\Delta\sigma_{PN}$ quantify spatial and temporal order, respectively.

The 2D-DWT distinguishes different degrees of dipolar order (Figure 5.10a). For a schematic monodomain ferroelectric material (Figure 5.10a – Ferroelectric), which is characterized by long-range order in either the $+c$ (yellow) or $-c$ (purple) directions (Figure 5.10a – Domains), the low-pass filter reproduces the original dipolar configuration (Figure 5.10a – Low-pass). A polar noise level σ_{PN} can be estimated as the median absolute deviation of the wavelet coefficients at the highest spatial frequencies¹⁷⁷. Therefore, in the scenario of a monodomain ferroelectric, for which no high-pass signal is detected, a background turquoise color is depicted (Figure 5.10a – High-pass), as $\sigma_{PN} = 0$. On the other hand, for a paraelectric material (Figure 5.10a – Paraelectric), which is defined by the absence of dipolar order, the 2D-DWT yields a larger $\sigma_{PN} = 1.23$. For a relaxor material (Figure 5.10a – Relaxor at time t), the expectation for dipolar ordering is somewhere between that of the extreme cases of ferroelectric and paraelectric materials ($0 < \sigma_{PN} < 1.23$) due to the coexistence of ferroelectric- and paraelectric-like phases as either slush-like polar structures³⁸ or polar nanoregions inside a nonpolar matrix³⁵. The 2D-DWT also can quantify dipolar fluctuations, in addition to their ordering, *via* the time variations of σ_{PN} (Figure 5.10a – Relaxor at time $t + \Delta t$). In other words, over a simulated period of ≈ 150 ps at equilibrium, the variation of σ_{PN} is given by its time-averaged standard deviation ($\Delta\sigma_{PN}$). This value quantifies the dynamical nature of polar domains in a material, wherein a larger $\Delta\sigma_{PN}$ indicates a highly time-varying dipolar structure. Together, σ_{PN} and $\Delta\sigma_{PN}$ can be interpreted as a measure of the dipolar order and fluctuations, respectively.

The $n = 4, 6$, and 16 $(\text{BaTiO}_3)_n/(\text{SrTiO}_3)_n$ superlattice structures show the dependence of σ_{PN} (vertical axis) and $\Delta\sigma_{PN}$ (line width) on the layer along the c lattice vector (horizontal axis) and temperature (color axis) (Figure 5.10b-c). For all n , the BaTiO_3 σ_{PN} and $\Delta\sigma_{PN}$ are less than those of SrTiO_3 at the same temperature. The former can be rationalized by the fact that bulk BaTiO_3 is ferroelectric and bulk SrTiO_3 is paraelectric, whereas the latter can be interpreted as the dipolar

dynamics being more time-invariant in ferroelectric BaTiO₃ than paraelectric SrTiO₃. Additionally, the results show that, across all periodicities studied, σ_{PN} and $\Delta\sigma_{PN}$ decrease with temperature. This demonstrates the freezing of polar domains as decreasing σ_{PN} and $\Delta\sigma_{PN}$ correspond to the ordering of the dipolar configuration and the slowing of the dipolar dynamics, respectively. Since non-interfacial BaTiO₃ layers in (BaTiO₃)_n/(SrTiO₃)_n are the closest to bulk BaTiO₃ in terms of their local structure and thus ferroelectric disposition, they are likely to serve as the nucleation center from which polar domains can freeze. Therefore, defining T_f as the temperature at which σ_{PN} and $\Delta\sigma_{PN} \rightarrow 0$ for non-interfacial BaTiO₃ layers, I find that T_f increases with periodicity (90 K for $n = 4$, 130 K for $n = 6$, and >170 K for $n = 16$), which is in excellent agreement with the experimentally measured freezing temperature. Importantly, the 2D-DWTs support the existence of relaxor-like phases in $n = 4$ and $n = 6$ superlattices at temperatures greater than T_f with intermediate dipolar order with values of σ_{PN} between 0.2-0.9 and highly-fluctuating dipoles with $\Delta\sigma_{PN} \approx 0.1-0.2$.

5.6. Conclusion

In conclusion, this work studied artificially designed relaxor behavior in the (BaTiO₃)_n/(SrTiO₃)_n system, wherein thermally induced width modulations of antipolar stripe domains short-period superlattices. Easily accessible fluctuations lead to enhancement of dielectric constant across a broad temperature range. All experimentally grown superlattices demonstrate some degree of relaxor behavior, with stronger behavior present in shorter periodicities and explained by BVMD. This study presents a mechanism for artificially defining relaxor structures in superlattices, wherein the thickness of a repeating superlattice unit can be modulated to design artificial relaxor behavior by modulating the width of antipolar stripe domains. Lastly, this work outlines design criteria based on layer thickness and dielectric permittivity for exploring complex polarization textures in ferroelectric superlattice systems.

Chapter 6

Beyond ferroelectric order: ferromagnetic order and interfacially-driven behavior

This Chapter focuses on emergent ferroic order beyond ferroelectric order. Symmetry breaking and mismatch of chemical potential at interfaces results in emergent phenomena inaccessible in the bulk. Because interfaces can reconstruct structurally and electronically, emergent phenomena can be tuned in more ways than just polar, ferroelectric order. This Chapter explores tuning ultra-thin ferromagnetic order in addition to and the electrostatic boundary conditions imposed on a ferroelectric phase by an emergent charge-ordered phase. First, I will focus on the heterointerface between ultra-thin $\text{LaCrO}_3/\text{SrTiO}_3$, which is positioned as a system with potential for emergent interfacial ferromagnetic order. The presence of ferromagnetic order at the interface between an antiferromagnet (LaCrO_3) and a diamagnet (SrTiO_3) near room temperature would be impactful for studying how spin and orbital degrees of freedom are affected at oxide heterointerfaces. Next, I will focus on the prospect of an optically induced phase metal-insulator-transition in $\text{La}_{0.67}\text{Ca}_{0.33}\text{MnO}_3$ to be utilized as either a dielectric or metallic layer adjacent to ultra-thin PbTiO_3 layers. This work can potentially turn on or off exotic polar phases such as vortices, skyrmions, etc.

6.1. Ferromagnetic order in ultra-thin LaCrO_3

Magnetism in complex oxides is mediated by strong short-range interactions and correlations between charge, spin, and orbital degrees of freedom. These interactions can be dramatically altered when placed in competition with a dissimilar material, for example at the interface between thin-film layers. Thus, interfacial engineering presents an opportunity to produce novel physical phenomena, such as new magnetic states. One example of such interface mediated properties is exchange coupling in ferromagnetic or antiferromagnetic heterostructures which has been a research focus for decades due to its application in spintronics devices such as spin valves¹⁹⁰.

In parallel, there is extensive work on heterointerfaces such as that

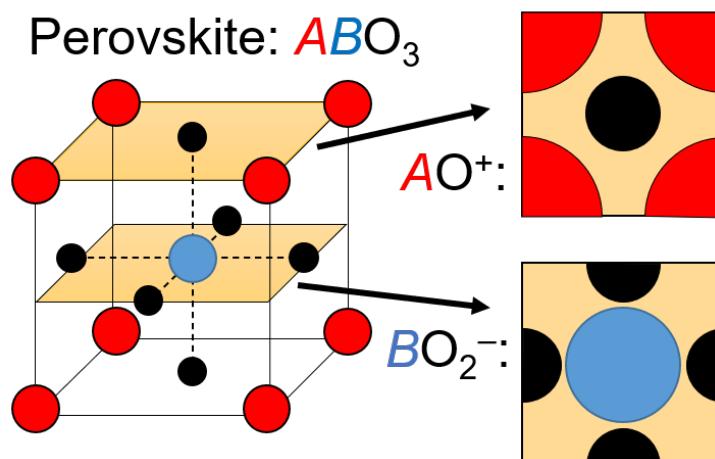


Figure 6.1. Charged layers in an oxide perovskite ABO_3 structure along the $[001]$. Alternating positive negative and positive charges in the AO^+ and BO_2^- layers build up potential in proximity to nonpolar layers, leading to a polar discontinuity and polar catastrophe.

in $\text{LaAlO}_3/\text{SrTiO}_3$ wherein charge mismatch between polar and non-polar layers in the materials provides for a built-in potential (known as a polar discontinuity) that drives accumulation of electrons near the interface, thus creating a conducting layer between these two insulators^{191–197}. Depending on the oxidation state of the *A*- and *B*-site cations, perovskites can exhibit layers with a negative, positive, or neutral charge. Neutral layers exist in non-polar materials such as SrTiO_3 , with Sr^{2+} and Ti^{4+} oxidation states. Likewise, charged layers exist in oxide perovskites with *A*-site cations in the 3+ oxidation state. Alternating charged layers in the [001] correspond to the AO^+ and BO_2^- layers in the ABO_3 perovskite structure (Figure 6.1). The built-in potential builds up a charge mismatch at the interface between two materials with different band gaps, as each unit cell builds up more charge at this polar discontinuity until a polar catastrophe occurs and charge (electrons) accumulates at the interface to negate the built-in interfacial voltage. To date, however, these studies have primarily focused on electronic reconstruction. I am interested in leveraging the polar discontinuity model to influence ferroic order parameters such as ferromagnetic order.

In this regard, researchers have applied the polar discontinuity model to magnetic transition-metal oxide systems, inducing a change in orbital occupation in manganate systems and reporting ferromagnetic states inaccessible in the bulk^{198,199}. Prior work from my colleagues has established a combined theoretical and experimental framework to understand the nature of electronic reconstruction at the $\text{LaMnO}_3/\text{SrTiO}_3$ (001) heterointerface²⁰⁰. LaMnO_3 , an antiferromagnetic insulator in the bulk, has alternating charged layers LaO^+ and MnO_2^- which result in a polar discontinuity with nonpolar SrTiO_3 . The discontinuity is compensated by an accumulation of electrons near the interface, in this case doping the LaMnO_3 and drives the formation of a ferromagnetic state mediated by double exchange interactions. This work opens opportunities for exploring emergent ferromagnetic phenomena in other systems.

Previous studies in the literature have probed the potential for a polar discontinuity at the $\text{LaCrO}_3/\text{SrTiO}_3$ (001) heterointerface, in particular looking for a possible conducting interface (which was not observed)²⁰¹. However, the magnetic state of the $\text{LaCrO}_3/\text{SrTiO}_3$ heterointerface has not been studied. In the bulk, LaCrO_3 is an antiferromagnetic insulator with a Néel temperature near room temperature. Alternating charged LaO^+ and CrO_2^- layers along the [001], when interfaced with the non-charged SrO and TiO_2 layers in SrTiO_3 along the [001] should lead to electron accumulation and emergent interfacial properties. Akin to the observed ferromagnetism in LaMnO_3 , LaCrO_3 thicker than a certain critical thickness of a few unit cells could also foster novel ferromagnetic order not observed in the bulk. Within the

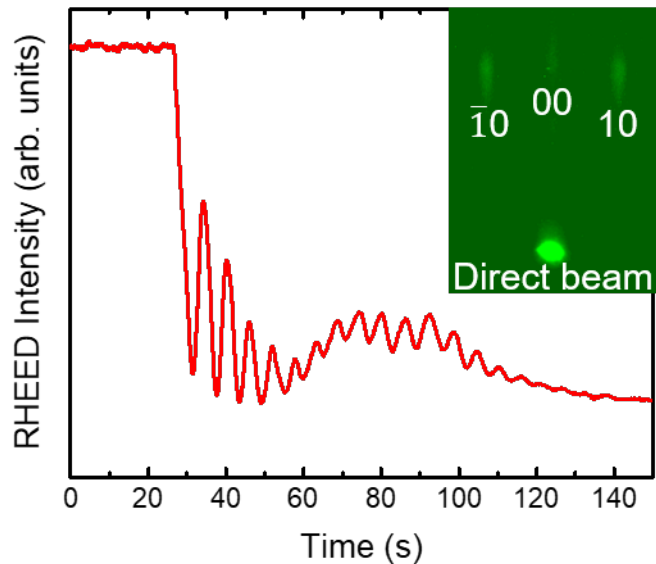


Figure 6.2. Reflection high-energy electron diffraction of LaCrO_3 grown epitaxially in the layer-by-layer growth mode on SrTiO_3 . Persistent oscillations and streaky pattern (inset) demonstrate excellent thin-film deposition *in situ*.

framework of the polar discontinuity model, a ferromagnetic state in the LaCrO_3 would manifest from an accumulation of electrons to the interface, reducing Cr^{3+} to Cr^{2+} . This change in orbital occupancy will be observable with X-ray absorption spectroscopy (XAS), and the consequent ferromagnetic order will be observable with X-ray magnetic circular dichroism (XMCD). These experiments are critical to ascertaining induced ferromagnetic order in ultra-thin heterointerfaces.

6.1.1. Initial LaCrO_3 deposition and orbital occupation

Bulk LaCrO_3 is an antiferromagnetic insulator with a pseudocubic lattice parameter $a_{pc} = 3.885 \text{ \AA}$. A SrTiO_3 substrate exerts 0.51% tensile strain on LaCrO_3 , with epitaxial growth demonstrated to be fully epitaxial and layer-by-layer within the scope of film thicknesses in this work²⁰². High-quality LaCrO_3 thin films with unit-cell precision were synthesized on TiO_2 -terminated SrTiO_3 (001) substrates by RHEED-assisted PLD. Persistent RHEED intensity oscillations and “streaky” diffraction spots indicate a layer-by-layer growth mode, which lays the foundation for a set of ideal samples in which to study the potential for interfacially driven phenomena (Figure 6.2).

I have completed preliminary XAS measurements of the Cr $L_{3,2}$ edges and have confirmed the expected 3+ oxidation state in an as-grown thick (30 nm) LaCrO_3 film (Figure 6.3). XAS is a widely used technique typically done at synchrotron facilities that probes local orbital occupancy of a material. It is achieved by using monochromatic photons to excite core electrons, wherein core electrons with principal quantum numbers $n = 1, 2, 3$ correspond to the K -, L -, and M -edge, respectively. The utility of XAS in this work is to locally detect the oxidation state and therefore probe if electron accumulation is occurring at the $\text{LaCrO}_3/\text{SrTiO}_3$ interface. Beamline 4.0.2 at the Advanced Light Source (ALS) was used to carry all these XAS measurements. XAS confirms the ability to create the parent material and obtain the baseline charge state needed for comparison. As the thickness of the film is reduced to the order of a few unit cells, the probe depth (typically $\sim 5 \text{ nm}$) of the spectroscopic techniques will increasingly detect signal from the buried heterointerfaces, as has been observed in LaMnO_3 films.

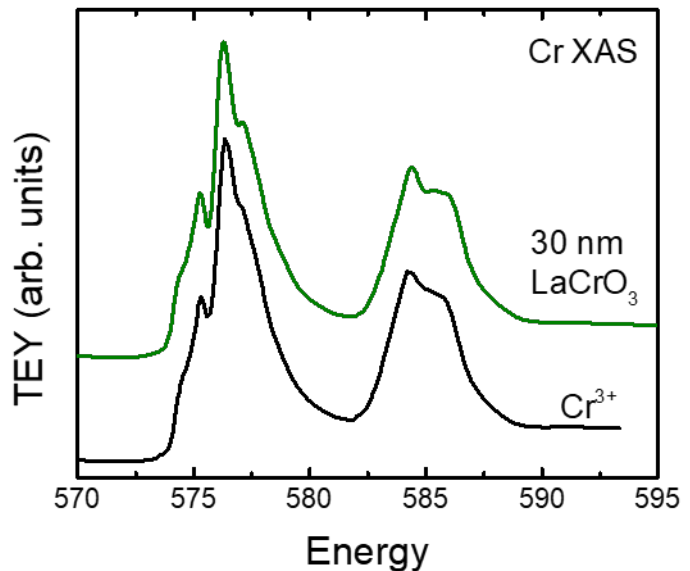


Figure 6.3. X-ray absorption spectra of Cr $L_{3,2}$ edges of a 30 nm LaCrO_3 film demonstrating a Cr^{3+} oxidation state in agreement with reference spectra.

6.1.2. Band alignment and beyond

From this foundation, a thickness series of ultra-thin films can be fabricated to probe the critical-thickness behavior on emergent ferromagnetic order at the $\text{LaCrO}_3/\text{SrTiO}_3$ heterointerface. XMCD is the ideal core-level spectroscopy to determine the spin structure and magnetism localized at the interface in thin-film oxides with just a few unit cells of thickness. The resonant enhancement of this technique is imperative for detection of interfacial magnetism because conventional magnetization measurements would struggle to deliver a signal-to-noise ratio that would allow for probing ultrathin films. ALS has the unique capabilities of providing soft X-ray energy ranges to perform measurements of the Cr L -edge while still detecting subtle signals stemming from phenomena localized at an interface.

Future efforts can explore the evolution of the valence (via XAS) and magnetic (via XMCD) states as a function of LaCrO_3 thickness, specifically in 2, 3, 4, 5, 6, 7, 8, and 10 unit-cell-thick heterostructures (with comparison to thick 30 nm films). Above the critical thickness, I expect a detectable reduction from Cr^{3+} to Cr^{2+} to appear in the Cr $L_{3,2}$ edge via XAS. The electron accumulation phenomenon found in the $\text{LaMnO}_3/\text{SrTiO}_3$, $\text{LaAlO}_3/\text{SrTiO}_3$, etc. has been shown to

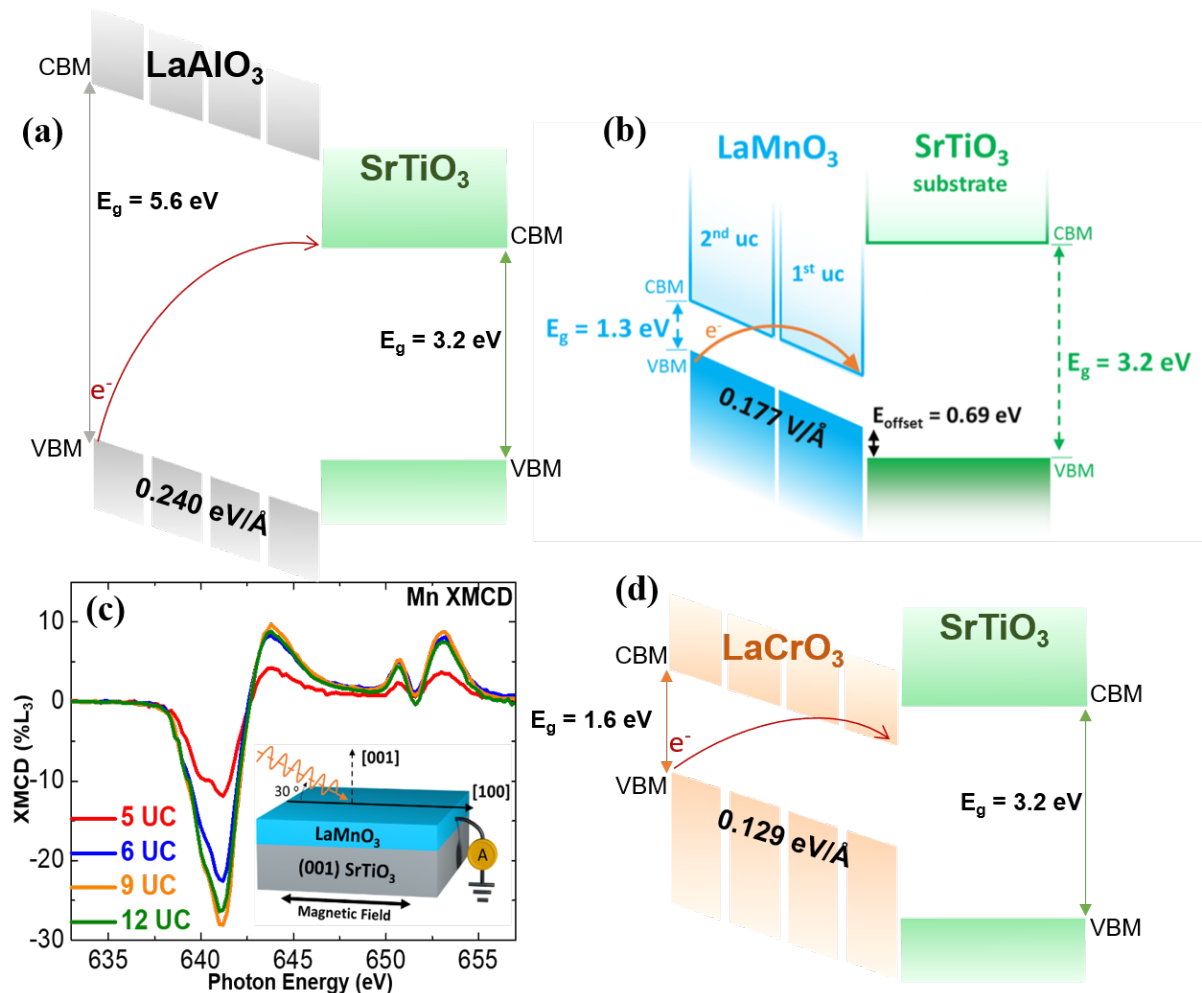


Figure 6.4. (a) Band alignment of the $\text{LaAlO}_3/\text{SrTiO}_3$ heterostructure demonstrates electron accumulation in the SrTiO_3 . Prior work from the group demonstrates (b) an electron accumulation in LaMnO_3 and (c) ferromagnetism by observation of Mn L -edge XMCD of ultra-thin $\text{LaMnO}_3/\text{SrTiO}_3$ heterostructures. (d) $\text{LaCrO}_3/\text{SrTiO}_3$ should have electron accumulation in LaCrO_3 .

have a critical thickness behavior in the range of 2-4 unit cells according to the band alignment of these materials. In the widely-studied case of $\text{LaAlO}_3/\text{SrTiO}_3$, the band alignment favors electron accumulation in SrTiO_3 , which promotes electronic reconstruction leading to a highly conductive interface (Figure 6.4a). In prior work on $\text{LaMnO}_3/\text{SrTiO}_3$, the accumulation of electrons at the interface was found to manifest in the LaMnO_3 , as supported by first-principles density functional theory (Figure 6.4b). This gives rise to ferromagnetism in LaMnO_3 as confirmed by XMCD, previously performed at ALS BL4.0.2 (Figure 6.4c)²⁰⁰. In the $\text{LaCrO}_3/\text{SrTiO}_3$ heterointerface, the critical thickness is

expected to be in the range of 3-4 unit cells based on a built-in potential ranging from 100-500 meV per unit cell estimated from literature values of the electronic structure and work functions²⁰¹. This is warranted by the band alignment of these materials^{203,204}. The band alignment of the $\text{LaCrO}_3/\text{SrTiO}_3$ system is expected to produce an accumulation in the LaCrO_3 (Figure 6.4d), which should be followed up with subsequent first-principles density functional theory.

Future work should perform XMCD studies at a temperature range sweeping from 200 K – 350 K, centered about the Néel temperature of bulk LaCrO_3 . Because the electron accumulation is expected in ultra-thin LaCrO_3 , future work should also probe the lack of change in orbital occupation in the Ti L -edge to ensure that the electron accumulation does not manifest as a change in the titanium oxidation state. Ferromagnetic order at the interface between an antiferromagnet and a diamagnet near room temperature would be impactful for studying the evolution of spin and orbital degrees of freedom in emergent interfacial phenomena.

6.2. Optically tunable exotic ferroic phases

Recent advances have designed thin-film oxide systems with robust emergent phenomena that are sensitive to perturbation via optical excitation. Specifically, the $\text{La}_{0.67}\text{Ca}_{0.33}\text{MnO}_3$ (LCMO) system has been shown to demonstrate an emergent charge-ordered insulating phase that can be optically excited into a metastable metallic phase²⁰⁵. This has been observed in 30 nm LCMO on NdGaO_3 (001) substrates. This work claims to hide the low-temperature metallic ferromagnetic phase normally present in bulk LCMO below 260 K^{206,207} by straining it to NdGaO_3 , which takes on the GdFeO_3 -type orthorhombic structure and therefore imposes anisotropic strain on the LCMO

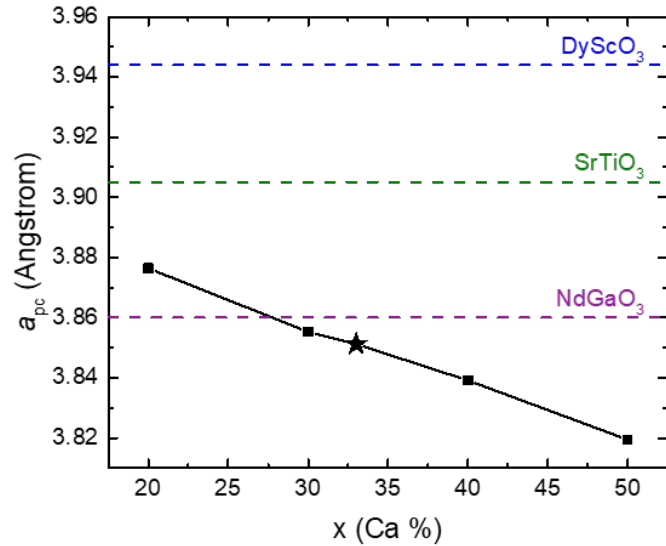


Figure 6.5. The evolution of $\text{La}_{1-x}\text{Ca}_x\text{MnO}_3$ lattice parameter as a function of calcium content. Relevant substrates are shown for reference.

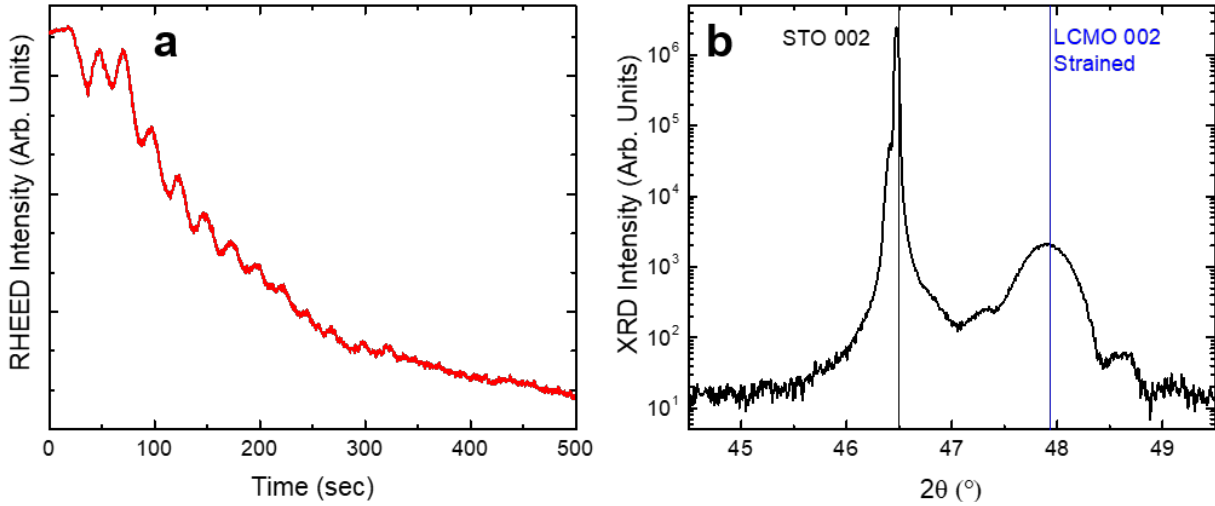


Figure 6.6. (a) Reflection high-energy electron diffraction intensity oscillations during deposition of $\text{La}_{0.67}\text{Mn}_{0.33}\text{O}_3$ on SrTiO_3 (001). (b) θ - 2θ X-ray scans about the 002-condition show excellent epitaxial quality.

film. The resulting phase at low temperatures is an antiferromagnetic insulating phase, leaving the metastable metallic phase accessible via application of a magnetic field. In addition to a magnetic field, the metallic phase is also accessible by optical excitation of Mn^{3+} - Mn^{4+} transitions^{208–211} using 1.55 eV pulses.

In parallel, the electrostatic boundary conditions imposed on ultra-thin ferroelectric layers are incredibly important for ferroic order parameters^{212,213}. An interesting direction to take the light-induced metal-insulator-transition (MIT) in LCMO is to apply it in the scenario of the most well-studied ferroelectric superlattice, $(\text{PbTiO}_3)_n/(\text{SrTiO}_3)_n$. SrTiO_3 typically functions as a dielectric layer, with a large resistance that separates polarization between each polar PbTiO_3 layer. If SrTiO_3 is replaced with LCMO, then the behavior of exotic polar phases such as skyrmions and vortices could be turned on and off or altered by optical excitation.

6.2.1. Next challenges in emergent charge-ordered insulating phase

There are several challenges in overlapping the $(\text{PbTiO}_3)_n/(\text{SrTiO}_3)_n$ and LCMO systems, the first of which is strain. Vortices and skyrmions in $(\text{PbTiO}_3)_n/(\text{SrTiO}_3)_n$ have traditionally been epitaxially grown on SrTiO_3 and DyScO_3 , which have larger lattice parameters than NdGaO_3 (3.905 Å and 3.944 Å, respectively, versus 3.86 Å). The lattice parameter of $\text{La}_{1-x}\text{Ca}_x\text{MnO}_3$ also changes according to the variation in calcium percentage²¹⁴, wherein the lattice parameter steadily drops with increasing calcium (Figure 6.5). Using a fixed composition of $\text{La}_{0.67}\text{Ca}_{0.33}\text{MnO}_3$ (starred, Figure 6.5), strain considerations need to not only consider the difference in magnitude of tensile strain from 0.23% on NdGaO_3 to 1.39% on SrTiO_3 , but also the difference in anisotropy between pseudocubic NdGaO_3 and cubic SrTiO_3 . The goal with LCMO deposition on SrTiO_3 in this regard would be to exhibit the same behavior as LCMO on NdGaO_3 , with a stable antiferromagnetic insulating low-temperature phase. To this end, LCMO thin films were grown on

SrTiO₃ (001) with excellent RHEED intensity oscillations demonstrating persistent layer-by-layer growth mode. Clear oscillations are shown up to 12 unit cells of deposition (Figure 6.6a), with total growth of 20 nm LCMO calculated by the growth rate of the first 12 unit cells. $\omega - 2\theta$ scans demonstrate excellent film quality, with thickness fringes confirming the total film thickness of 20 nm (Figure 6.6b).

Another challenge to note is thickness, wherein LCMO films with thickness below 30 nm becomes more resistive and its ability to effectively perform as a switchable MIT layer diminishes. This is seen in resistivity sweeps to low temperature, both at zero-field and 2 Tesla (Figure 6.7a) for a 20 nm LCMO layer on SrTiO₃. The room temperature resistivity jumps about one order of magnitude in comparison to the 30 nm LCMO on NdGaO₃ reference²⁰⁵, but this could be attributed to a number

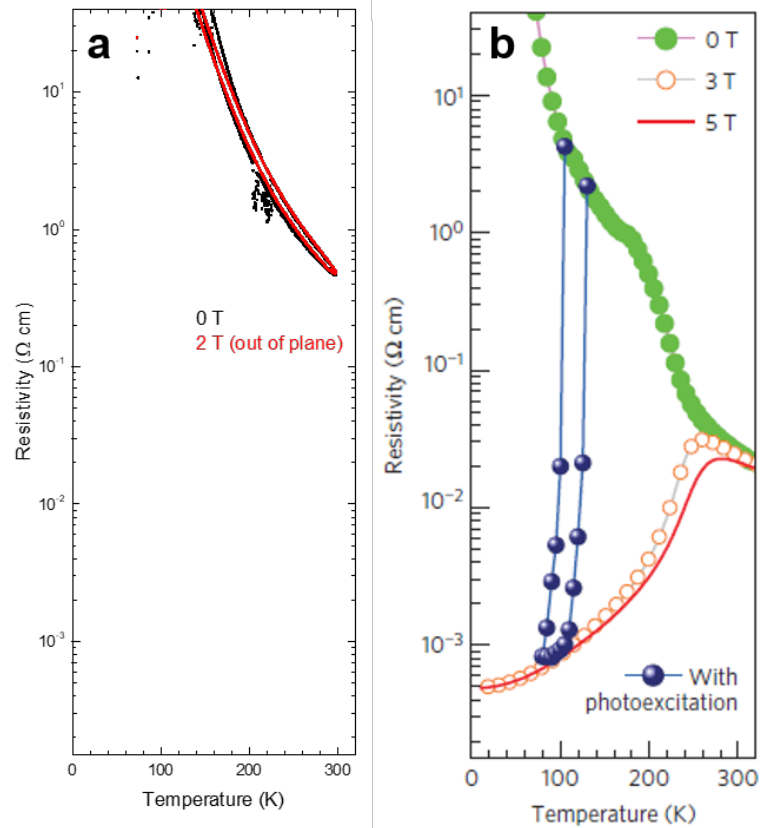


Figure 6.7. Resistivity versus temperature measurements with and without applied magnetic fields of (a) 20 nm LCMO on SrTiO₃ and (b) 30 nm LCMO on NdGaO₃ [Adapted from Zhang 2016].

of factors in the growth conditions, including a fine-tuning of a post-deposition anneal process.

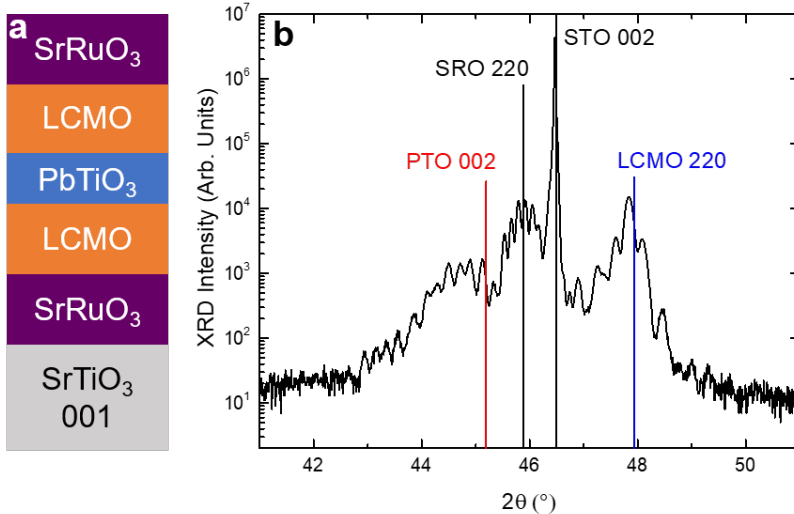


Figure 6.8. (a) Schematic of the SrRuO₃ / La_{0.67}Mn_{0.33}O₃ / PbTiO₃ / La_{0.67}Mn_{0.33}O₃ / SrRuO₃ heterostructure. (b) $\theta - 2\theta$ X-ray scans demonstrate excellent heterostructure growth on SrTiO₃.

With single-layer epitaxial deposition established, more elaborate heterostructures including PbTiO₃ can be explored. Thickness is another challenge in multi-layer heterostructures, wherein PbTiO₃ layers are typically 12-20 unit cells thick (5-8 nm) in vortex and skyrmion structures. This does not easily layer into a superlattice

system including LCMO because that component needs to be 20-30 nm thick to exhibit the optically-induced MIT and the total superlattice thickness would add up quickly, leading to potentially relaxed films. A way to circumvent this issue is to use a single heterostructure stack instead of a superlattice with tens of repeating units. To this end, I synthesized a multi-layer 20 nm SrRuO₃ / 25 nm La_{0.67}Mn_{0.33}O₃ / 6.5 nm PbTiO₃ / 25 nm La_{0.67}Mn_{0.33}O₃ / 20 nm SrRuO₃ symmetric heterostructure (Figure 6.8a), which is particularly useful for analyzing the electronic response of the system within the standard framework of ferroelectric capacitor structures outlined in Chapter 3. This heterostructure exhibits high-quality epitaxy through $\omega - 2\theta$ scans about the 002-diffraction condition (Figure 6.8b). No periodic in-plane structures are detected in reciprocal space maps about the 002-diffraction condition (Figure 6.9a). Peaks at $Q_x \neq 0$ would indicate periodic in-plane order in the PbTiO₃. All layers are epitaxially strained to the substrate as well, confirming excellent film quality (Figure 6.9b).

Beyond structural considerations, LCMO/PbTiO₃ heterostructures are positioned to explore ultrafast control of skyrmion, vortex, and supercrystal phases. More X-ray characterization will be required to study the control of in-plane periodicities in PbTiO₃. These should be integrated with optical pulses in an optical-pump X-ray-probe format, wherein a relationship between optical pulses and exotic ferroelectric phases can be established. This would push the boundary of how electrostatic boundary conditions can be designed to result in tunable and/or novel polar phases. Further efforts such as near-field microscopy and phase-field modeling can help further this effort by providing more insight into the structure-property relationship in this system.

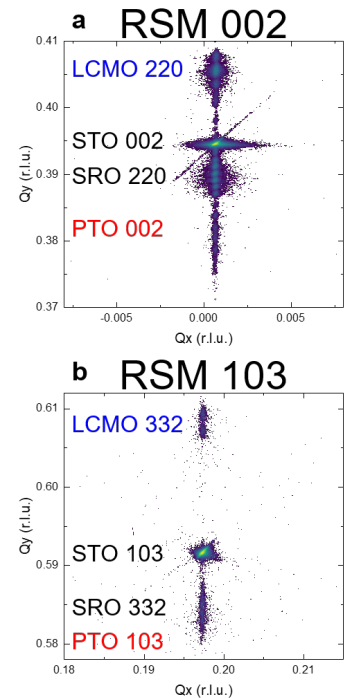


Figure 6.9. Reciprocal space maps of multi-layer heterostructures demonstrate (a) no periodic in-plane features at the 002-diffraction condition and (b) excellent epitaxial quality at the 103-diffraction condition.

Chapter 7

Summary of findings and directions for future work

This Chapter summarizes key findings and features from Chapter 3 to Chapter 6 in the understanding of emergent ferroic behavior in oxide materials. Following that, I suggest directions for future work.

7.1. Summary of findings

1. *RHEED can be used for rapid optimization:* I have demonstrated a pathway for optimizing PLD conditions of STO in a single growth. Persistent RHEED intensity oscillations rise with strontium excess and fall with strontium deficiency. Laser fluence can be tuned *in situ* to fluctuate between rising and falling intensity, with stable intensity at the same level of the substrate (also STO) indicative of stoichiometric deposition. This is particularly useful for tuning the laser in a PLD system after a laser cleaning or optics change. The benefits include time and resources spent in the optimization of high-quality crystal structure, exact stoichiometry, and smooth surfaces of deposited materials. The short study described in **Chapter 3** demonstrates the versatility that RHEED provides in PLD, wherein stoichiometric growth is achieved in a timely and effective manner.
2. *Ferroelectric polarization and dielectric permittivity can be simultaneously enhanced:* Typical ferroelectric materials exhibit either large dielectric susceptibility near a phase boundary or large saturation polarization away from a phase boundary. I achieve both large ferroelectric polarization and dielectric permittivity by building a superlattice heterostructure that simultaneously contains components near a phase boundary (interfaces) and away from a phase boundary (away from interface). The composition of each layer is chosen such that the composition of the MPB is crossed at every interface, wherein phase-boundary behavior stems from repeated interfacial regions in the superlattice structure. Fully-epitaxial $(\text{PbZr}_{0.8}\text{Ti}_{0.2}\text{O}_3)_n / (\text{PbZr}_{0.4}\text{Ti}_{0.6}\text{O}_3)_{2n}$ superlattices with overall film chemistry at the MPB described in **Chapter 4** contain constitutive layers that retain their bulk properties according to the superlattice thickness n (in unit cells). FORC studies reveal separate switching events for each of the parent layers in addition to a phase-boundary-like interfacial layer – with the FORC intensity of the latter increasing as the superlattice period is shortened. This corresponds to the creation of a large volume fraction of phase-boundary-like character at the interfaces in these heterostructures such that one can simultaneously achieve large polarization (enabled by the parent character in those layers) and large permittivity (enabled by the emergent interfacial phase-boundary-like layers). This reveals that deterministic creation of artificial superlattices is an effective pathway for designing materials with enhanced responses to applied bias.

3. *Relaxors can be designed from superlattice heterostructures:* Relaxor-like behavior, which is typically associated with chemical inhomogeneity/complexity in solid solutions, is experimentally and computationally observed in atomically precise $(\text{BaTiO}_3)_n/(\text{SrTiO}_3)_n$ ($n = 4-20$ unit cells) symmetric superlattices in **Chapter 5**. Dielectric studies as a function of temperature reveal frequency dispersion of dielectric response which increases in magnitude as the periodicity decreases. Subsequent Vogel-Fulcher analysis confirms the frequency dispersion of the dielectric maxima across a range of periodicities and the presence of relaxor-like behavior which becomes more robust at shorter periods. BVMD simulations suggest that the relaxor-like behavior observed experimentally in the shorter-period superlattices ($n = 4$) arises from temperature-driven size variations of antipolar stripe domains in contrast to the more thermally stable dipolar configurations in the longer-period superlattices ($n = 6$ and $n = 16$). 2D discrete wavelet transforms, used to quantify spatial and temporal dipolar correlations, reveal that the phenomenological VF freezing temperature marks the transition between a relaxor-like phase and one with diagonal antipolar domains. Moreover, the size and shape of the antipolar domains are tuned by superlattice periodicity following Kittel's Law thus providing an artificial route to relaxor-like behavior which may expand the ability to control desired properties in these complex systems.
4. *The dielectric permittivity of ultra-thin superlattice layers depends on the periodicity:* In the atomically precise superlattice systems focused on in this work, the repeating unit of a superlattice heavily dictates the permittivity. In the case of $(\text{PbZr}_{0.8}\text{Ti}_{0.2}\text{O}_3)_n/(\text{PbZr}_{0.4}\text{Ti}_{0.6}\text{O}_3)_{2n}$ superlattices, this can be attributed to the amount of interfaces that behave like a phase boundary. While these structures exhibit uniformly large polarization, there is a significant superlattice-periodicity-dependent evolution of the dielectric permittivity and switching behavior according to the number of interfaces and therefore the amount of phase-boundary behavior. In the case of $(\text{BaTiO}_3)_n/(\text{SrTiO}_3)_n$ superlattices, both dielectric permittivity and tunability can be enhanced by tuning the superlattice periodicity down to shorter periods. In this case, temperature-driven size variations of antipolar stripe domains in short-period superlattices lead to strong relaxor-like behavior in contrast to more thermally stable dipolar configurations in the longer-period superlattices.

7.2. Directions for future work

This section covers a handful of directions for future efforts, primarily focused on destabilizing ferroelectric phases to explore novel phases and enhanced properties by using the extra degrees of freedom enabled by superlattice design criteria.

7.2.1. Tri-component superlattices

The superlattice systems in this work are almost exclusively two-component systems (not including electrode layers). One design parameter that can be expanded on is the number of components in the system. The next obvious step is a tri-component system. Tri-layer superlattices have previously explored, typically with the goal of enhancing dielectric response and polarization

through the breaking of inversion symmetry^{87,145,215–220}. One notable advance in this effort is the tri-color BaTiO₃/SrTiO₃/LaTiO₃ superlattice²²¹, wherein unequal interfaces give rise to coexisting polar structure and metallicity.

To expand on the current work on superlattices in the PbZr_{1-x}Ti_xO₃ system, future efforts could employ a tri-component superlattice. Given the importance of the MPB in this system, a logical third component to weave into this system would be the MPB composition, PbZr_{0.52}Ti_{0.48}O₃. Thus, a tri-component superlattice with PbZr_{0.8}Ti_{0.2}O₃/PbZr_{0.52}Ti_{0.48}O₃/PbZr_{0.4}Ti_{0.6}O₃ layers could directly modulate phase boundary behavior by containing entire phase boundary layers. The limit of this would be PbZr_{0.52}Ti_{0.48}O₃ layers with zero thickness, which would be the current work. Thus, this effort would inherently include more phase boundary behavior and likely maintain large dielectric susceptibility. The inclusion of PbZr_{0.52}Ti_{0.48}O₃ layers could bring about interesting observations in switching, wherein the monoclinic phase could assist in bringing down the energy required to switch via multiple polarization rotations. This might be akin to previous work on successive switching events in (111)-oriented PbZr_{0.2}Ti_{0.8}O₃ films²²².

Tri-component systems could also be employed in PbTiO₃/SrTiO₃ system, wherein an intermediate composition in the Pb_{1-x}Sr_xTiO₃ could be introduced between each PbTiO₃ and SrTiO₃ layer to reduce the contribution of polarization gradient energy in system. This sort of intermediate composition could lead to larger and less stable polar vortex and skyrmion structures, wherein smaller electric fields could elicit a larger dielectric response. When pushed to longer periodicities, these exotic phases could lose their in-plane polar order and exhibit more random polar order akin to that of relaxor ferroelectrics.

Instead of adding an intermediate composition to an existing two-component system, the third component can be something entirely different. For example, future research efforts can focus on PbTiO₃/SrTiO₃/La_{0.67}Ca_{0.33}MnO₃ superlattices²⁰⁵, wherein the exotic polar phases can be turned on and off by optical pulses (**Chapter 6**). The same functionality could be observed without the dielectric SrTiO₃ layer, but that would need to be explored. Additional consideration needs to be taken with a dissimilar third component in growing the material as well, wherein overlapping PLD growth conditions would become increasingly cumbersome to achieve even in oxide thin films.

7.2.2. Superlattice asymmetry

The bulk of the current work utilizes superlattice periodicity as the main tool to destabilize ferroelectric phases, with a small degree of effort dedicated to tuning MPB behavior via superlattice asymmetry (**Chapter 4**). In asymmetric superlattices, uneven chemical compositions and length scales present opportunities to precisely tackle ultra-thin ferroelectric order for studying screening lengths, polarization rotations, etc^{140,215}. Superlattices with asymmetric types of interfaces such as metal-ferroelectric interfaces^{15,223–227} also present fertile pathways to studying the evolution of ferroic order parameters in ultra-thin layers.

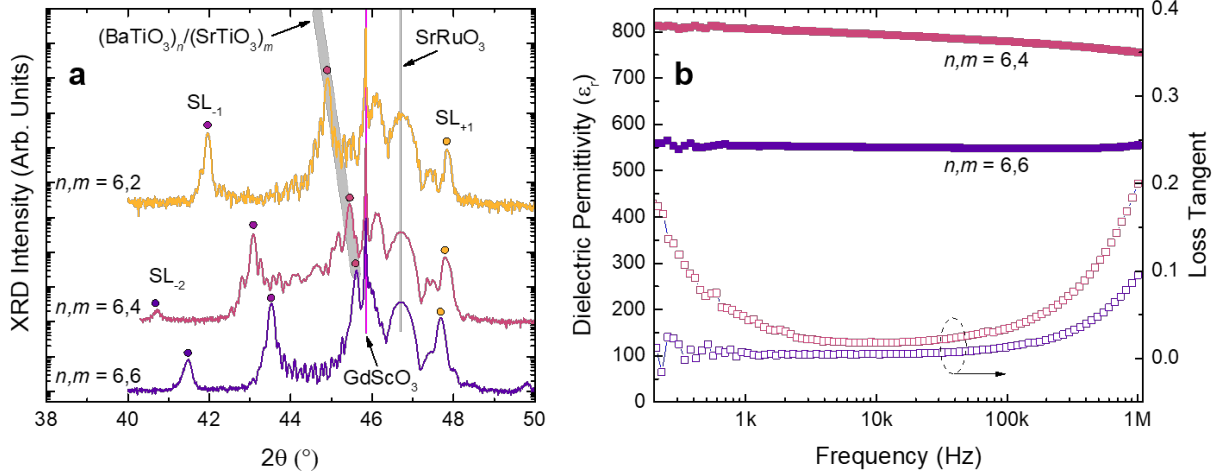


Figure 7.1. (a) X-ray diffraction about the 002-diffraction condition demonstrating high-quality epitaxial (00l)-oriented $(BaTiO_3)_n/(SrTiO_3)_m$ superlattices on 20 nm $SrRuO_3/GdScO_3$ (110) with thickness and superlattices fringes. (b) Dielectric permittivity and loss for $n,m = 6,4$ and $6,6$, with larger permittivity in the shorter periodicity.

One such study that could be further explored is superlattice asymmetry in $(BaTiO_3)_n/(SrTiO_3)_m$, wherein previous work has reported enhanced out-of-plane polarization in phase-field simulations on $SrTiO_3$ substrates¹⁴¹. There are opportunities to explore the evolution of ferroelectric order in this system on a more moderate substrate between the two parent components, wherein I have done some preliminary measurements. I designed and deposited $(BaTiO_3)_n/(SrTiO_3)_m$ with $n = 6$ and $m = 6, 4, 2$ on $GdScO_3$ (110) substrates to study how relaxor behavior evolves beyond periodicity (**Chapter 5**). θ - 2θ scans about the 002-diffraction condition reveal high-quality epitaxial superlattices with an expanding main $SL_{(0)}$ peak with increased asymmetry (more $BaTiO_3$). This expansion is consistent with a larger percentage of the larger component, $BaTiO_3$ (Figure 7.1a). The dielectric response of the asymmetric $n,m = 6,4$ superlattice indicates an enhanced permittivity (Figure 7.1b), but caution should be taken in further studies, as Maxwell-Wagner polarization could be the cause of enhanced dielectric response in this asymmetric film due to enhanced low-frequency loss (**Chapter 2**). Future work in asymmetric superlattices in this system could go to study the evolution of relaxor behavior in fitting temperature-dependent frequency dispersion to the VF relation^{30,32,33}. Another avenue in this system would be to probe asymmetry in the other direction, wherein more $SrTiO_3$ in the system would further destabilize polar domains in the $BaTiO_3$. A larger fraction of the dielectric component could also be pursued in $(PbTiO_3)_n/(SrTiO_3)_n$ superlattices, with a likely similar effect of destabilizing polar vortices or skyrmions by increased $SrTiO_3$ layer thicknesses.

7.2.3. Strain control and measurement direction

Another straightforward direction for future work is to take standard ferroelectric systems like those in the current work and probe how they behave in superlattices under various other strain conditions. Strain is known to be one of the larger factors in the energy landscape, so tuning the elastic energy of a superlattice is incredibly important^{55,228,229}. To this end, I have designed and realized some preliminary structures. I explored the evolution of relaxor behavior in

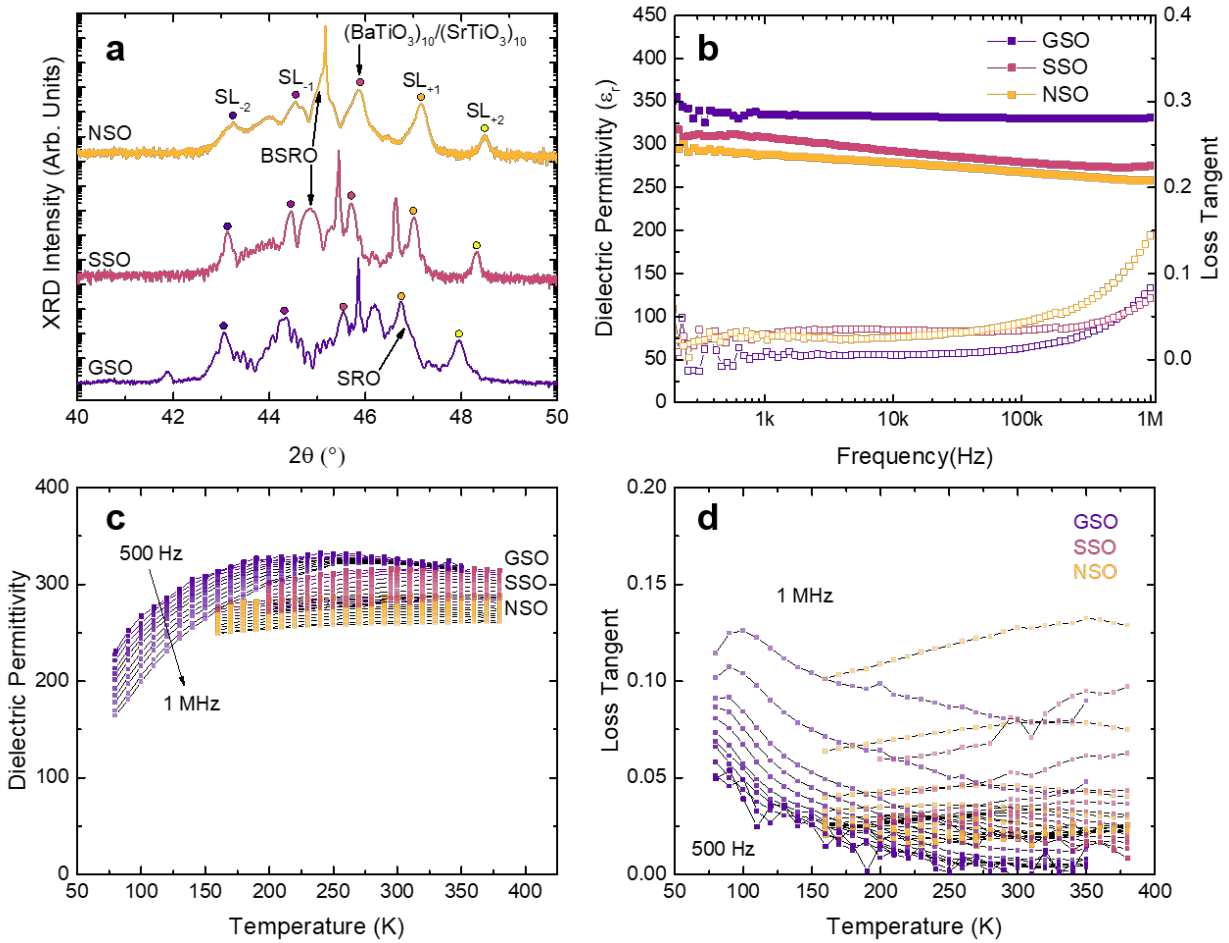


Figure 7.2. (a) X-ray diffraction about the 002-diffraction condition demonstrating high-quality epitaxial (001)-oriented $(\text{BaTiO}_3)_{10}/(\text{SrTiO}_3)_{10}$ superlattices on NdScO_3 , SmScO_3 , and GdScO_3 (110) substrates with thickness and superlattices fringes. (b) Dielectric permittivity trending upward with decreasing substrate size, with corresponding loss tangents. (c) Frequency- and temperature-dependent dielectric permittivity from 500 Hz to 1 MHz and (d) corresponding loss tangents.

$(\text{BaTiO}_3)_{10}/(\text{SrTiO}_3)_{10}$ superlattices with larger substrates SmScO_3 and NdScO_3 in addition to the structures on GdScO_3 (110) in **Chapter 5**. Structures on SmScO_3 and NdScO_3 (110) substrates were grown on 20 nm $\text{Ba}_{0.5}\text{Sr}_{0.5}\text{RuO}_3$ (BSRO) instead of SrRuO_3 (SRO) due to its favorably smaller lattice mismatch with the larger substrates. θ - 2θ scans about the 002-diffraction condition confirm strong superlattice peaks for all films, indicative of excellent layer control in the deposition process (Figure 7.2a). Dielectric response as a function of frequency at room temperature demonstrates larger permittivity with smaller substrates and no sign of Maxwell-Wagner polarization (Figure 7.2b). Temperature- and frequency-dependent dielectric permittivity (Figure 7.2c) and loss (Figure 7.2d) show broad temperature dependence for the larger substrates. For the structure on GdScO_3 , permittivity falls and loss rises at temperatures below 100 K with some frequency dispersion, indicative of a relaxor transition (**Chapter 5**). For the structures on the two larger substrates, flat response dominates a large temperature window (150 K – 350 K). Future work in this regard should consider in-plane physical properties measurements, wherein larger substrates should lead to larger percentages of in-plane polarization. In-plane dielectric

permittivity measurements of superlattices structures should add the capacitance of each layer in parallel instead of in series, given that electric fields would be directed in the plane of the film.

References

1. Cross, L. E. & Newnham, R. E. *History of Ferroelectrics*. **III**, (The American Chemical Society, 1987).
2. Newnham, R. *Properties of Materials- Anisotropy, Symmetry, Structure*. (Oxford University Press, 2005).
3. Bader, R. F. W. An interpretation of potential interaction constants in terms of low-lying excited states. *Mol. Phys.* **3**, 137–151 (1960).
4. H.A. Jahn and E. Teller. Stability of Polyatomic Molecules in Degenerate Electronic States I-Orbital Degeneracy. *Proc. R. Soc. London* **161**, 220–235 (1937).
5. Opik, U. & Pryce, M. H. L. Studies of the Jahn-Teller effect I. A survey of the static problem. *Proc. R. Soc. A* **238**, 425 (1957).
6. Ronald E. Cohen. Origin of ferroelectricity in perovskite oxides. *Nature* **358**, 136–138 (1992).
7. Halasyamani, P. S. & Poepelmeier, K. R. Noncentrosymmetric Oxides. *Chem. Mater.* **10**, 2753–2769 (1998).
8. Lines, M. E. & Glass, A. M. *Principles and Applications of Ferroelectrics and Related Materials*. (Oxford University Press, 2001).
9. Zhong, W., Vanderbilt, D. & Rabe, K. M. First-principles theory of ferroelectric phase transitions for perovskites: The case of BaTiO₃. *Phys. Rev. B* **52**, 6301–6312 (1995).
10. Bassiri-Gharb, N. *et al.* Domain wall contributions to the properties of piezoelectric thin films. *J. Electroceramics* **19**, 47–65 (2007).
11. Schlom, D. G. *et al.* Strain Tuning of Ferroelectric Thin Films. *Annu. Rev. Mater. Res* **37**, 589–626 (2007).
12. Haeni, J. H. *et al.* Room-temperature ferroelectricity in strained SrTiO₃. *Nature* **430**, 758–761 (2004).
13. Choi, K. J. *et al.* Enhancement of Ferroelectricity in Strained BaTiO₃ Thin Films. *Science* **306**, 1005–1009 (2004).
14. He, B. & Wang, Z. Enhancement of the Electrical Properties in BaTiO₃/PbZr_{0.52}Ti_{0.48}O₃ Ferroelectric Superlattices. *ACS Appl. Mater. Interfaces* **8**, 6736–6742 (2016).
15. Hadjimichael, M., Li, Y., Yedra, L., Dkhil, B. & Zubko, P. Domain structure and dielectric properties of metal-ferroelectric superlattices with asymmetric interfaces. *Phys. Rev. Mater.* **4**, 1–10 (2020).
16. Junquera, J. & Ghosez, P. Critical thickness for ferroelectricity in perovskite ultrathin films. *Nature* **422**, 506–509 (2003).
17. Nagaraj, B., Aggarwal, S. & Ramesh, R. Influence of contact electrodes on leakage characteristics in ferroelectric thin films. *J. Appl. Phys.* **90**, 375–382 (2001).
18. Glinchuk, M. D., Zaulychny, B. Y. & Stephanovich, V. A. Depolarization field in thin ferroelectric films with account of semiconductor electrodes. *Ferroelectrics* **316**, 1–6 (2005).
19. Hartmann, A. J., Neilson, M., Lamb, R. N., Watanabe, K. & Scott, J. F. Ruthenium oxide and strontium ruthenate electrodes for ferroelectric thin-film capacitors. *Appl. Phys. A Mater. Sci. Process.* **70**, 239–242 (2000).
20. Janovec, V. On the theory of the coercive field of single-domain crystals of BaTiO₃. *Czechoslov. J. Phys.* **8**, 3–15 (1958).
21. Kay, H. F. & Dunn, J. W. Thickness dependence of the nucleation field of triglycine

- sulphate. *Philos. Mag.* **7**, 2027–2034 (1962).
22. Chandra, P., Dawber, M., Littlewood, P. B. & Scott, J. F. Scaling of the coercive field with thickness in thin-film ferroelectrics. *Ferroelectrics* **313**, 7–13 (2004).
 23. Dawber, M., Chandra, P., Littlewood, P. B. & Scott, J. F. Depolarization corrections to the coercive field in thin-film ferroelectrics. *J. Phys. Condens. Matter* **15**, (2003).
 24. Spaldin, N. A. Fundamental Size Limits in Ferroelectricity. *Science* **304**, 1606–1608 (2004).
 25. Fong, D. D. *et al.* Ferroelectricity in ultrathin perovskite films. *Science* **304**, 1650–1653 (2004).
 26. Park, S. E. & Shrout, T. R. Ultrahigh strain and piezoelectric behavior in relaxor based ferroelectric single crystals. *J. Appl. Phys.* **82**, 1804–1811 (1997).
 27. Pandya, S. *et al.* Pyroelectric energy conversion with large energy and power density in relaxor ferroelectric thin films. *Nat. Mater.* **17**, 432–438 (2018).
 28. Jiang, Y. *et al.* Ferroelectric polymers and their nanocomposites for dielectric energy storage applications. *APL Mater.* **9**, (2021).
 29. Cross, L. E. Relaxor ferroelectrics: an overview. *Ferroelectrics* **151**, 305–320 (1994).
 30. Viehland, D., Jang, S. J., Cross, L. E. & Wuttig, M. Freezing of the polarization fluctuations in lead magnesium niobate relaxors. *J. Appl. Phys.* **68**, 2916–2921 (1990).
 31. Viehland, D., Wuttig, M. & Cross, L. E. The glassy behavior of relaxor ferroelectrics. *Ferroelectrics* **120**, 71–77 (1991).
 32. Huang, Y. *et al.* Domain freezing in potassium dihydrogen phosphate, triglycine sulfate, and CuAlZnNi. *Phys. Rev. B* **55**, 16159–16167 (1997).
 33. Bahri, F. *et al.* Dielectric and Raman studies on the solid solution $(1 - x)\text{BaTiO}_3/x\text{NaNbO}_3$ ceramics. *Solid State Sci.* **5**, 1445–1450 (2003).
 34. Hlinka, J. Do we need the ether of polar nanoregions? *J. Adv. Dielectr.* **2**, 1241006 (2012).
 35. Burns, G. Crystalline Ferroelectrics with a Glassy Polarization Phase. *Phase Transitions* **5**, 261–275 (1985).
 36. Dkhil, B. *et al.* Intermediate temperature scale T^* in lead-based relaxor systems. *Phys. Rev. B* **80**, 1–6 (2009).
 37. Kim, J. *et al.* Epitaxial Strain Control of Relaxor Ferroelectric Phase Evolution. *Adv. Mater.* **31**, 1901060 (2019).
 38. Takenaka, H., Grinberg, I., Liu, S. & Rappe, A. M. Slush-like polar structures in single-crystal relaxors. *Nature* **546**, 391–395 (2017).
 39. Matsuura, M. *et al.* Composition dependence of the diffuse scattering in the relaxor ferroelectric compound $(1-x)\text{Pb}(\text{Mg}_{1/3}\text{Nb}_{2/3})\text{O}_3 - x\text{PbTiO}_3$ ($0 \leq x \leq 0.40$). *Phys. Rev. B* **74**, 1–10 (2006).
 40. Fernandez, A., Kim, J., Meyers, D., Saremi, S. & Martin, L. W. Finite-size effects in lead scandium tantalate relaxor thin films. *Phys. Rev. B* **101**, 1–8 (2020).
 41. Krogstad, M. J. *et al.* The relation of local order to material properties in relaxor ferroelectrics. *Nat. Mater.* **17**, 718–724 (2018).
 42. Ruddlesden, S. N. & Popper, P. New compounds of the K_2Nf_4 type. *Acta Crystallogr.* **10**, 538–539 (1957).
 43. Nakhmanson, S. M. Revealing latent structural instabilities in perovskite ferroelectrics by layering and epitaxial strain: A first-principles study of Ruddlesden-Popper superlattices. *Phys. Rev. B* **78**, 1–5 (2008).
 44. Perez-Mato, J. M. *et al.* Competing structural instabilities in the ferroelectric Aurivillius compound $\text{SrBi}_2\text{Ta}_2\text{O}_9$. *Phys. Rev. B* **70**, 1–14 (2004).

45. Scott, J. F., Ross, F. M., Paz De Araujo, C. A., Scott, M. C. & Huffman, M. Structure and device characteristics of SrBi₂Ta₂O₉-based nonvolatile random-access memories. *MRS Bull.* **21**, 33–39 (1996).
46. Bein, B. *et al.* In situ X-ray diffraction and the evolution of polarization during the growth of ferroelectric superlattices. *Nat. Commun.* **6**, 10136 (2015).
47. Tabata, H., Tanaka, H. & Kawai, T. Formation of artificial BaTiO₃ / SrTiO₃ superlattices using pulsed laser deposition and their dielectric properties Formation of artificial BaTiO₃ / SrTiO₃ superlattices using pulsed laser deposition and their dielectric properties. *Appl. Phys. Lett.* **65**, 1970 (1994).
48. Shimuta, T. *et al.* Enhancement of remanent polarization in epitaxial BaTiO₃/SrTiO₃ superlattices with ‘asymmetric’ structure. *J. Appl. Phys.* **91**, 2290–2294 (2002).
49. O’Neill, D., Bowman, R. M. & Gregg, J. M. Dielectric enhancement and Maxwell-Wagner effects in ferroelectric superlattice structures. *Appl. Phys. Lett.* **77**, 1520–1522 (2000).
50. Wang, C. C., Lu, H. B., Jin, K. J. & Yang, G. Z. Temperature-dependent dielectric strength of a Maxwell-Wagner type relaxation. *Mod. Phys. Lett. B* **22**, 1297–1305 (2008).
51. Shen, M., Ge, S. & Cao, W. Dielectric enhancement and Maxwell-Wagner effects in polycrystalline ferroelectric multilayered thin films. *J. Phys. D: Appl. Phys.* **34**, 2935–2938 (2001).
52. Catalan, G., O’Neill, D., Bowman, R. M. & Gregg, J. M. Relaxor features in ferroelectric superlattices: A Maxwell-Wagner approach. *Appl. Phys. Lett.* **77**, 3078–3080 (2000).
53. Neumann, H. & Arlt, G. Maxwell-wagner relaxation and degradation of SrTiO₃ and BaTiO₃ ceramics. *Ferroelectrics* **69**, 179–186 (1986).
54. Arlt, G. The Influence Of Microstructure On The Properties Of Ferroelectric Ceramics. *Ferroelectrics* **104**, 217–227 (1990).
55. Nambu, S. & Sagala, D. A. Domain formation and elastic long-range interaction in ferroelectric perovskites. *Phys. Rev. B* **50**, 5838–5847 (1994).
56. Semenovskaya, S. & Khachatryan, A. G. Development of ferroelectric mixed states in a random field of static defects. *J. Appl. Phys.* **83**, 5125–5136 (1998).
57. Li, Y. L., Hu, S. Y., Liu, Z. K. & Chen, L. Q. Effect of substrate constraint on the stability and evolution of ferroelectric domain structures in thin films. *Acta Mater.* **50**, 395–411 (2002).
58. Speck, J. S., Daykin, A. C., Seifert, A., Romanov, A. E. & Pompe, W. Domain configurations due to multiple misfit relaxation mechanisms in epitaxial ferroelectric thin films. III. Interfacial defects and domain misorientations. *J. Appl. Phys.* **78**, 1696–1706 (1995).
59. Alpay, S. P. & Roytburd, A. L. Thermodynamics of polydomain heterostructures. III. Domain stability map. *J. Appl. Phys.* **83**, 4714–4723 (1998).
60. Pertsev, N. A. & Koukhar, V. G. Polarization instability in polydomain ferroelectric epitaxial thin films and the formation of heterophase structures. *Phys. Rev. Lett.* **84**, 3722–3725 (2000).
61. Koukhar, V. G., Pertsev, N. A. & Waser, R. In-plane polarization states and their instabilities in polydomain epitaxial ferroelectric thin films. *Appl. Phys. Lett.* **78**, 530–532 (2001).
62. Li, Y. L., Hu, S. Y., Liu, Z. K. & Chen, L. Q. Effect of electrical boundary conditions on ferroelectric domain structures in thin films. *Appl. Phys. Lett.* **81**, 427–429 (2002).
63. Strukov, B. A. & Levanyuk, A. P. *Ferroelectric Phenomena in Crystals. Ferroelectric*

- Phenomena in Crystals* (Springer, 1998). doi:10.1007/978-3-642-60293-1
64. Bousquet, E. *et al.* Improper ferroelectricity in perovskite oxide artificial superlattices. *Nature* **452**, 732–736 (2008).
 65. Tang, Y. L. *et al.* Observation of a periodic array of flux-closure quadrants in strained ferroelectric PbTiO₃ films. *Science* **348**, 547 (2015).
 66. Yadav, A. K. *et al.* Observation of polar vortices in oxide superlattices. *Nature* **530**, 198–201 (2016).
 67. Damodaran, A. R. *et al.* Phase coexistence and electric-field control of toroidal order in oxide superlattices. *Nat. Mater.* **16**, 1003–1009 (2017).
 68. Shafer, P. *et al.* Emergent chirality in the electric polarization texture of titanate superlattices. *Proc. Natl. Acad. Sci. U. S. A.* **115**, 915–920 (2018).
 69. Das, S. *et al.* Observation of room-temperature polar skyrmions. *Nature* **568**, 368–372 (2019).
 70. Levanyuk, A. P. & Sannikov, D. G. Improper ferroelectrics. *Sov. Phys. Uspekhi* **17**, 199 (1974).
 71. Hong, Z. *et al.* Stability of Polar Vortex Lattice in Ferroelectric Superlattices. *Nano Lett.* **17**, 2246–2252 (2017).
 72. Das, S. *et al.* Local negative permittivity and topological phase transition in polar skyrmions. *Nat. Mater.* (2020). doi:10.1038/s41563-020-00818-y
 73. Tomasello, R. *et al.* A strategy for the design of skyrmion racetrack memories. *Sci. Rep.* **4**, 1–7 (2014).
 74. Stuart S. P. Parkin, Hayashi, M. & Thomas, L. Magnetic Domain-Wall Racetrack Memory. *Science* **320**, 190 (2008).
 75. Yadav, A. K. *et al.* Spatially resolved steady-state negative capacitance. *Nature* **565**, 468–471 (2019).
 76. Zubko, P. *et al.* Negative capacitance in multidomain ferroelectric superlattices. *Nature* **534**, 524–528 (2016).
 77. Hoffmann, M. *et al.* Unveiling the double-well energy landscape in a ferroelectric layer. *Nature* **565**, 464–467 (2019).
 78. Sherman, A. *Chemical Vapor Deposition for Microelectronics: Principles, Technology, and Applications.* **19**, 215 (1987).
 79. Mahan, J. E. *Physical vapor deposition of thin films.* (Wiley, 2000).
 80. Martin, L. W., Chu, Y. H. & Ramesh, R. Advances in the growth and characterization of magnetic, ferroelectric, and multiferroic oxide thin films. *Mater. Sci. Eng. R Reports* **68**, 89–133 (2010).
 81. Martin, L. W. & Schlom, D. G. Advanced synthesis techniques and routes to new single-phase multiferroics. *Curr. Opin. Solid State Mater. Sci.* **16**, 199–215 (2012).
 82. Moyer, J. A., Gao, R., Schiffer, P. & Martin, L. W. Epitaxial growth of highly-crystalline spinel ferrite thin films on perovskite substrates for all-oxide devices. *Sci. Rep.* **5**, 10363 (2015).
 83. Zhang, H. T., Dedon, L. R., Martin, L. W. & Engel-Herbert, R. Self-regulated growth of LaVO₃ thin films by hybrid molecular beam epitaxy. *Appl. Phys. Lett.* **106**, (2015).
 84. Breckenfeld, E. *et al.* Effect of growth induced (non)stoichiometry on interfacial conductance in LaAlO₃/SrTiO₃. *Phys. Rev. Lett.* **110**, 196804 (2013).
 85. Breckenfeld, E., Bronn, N., Mason, N. & Martin, L. W. Tunability of conduction at the LaAlO₃/SrTiO₃ heterointerface: Thickness and compositional studies. *Appl. Phys. Lett.*

- 105, (2014).
86. Lee, S. *et al.* A novel, layered phase in Ti-Rich SrTiO₃ epitaxial thin films. *Adv. Mater.* **27**, 861–868 (2015).
 87. Eckstein, J. N. & Bozovic, I. HETEROSTRUCTURES GROWN BY ATOMIC LAYER-BY-LAYER molecular beam epitaxy. *Annu. Rev. Mater. Sci.* **25**, 679–709 (1995).
 88. Chambers, S. A. Epitaxial growth and properties of thin film oxides. *Surf. Sci. Rep.* **39**, 105–180 (2000).
 89. Chambers, S. A. Epitaxial growth and properties of doped transition metal and complex oxide films. *Adv. Mater.* **22**, 219–248 (2010).
 90. Christen, H. M., Silliman, S. D. & Harshavardhan, K. S. Continuous compositional-spread technique based on pulsed-laser deposition and applied to the growth of epitaxial films. *Rev. Sci. Instrum.* **72**, 2673–2678 (2001).
 91. Christen, H. M. *et al.* An improved continuous compositional-spread technique based on pulsed-laser deposition and applicable to large substrate areas. *Rev. Sci. Instrum.* **74**, 4058–4062 (2003).
 92. Ohkubo, I. *et al.* High-throughput growth temperature optimization of ferroelectric Sr xBa 1-xNb 2O 6 epitaxial thin films using a temperature gradient method. *Appl. Phys. Lett.* **84**, 1350–1352 (2004).
 93. Christen, H. M. *et al.* Dielectric and optical properties of epitaxial rare-earth scandate films and their crystallization behavior. *Appl. Phys. Lett.* **88**, 1–4 (2006).
 94. Sambri, A. *et al.* Effects of oxygen background pressure on the stoichiometry of a LaGaO₃ laser ablation plume investigated by time and spectrally resolved two-dimensional imaging. *J. Appl. Phys.* **119**, (2016).
 95. Smith, D. L. *Thin-film Deposition: Principles and Practice.* (McGraw-Hill, 1995).
 96. Chrisey, D. B. & Hubler, G. K. *Pulsed Laser Deposition of Thin Films.* (John Wiley & Sons, 1994).
 97. Eason, R. *Pulsed Laser Deposition of Thin Films.* (John Wiley & Sons, 2007).
 98. Ashfold, M. N. R., Claeysens, F., Fuge, G. M. & Henley, S. J. Pulsed laser ablation and deposition of thin films Michael. *Chem. Soc. Rev.* **33**, 23 (2004).
 99. Prentice, J. J., Grant-Jacob, J. A., Kurilchik, S. V., Mackenzie, J. I. & Eason, R. W. Particulate reduction in PLD-grown crystalline films via bi-directional target irradiation. *Appl. Phys. A Mater. Sci. Process.* **125**, 1–8 (2019).
 100. Brune, H. Epitaxial growth of thin films of perylene. in *Surface and Interface Science* **66**, 421 (Wiley-VCH Verlag GmbH & Co. KGaA, 2014).
 101. Hong, W. *et al.* Persistent step-flow growth of strained films on vicinal substrates. *Phys. Rev. Lett.* **95**, 1–4 (2005).
 102. Ohring, M. *Materials Science of Thin Films.* (Academic Press, 2002).
 103. Ohashi, S. *et al.* Compact laser molecular beam epitaxy system using laser heating of substrate for oxide film growth. *Rev. Sci. Instrum.* **70**, 178–183 (1999).
 104. Chen, P., Xu, S. Y., Lin, J., Ong, C. K. & Cui, D. F. Angle-resolved X-ray photoelectron spectroscopy of topmost surface for LaNiO₃ thin film grown on SrTiO₃ substrate by laser molecular beam epitaxy. *Appl. Surf. Sci.* **137**, 98–102 (1999).
 105. Yang, G. Z., Lu, H. B., Chen, F., Zhao, T. & Chen, Z. H. Laser molecular beam epitaxy and characterization of perovskite oxide thin films. *J. Cryst. Growth* **227–228**, 929–935 (2001).
 106. Rijnders, G. J. H. M., Koster, G., Blank, D. H. A. & Rogalla, H. In situ monitoring during pulsed laser deposition of complex oxides using reflection high energy electron diffraction

- under high oxygen pressure. *Appl. Phys. Lett.* **70**, 1888–1890 (1997).
107. Shitara, T. *et al.* Morphological model of reflection high-energy electron-diffraction intensity oscillations during epitaxial growth on GaAs(001). *Appl. Phys. Lett.* **60**, 1504–1506 (1992).
 108. Rijnders, G., Blank, D. H. A., Auciello, O. & Ramesh, R. *Thin Films and Heterostructures of Oxide Electronics*. (Springer Science, 2005).
 109. Huijben, M. *et al.* Critical thickness and orbital ordering in ultrathin La_{0.7} Sr_{0.3} MnO₃ films. *Phys. Rev. B* **78**, 1–7 (2008).
 110. Kawasaki, M. *et al.* Atomic Control of the SrTiO₃ Crystal Surface. *Science* **266**, 1540–1542 (1994).
 111. Zhang, T. W., Mao, Z. W., Gu, Z. B., Nie, Y. F. & Pan, X. Q. An efficient and reliable growth method for epitaxial complex oxide films by molecular beam epitaxy. *Appl. Phys. Lett.* **111**, 011601 (2017).
 112. Sullivan, M. C. *et al.* Complex oxide growth using simultaneous in situ reflection high-energy electron diffraction and x-ray reflectivity: When is one layer complete? *Appl. Phys. Lett.* **106**, 031604 (2015).
 113. Sun, H. Y. *et al.* Chemically specific termination control of oxide interfaces via layer-by-layer mean inner potential engineering. *Nat. Commun.* **9**, (2018).
 114. Eom, C. B. *et al.* Fabrication and properties of epitaxial ferroelectric heterostructures with (SrRuO₃) isotropic metallic oxide electrodes. *Appl. Phys. Lett.* **63**, 2570–2572 (1993).
 115. Morimoto, T. *et al.* Ferroelectric Properties of Pb (Zi , Ti) O 3 Capacitor with Thin SrRuO 3 Films within Both Electrodes. *Japanese J. Appl. Phys* **39**, 2110 (2000).
 116. Tagantsev, A. K., Stolichnov, I., Colla, E. L. & Setter, N. Polarization fatigue in ferroelectric films: Basic experimental findings, phenomenological scenarios, and microscopic features. *J. Appl. Phys.* **90**, 1387–1402 (2001).
 117. Kim, Y. S. *et al.* Ferroelectric properties of SrRu O₃ BaTi O₃ SrRu O₃ ultrathin film capacitors free from passive layers. *Appl. Phys. Lett.* **88**, (2006).
 118. Bragg, W. H. & Bragg, W. L. The reflection of X-rays by crystals. *Proc. R. Soc. A* **17**, 43 (1913).
 119. Birkholz, M. *Thin film analysis by X-ray scattering*. (Wiley-VCH Verlag GmbH Co., 2005).
 120. Ando, Y., Patel, J. R. & Kato, N. X-ray diffraction topographs of silicon crystals with superposed oxide film. III. Intensity distribution. *J. Appl. Phys.* **44**, 4405–4412 (1973).
 121. Hirano, K. *et al.* Formation of interference fringes in the Bragg-(Bragg)m-Laue mode. *Acta Crystallogr. Sect. A Found. Crystallogr.* **65**, 253–258 (2009).
 122. Authier, A., Lagomarsino, S. & Tanner, B. K. *X-Ray and Neutron Dynamical Diffraction: Theory and Applications*. (Springer Science, 1996).
 123. Bertotti, G. Generalized Preisach model for the description of hysteresis and eddy current effects in metallic ferromagnetic materials. *J. Appl. Phys.* **69**, 4608–4610 (1991).
 124. Bartic, A. T., Wouters, D. J., Maes, H. E., Rickes, J. T. & Waser, R. M. Preisach model for the simulation of ferroelectric capacitors. *J. Appl. Phys.* **89**, 3420–3425 (2001).
 125. Stancu, A., Ricinschi, D., Mitoseriu, L., Postolache, P. & Okuyama, M. First-order reversal curves diagrams for the characterization of ferroelectric switching. *Appl. Phys. Lett.* **83**, 3767–3769 (2003).
 126. Preisach, F. About the magnetic aftermath. *Zeitschrift für Phys.* **94**, 277 (1935).
 127. Hall, D. A. & Stevenson, P. J. High field dielectric behaviour of ferroelectric ceramics. *Ferroelectrics* **228**, 139–158 (1999).

128. Damjanovic, D. & Demartin, M. The Rayleigh law in piezoelectric ceramics. *J. Phys. D. Appl. Phys.* **29**, 2057–2060 (1996).
129. Rayleigh, Lord. XXV. Notes on electricity and magnetism.—III. On the behaviour of iron and steel under the operation of feeble magnetic forces. *London, Edinburgh, Dublin Philos. Mag. J. Sci.* **23**, 225–245 (1887).
130. Viehland, D., Jang, S. J., Cross, L. E. & Wuttig, M. Deviation from Curie-Weiss behavior in relaxor ferroelectrics. *Phys. Rev. B* **46**, 8003–8006 (1992).
131. Saremi, S., Kim, J., Ghosh, A., Meyers, D. & Martin, L. W. Defect-Induced (Dis)Order in Relaxor Ferroelectric Thin Films. *Phys. Rev. Lett.* **123**, 207602 (2019).
132. Erbil, A., Kim, Y. & Gerhardt, R. A. Giant Permittivity in Epitaxial Ferroelectric Heterostructures. *Phys. Rev. Lett.* **77**, 1628 (1996).
133. Zubko, P., Gariglio, S., Gabay, M., Ghosez, P. & Triscone, J.-M. Interface Physics in Complex Oxide Heterostructures. *Annu. Rev. Condens. Matter Phys.* **2**, 141–165 (2011).
134. Lee, H. N., Christen, H. M., Chisholm, M. F., Rouleau, C. M. & Lowndes, D. H. Strong polarization enhancement in asymmetric three-component ferroelectric superlattices. *Nature* **433**, 395–399 (2005).
135. Nakagawara, O. *et al.* Epitaxial growth and dielectric properties of superlattices by pulsed-laser deposition. *Appl. Phys. Lett.* **77**, 3257 (2000).
136. Tabata, H., Tanaka, H. & Kawai, T. Formation of artificial BaTiO₃/SrTiO₃ superlattices using pulsed laser deposition and their dielectric properties. *Appl. Phys. Lett.* **65**, 1970 (1994).
137. Johnston, K., Huang, X., Neaton, J. B. & Rabe, K. M. First-principles study of symmetry lowering and polarization in BaTiO₃/SrTiO₃ superlattices with in-plane expansion. *Phys. Rev. B* **71**, 100103 (2005).
138. Kendra Kathan-Galipeau *et al.* Quantification of internal electric fields and local polarization in ferroelectric superlattices. *ACS Nano* **5**, 640–646 (2010).
139. Ortega, N. *et al.* Effect of periodicity and composition in artificial BaTiO₃/(Ba,Sr)TiO₃ superlattices. *Phys. Rev. B* **83**, 144108 (2011).
140. Ortega, N. *et al.* Compositional engineering of BaTiO₃/(Ba,Sr)TiO₃ ferroelectric superlattices. *J. Appl. Phys.* **114**, 104102 (2013).
141. Wu, P. *et al.* Influence of interfacial coherency on ferroelectric switching of superlattice BaTiO₃/SrTiO₃. *Appl. Phys. Lett.* **107**, 122906 (2015).
142. Jo, J. Y. *et al.* Nanosecond dynamics of ferroelectric/dielectric superlattices. *Phys. Rev. Lett.* **107**, 055501 (2011).
143. Liu, G. *et al.* Reversible Polarization Rotation in Epitaxial Ferroelectric Bilayers. *Adv. Mater. Interfaces* **3**, 1600444 (2016).
144. Xue, F. *et al.* Phase field simulations of ferroelectrics domain structures in PbZr_xTi_{1-x}O₃ bilayers. *Acta Mater.* **61**, 2909–2918 (2013).
145. Sai, N., Meyer, B. & Vanderbilt, D. Compositional inversion symmetry breaking in ferroelectric perovskites. *Phys. Rev. Lett.* **84**, 5636–5639 (2000).
146. Specht, E. D., Christen, H., Norton, D. P. & Boatner, L. A. X-Ray Diffraction Measurement of the Effect of Layer Thickness on the Ferroelectric Transition in Epitaxial KTaO₃/KNbO₃ Multilayers. *Phys. Rev. Lett.* **80**, 4317 (1998).
147. Jaffe, B., Roth, R. S. & Marzullo, S. Piezoelectric Properties of Lead Zirconate-Lead Titanate Solid-Solution Ceramics. *J. Appl. Phys.* **25**, 809 (1954).
148. Noheda, B. *et al.* A monoclinic ferroelectric phase in the solid solution A monoclinic

- ferroelectric phase in the $\text{Pb}_{1-x}\text{Zr}_x\text{Ti}_x\text{O}_3$ solid solution. *Appl. Phys. Lett.* **74**, 2059 (1999).
149. Pandya, S. *et al.* Understanding the Role of Ferroelastic Domains on the Pyroelectric and Electrocaloric Effects in Ferroelectric Thin Films. *Adv. Mater.* **31**, 1–9 (2019).
 150. Noheda, B. *et al.* Stability of the monoclinic phase in the ferroelectric perovskite $\text{PbZr}_{1-x}\text{Ti}_x\text{O}_3$. *Phys. Rev. B* **63**, 014103 (2000).
 151. Cross, E. Lead-free at last. *Nature* **432**, 24–25 (2004).
 152. Mangalam, R. V. K., Karthik, J., Damodaran, A. R., Agar, J. C. & Martin, L. W. Unexpected crystal and domain structures and properties in compositionally graded $\text{PbZr}_{1-x}\text{Ti}_x\text{O}_3$ thin films. *Adv. Mater.* **25**, 1761–1767 (2013).
 153. Agar, J. C. *et al.* Highly mobile ferroelastic domain walls in compositionally graded ferroelectric thin films. *Nat. Mater.* **15**, 549–556 (2016).
 154. Agar, J. C. *et al.* Complex Evolution of Built-in Potential in Compositionally-Graded $\text{PbZr}_{1-x}\text{Ti}_x\text{O}_3$ Thin Films. *ACS Nano* **9**, 7332 (2015).
 155. Huang, H. H. *et al.* Epitaxial $\text{PbZr}_x\text{Ti}_{1-x}\text{O}_3$ Ferroelectric Bilayers with Giant Electromechanical Properties. *Adv. Mater. Interfaces* **2**, 1500075 (2015).
 156. Bao, D., Scholz, R., Alexe, M. & Hesse, D. Growth, microstructure, and ferroelectric properties of $\text{Pb}(\text{Zr}_{0.4}\text{Ti}_{0.6})\text{O}_3/\text{PbZrO}_3$ superlattices prepared on SrTiO_3 (100) substrates by pulsed laser deposition. *J. Appl. Phys.* **101**, 054118 (2007).
 157. Kornev, I. A. & Bellaiche, L. Unusual Thermodynamic Properties and Nonergodicity in Ferroelectric Superlattices. *Phys. Rev. Lett.* **91**, 116103 (2003).
 158. Janolin, P.-E. Strain on ferroelectric thin films. *J. Mater. Sci.* **44**, 5025–5048 (2009).
 159. Hoon Oh, S. & Jang, H. W. Two-dimensional thermodynamic theory of epitaxial $\text{Pb}(\text{Zr},\text{Ti})\text{O}_3$ thin films. *Phys. Rev. B* **62**, 14757 (2000).
 160. Pertsev, N. A., Kukhar, V. G., Kohlstedt, H. & Waser, R. Phase diagrams and physical properties of single-domain epitaxial (formula presented) thin films. *Phys. Rev. B* **67**, 1–10 (2003).
 161. Xu, R., Karthik, J., Damodaran, A. R. & Martin, L. W. Stationary domain wall contribution to enhanced ferroelectric susceptibility. *Nat. Commun.* **5**, 3120 (2014).
 162. Pike, C. R., Roberts, A. P. & Verosub, K. L. Characterizing interactions in fine magnetic particle systems using first order reversal curves. *J. Appl. Phys.* **85**, 6660 (2013).
 163. Kim, Y. *et al.* First-order reversal curve probing of spatially resolved polarization switching dynamics in ferroelectric nanocapacitors. *ACS Nano* **6**, 491 (2012).
 164. Hong, Z. & Chen, L. Q. Blowing polar skyrmion bubbles in oxide superlattices. *Acta Mater.* **152**, 155–161 (2018).
 165. Lupi, E. *et al.* Large Polarization and Susceptibilities in Artificial Morphotropic Phase Boundary $\text{PbZr}_{1-x}\text{Ti}_x\text{O}_3$ Superlattices. *Adv. Electron. Mater.* **6**, 1–10 (2020).
 166. Hashemizadeh, S. & Damjanovic, D. Nonlinear dynamics of polar regions in paraelectric phase of $(\text{Ba}_{1-x}\text{Sr}_x)\text{TiO}_3$ ceramics. *Appl. Phys. Lett.* **110**, 192905 (2017).
 167. Ménoret, C. *et al.* Structural evolution and polar order in $\text{Sr}_{1-x}\text{Ba}_x\text{TiO}_3$. *Phys. Rev. B* **65**, 224104 (2002).
 168. Vendik, O. G. & Zubko, S. P. Ferroelectric phase transition and maximum dielectric permittivity of displacement type ferroelectrics ($\text{Ba}_x\text{Sr}_{1-x}\text{TiO}_3$). *J. Appl. Phys.* **88**, 5343–5350 (2000).
 169. Wang, S. Y. *et al.* Dielectric and ferroelectric properties of $\text{Ba}_{1-x}\text{Sr}_x\text{TiO}_3$ thin films prepared by pulsed laser deposition. *Key Eng. Mater.* **280–283**, 81–84 (2005).

170. Li, F. *et al.* Ultrahigh piezoelectricity in ferroelectric ceramics by design. *Nat. Mater.* **17**, 349 (2018).
171. Grinberg, I., Juhás, P., Davies, P. K. & Rappe, A. M. Relationship between local structure and relaxor behavior in perovskite oxides. *Phys. Rev. Lett.* **99**, 21–24 (2007).
172. Shetty, S. *et al.* Relaxor Behavior in Ordered Lead Magnesium Niobate (PbMg_{1/3}Nb_{2/3}O₃) Thin Films. *Adv. Funct. Mater.* **29**, 1–9 (2019).
173. Alexandru, H. V., Berbecaru, C., Ioachim, A., Nedelcu, L. & Dutu, A. BST solid solutions, temperature evolution of the ferroelectric transitions. *Appl. Surf. Sci.* **253**, 354 (2006).
174. Pullar, R. C. *et al.* Manufacture and measurement of combinatorial libraries of dielectric ceramics. Part II. Dielectric measurements of Ba_{1-x}Sr_xTiO₃ libraries. *J. Eur. Ceram. Soc.* **27**, 4437–4443 (2007).
175. Singh, S., Singh, S. P. & Pandey, D. A succession of relaxor ferroelectric transitions in Ba_{0.55}Sr_{0.45}TiO₃. *J. Appl. Phys.* **103**, 2006–2009 (2008).
176. Wexler, R. B., Qi, Y. & Rappe, A. M. Sr-induced dipole scatter in Ba_xSr_{1-x}TiO₃: Insights from a transferable-bond valence-based interatomic potential. *Phys. Rev. B* **100**, 1–9 (2019).
177. Donoho, D. L. & Johnstone, J. M. Ideal spatial adaptation by wavelet shrinkage. *Biometrika* **81**, 425–455 (1994).
178. Gim, Y. *et al.* Microstructure and dielectric properties of Ba_{1-x}Sr_xTiO₃ films grown on LaAlO₃ substrates. *Appl. Phys. Lett.* **77**, 1200–1202 (2000).
179. Lu, S. G. *et al.* High tunability in compositionally graded epitaxial barium strontium titanate thin films by pulsed-laser deposition. *Appl. Phys. Lett.* **82**, 2877–2879 (2003).
180. Pramanick, A. *et al.* Microdomain dynamics in single-crystal BaTiO₃ during paraelectric-ferroelectric phase transition measured with time-of-flight neutron scattering. *Phys. Rev. B* **92**, 1–10 (2015).
181. Ke, S., Huang, H. & Fan, H. Relaxor behavior in CaCu₃Ti₄O₁₂ ceramics. *Appl. Phys. Lett.* **89**, 87–90 (2006).
182. Plimpton, S. Fast Parallel Algorithms for Short-Range Molecular Dynamics. *J. Comput. Phys.* **117**, 1–19 (1995).
183. Schildkamp, W. & Fischer, K. Rhomboedrisches BaTiO₃: Strukturuntersuchung bei 132° K und 196° K. *Zeitschrift für Krist. - Cryst. Mater.* **155**, 217–226 (1981).
184. Qi, Y., Liu, S., Grinberg, I. & Rappe, A. M. Atomistic description for temperature-driven phase transitions in BaTiO₃. *Phys. Rev. B* **94**, 1–8 (2016).
185. Balachandran, P. V., Xue, D. & Lookman, T. Structure-Curie temperature relationships in BaTiO₃-based ferroelectric perovskites: Anomalous behavior of (Ba,Cd)TiO₃ from DFT, statistical inference, and experiments. *Phys. Rev. B* **93**, 1–12 (2016).
186. Kittel, C. Theory of the structure of ferromagnetic domains in films and small particles. *Phys. Rev.* **70**, 965–971 (1946).
187. Kittel, C. Physical theory of ferromagnetic domains. *Rev. Mod. Phys.* **21**, 541 (1949).
188. Bennett, D., Muñoz Basagoiti, M. & Artacho, E. Electrostatics and domains in ferroelectric superlattices: Domains in ferroelectric superlattices. *R. Soc. Open Sci.* **7**, (2020).
189. Pragada, S. & Sivaswamy, J. Image denoising using matched biorthogonal wavelets. *Proc. - 6th Indian Conf. Comput. Vision, Graph. Image Process. ICVGIP 2008* 25–32 (2008). doi:10.1109/ICVGIP.2008.95
190. Nogués, J. & Schuller, I. K. Exchange bias. *J. Magn. Magn. Mater.* **192**, 203–232 (1999).
191. Ohtomo, A. & Hwang, H. Y. A high-mobility electron gas at the LAO/STO heterointerface. *Nature* **427**, 423–426 (2004).

192. Warusawithana, M. P. *et al.* LaAlO₃ stoichiometry is key to electron liquid formation at LaAlO₃/SrTiO₃ interfaces. *Nat. Commun.* **4**, 1–9 (2013).
193. Nakagawa, N., Hwang, H. Y. & Muller, D. A. Why some interfaces cannot be sharp. *Nat. Mater.* **5**, 204–209 (2006).
194. Schoofs, F., Egilmez, M., Fix, T., MacManus-Driscoll, J. L. & Blamire, M. G. Impact of structural transitions on electron transport at LaAlO₃/SrTiO₃ heterointerfaces. *Appl. Phys. Lett.* **100**, 081601 (2012).
195. Xie, Y., Hikita, Y., Bell, C. & Hwang, H. Y. Control of electronic conduction at an oxide heterointerface using surface polar adsorbates. *Nat. Commun.* **2**, 494–495 (2011).
196. Kim, S. K. *et al.* Electric-field-induced Shift in the Threshold Voltage in LaAlO₃/SrTiO₃ Heterostructures. *Sci. Rep.* **5**, 8023 (2015).
197. Breckenfeld, E., Bronn, N., Mason, N. & Martin, L. W. Tunability of conduction at the LaAlO₃/SrTiO₃ heterointerface: Thickness and compositional studies. *Appl. Phys. Lett.* **105**, 0–5 (2014).
198. Grutter, A. J. *et al.* Interfacial ferromagnetism in LaNiO₃/CaMnO₃ superlattices. *Phys. Rev. Lett.* **111**, 087202 (2013).
199. Hoffman, J. *et al.* Charge transfer and interfacial magnetism in (LaNiO₃)_n/(LaMnO₃)₂ superlattices. *Phys. Rev. B* **88**, 144411 (2013).
200. Chen, Z. *et al.* Electron Accumulation and Emergent Magnetism in LaMnO₃ = SrTiO₃ Heterostructures. *Phys. Rev. Lett.* **119**, 156801 (2017).
201. Chambers, S. A. *et al.* Band alignment, built-in potential, and the absence of conductivity at the LaCrO₃/SrTiO₃(001) heterojunction. *Phys. Rev. Lett.* **107**, 4–7 (2011).
202. Qiao, L., Droubay, T. C., Bowden, M. E., Shutthanandan, V. & Kaspar, T. C. LaCrO₃ heteroepitaxy on SrTiO₃(001) by molecular beam epitaxy. *Appl. Phys. Lett.* **99**, 061904 (2011).
203. Takizawa, M., Tsuda, S., Susaki, T., Hwang, H. Y. & Fujimori, A. Electronic charges and electric potential at LaAlO₃/SrTiO₃ interfaces studied by core-level photoemission spectroscopy. *Phys. Rev. B* **84**, 3–7 (2011).
204. Hong, W. T. *et al.* Probing LaMO₃ Metal and Oxygen Partial Density of States Using X-ray Emission, Absorption, and Photoelectron Spectroscopy. *J. Phys. Chem. C* **119**, 2063–2072 (2015).
205. Zhang, J. *et al.* Cooperative photoinduced metastable phase control in strained manganite films. *Nat. Mater.* **15**, 956–960 (2016).
206. Huang, Z. *et al.* Tuning the ground state of La_{0.67}Ca_{0.33}MnO₃ films via coherent growth on orthorhombic NdGaO₃ substrates with different orientations. *Phys. Rev. B* **86**, 1–8 (2012).
207. Wang, L. F. *et al.* Annealing assisted substrate coherency and high-temperature antiferromagnetic insulating transition in epitaxial La_{0.67}Ca_{0.33}MnO₃/NdGaO₃(001) films. *AIP Adv.* **3**, 0–14 (2013).
208. Basov, D. N., Averitt, R. D., Van Der Marel, D., Dressel, M. & Haule, K. Electrodynamics of correlated electron materials. *Rev. Mod. Phys.* **83**, 471–541 (2011).
209. Kovaleva, N. N. *et al.* Spin-controlled mott-hubbard bands in LaMnO₃ probed by optical ellipsometry. *Phys. Rev. Lett.* **93**, 1–4 (2004).
210. Quijada, M., Černe, J., Simpson, J. & Drew, H. Optical conductivity of manganites: Crossover from Jahn-Teller small polaron to coherent transport in the ferromagnetic state. *Phys. Rev. B* **58**, 16093–16102 (1998).

211. Kim, K. H., Lee, S., Noh, T. W. & Cheong, S. W. Charge Ordering Fluctuation and Optical Pseudogap in [Formula presented]. *Phys. Rev. Lett.* **88**, 4 (2002).
212. Lesne, E. *et al.* Suppression of the critical thickness threshold for conductivity at the LaAlO₃/SrTiO₃ interface. *Nat. Commun.* **5**, 4291 (2014).
213. Moetakef, P. *et al.* Electrostatic carrier doping of GdTiO₃/SrTiO₃ interfaces. *Appl. Phys. Lett.* **99**, (2011).
214. Sagdeo, P. R., Anwar, S. & Lalla, N. P. Powder X-ray diffraction and Rietveld analysis of La_{1-x}CaxMnO₃ (0 < X < 1). *Powder Diffr.* **21**, 40–44 (2006).
215. Rogdakis, K. *et al.* Tunable ferroelectricity in artificial tri-layer superlattices comprised of non-ferroic components. *Nat. Commun.* **3**, (2012).
216. Tokura, Y. Multiferroics-toward strong coupling between magnetization and polarization in a solid. *J. Magn. Magn. Mater.* **310**, 1145–1150 (2007).
217. Warusawithana, M. P., Colla, E. V., Eckstein, J. N. & Weissman, M. B. Artificial Dielectric Superlattices with Broken Inversion Symmetry. *Phys. Rev. Lett.* **90**, 4 (2003).
218. Lee, H. N., Christen, H. M., Chisholm, M. F., Rouleau, C. M. & Lowndes, D. H. Strong polarization enhancement in asymmetric three-component ferroelectric superlattices. *Nature* **433**, 395–399 (2005).
219. Kida, N. *et al.* Optical magnetoelectric effect of patterned oxide superlattices with ferromagnetic interfaces. *Phys. Rev. Lett.* **99**, 1–4 (2007).
220. Virshup, G. F., Klausmeier-Brown, M. E., Bozovic, I. & Eckstein, J. N. Hysteretic, high Tc Josephson junctions using heterostructure trilayer films grown by molecular beam epitaxy. *Appl. Phys. Lett.* **60**, 2288–2290 (1992).
221. Cao, Y. *et al.* Artificial two-dimensional polar metal at room temperature. *Nat. Commun.* **9**, (2018).
222. Xu, R. *et al.* Ferroelectric polarization reversal via successive ferroelastic transitions. *Nat. Mater.* **14**, 79–86 (2015).
223. Liang, Y. C., Wu, T. B., Lee, H. Y. & Hsieh, Y. W. Structural characteristics of epitaxial BaTiO₃/LaNiO₃ superlattice. *J. Appl. Phys.* **96**, 584–589 (2004).
224. Qiao, L. & Bi, X. Dielectric phase transition and relaxor behavior in BaTiO₃/LaNiO₃ superlattice. *CrystEngComm* **13**, 1693–1696 (2011).
225. De Luca, G. *et al.* Nanoscale design of polarization in ultrathin ferroelectric heterostructures. *Nat. Commun.* **8**, 1–7 (2017).
226. Guo, E. J. *et al.* Influence of chemical composition and crystallographic orientation on the interfacial magnetism in BiFeO₃ / La_{1-x}Sr_xMnO₃ superlattices. *Phys. Rev. Mater.* **2**, 1–8 (2018).
227. Liu, Y. T., Chiu, S. J., Lee, H. Y. & Chen, S. Y. Fabrication and ferroelectric properties of BiFeO₃/LaNiO₃ artificial superlattice structures grown by radio-frequency magnetron-sputtering. *Thin Solid Films* **529**, 66–70 (2013).
228. Haun, M. J., Furman, E., Jang, S. J. & Cross, L. E. Thermodynamic theory of the lead zirconate-titanate solid solution system, part v: Theoretical calculations. *Ferroelectrics* **99**, 63–86 (1989).
229. Chen, L. Q. Phase-field method of phase transitions/domain structures in ferroelectric thin films: A review. *J. Am. Ceram. Soc.* **91**, 1835–1844 (2008).

Appendix A: RHEED-assisted PLD conditions

Pulsed-laser deposition parameters for every system used in this work were optimized for growth mode, composition, topography, and desired properties. The optimized parameters for each materials system are provided. Most films were grown on a Twente Solid State Technologies (TSST) deposition chamber, equipped with a RHEED gun and detector.

Film	Substrate(s)	Fluence (J cm ⁻²)	Spot size (cm ²)	Laser Frequ- ency (Hz)	Growth Pressure (mTorr)	Cooldown Pressure mTorr or <i>atmospheric</i>	Temp- erature (°C)	Thickness nm or (<i>u.c.</i>)	Growth rate (pulses / unit cell)
SrRuO₃	GdScO3 (110)	1.15	0.0394	10	100	flexible	700	20	68
Ba_{0.5}Sr_{0.5}RuO₃	SmScO3 (110), NdScO3 (110)	1.15	0.0394	10	100	flexible	700	20	68
SrTiO₃	GdScO3 (110), SmScO3 (110), NdScO3 (110)	2.05	0.0109	5	20	<i>atm</i>	700	(2-20)	50
BaTiO₃	GdScO3 (110), SmScO3 (110), NdScO3 (110)	2.05	0.0109	5	20	<i>atm</i>	700	(4-20)	47
Ba_{0.6}Sr_{0.4}TiO₃	GdScO3 (110)	1.52	0.086	2	40	<i>atm</i>	600	150	-
PbZr_{0.4}Ti_{0.6}O₃	PrScO3 (110)	1.41	0.03	10	100	<i>atm</i>	610	(4-16)	23
PbZr_{0.52}Ti_{0.48}O₃	PrScO3 (110)	1.41	0.03	10	100	<i>atm</i>	610	80 nm	25
PbZr_{0.8}Ti_{0.2}O₃	PrScO3 (110)	1.41	0.03	10	100	<i>atm</i>	610	(4-32)	25
La_{0.67}Ca_{0.33}MnO₃	SrTiO3 (001)	1.27	0.0394	2	200	<i>atm</i>	750	20	38
LaCrO₃	SrTiO3 (001)	1.42	0.03	2	2	2	700	20	165